

Molecular mechanisms of proton-coupled electron transfer and water oxidation in photosystem II

(光化学系 II におけるプロトン共役電子移動および
水分解反応の分子機構)

Shin Nakamura

中村 伸

Table of contents

Abbreviations.....	3
Chapter 1: General introduction	4
1.1. Photosystem II	4
1.2. Fourier transform infrared spectroscopy (FTIR).....	7
1.3. Quantum chemical calculation.....	9
1.4. Purpose of this study	10
References	11
Chapter 2: Hydrogen bond structure of redox active tyrosines in photosystem II	16
2.1. Introduction	16
2.2. Materials and Methods	18
2.3. Results	21
2.4. Discussion	31
References	36
Chapter 3: Proton release reaction of tyrosine D in photosystem II....	43
3.1. Introduction	43
3.2. Materials and Methods	44
3.3. Results	46
3.4. Discussion	50
References	54
Chapter 4: Vibrational analysis of water network around the Mn cluster	59
4.1. Introduction	59
4.2. Materials and Methods	60
4.3. Results	60
4.4. Discussion	65
References	68
Chapter 5: Vibrational analysis of carboxylate ligands in the water oxidizing center.....	59
5.1. Introduction	74
5.2. Materials and Methods	76
5.3. Results	77
5.4. Discussion	82

References	85
Chapter 6: Protonation structure of a key histidine in the water oxidizing center.....	91
6.1. Introduction	91
6.2. Materials and Methods	93
6.3. Results	96
6.4. Discussion	107
References	111
Chapter 7: general conclusion.....	118
Acknowledgments.....	120

Abbreviations

PSII: photosystem II

P680: the special pair chlorophyll of photosystem II

FTIR: Fourier transform infrared

DFT: density functional theory

QM/MM: quantum mechanics/molecular mechanics

ONIOM: our own *n*-layered integrated molecular orbital and molecular mechanics

PDB: Protein Data Bank

WOC: water-oxidizing center

XFEL: X-ray free electron laser

Y_D: redox-active tyrosine on the D2 protein

Y_Z: redox-active tyrosine on the D1 protein

Q_A: primary quinone electron acceptor

Q_B: secondary quinone electron acceptor

DM: *n*-dodecyl-β-D-maltoside

Mes: 2-(*N*-morpholino)ethanesulfonic acid

Hepes: 4-(2-hydroxyethyl)-1-piperazineethanesulfonic acid

MeIm: methylimidazole

General introduction

1.1. Photosystem II

In plants and cyanobacteria, photosystem II (PSII) has a function of photosynthetic water oxidation.¹⁻⁷ PSII is a multisubunit protein complex embedded in thylakoid membranes (Figure 1.1). Water oxidation splits water into molecular oxygen and protons. Virtually all of atmospheric oxygen, which is essential for the sustenance of life on Earth, is produced by this reaction. Released protons generate a proton gradient across the membranes, which is utilized to produce ATP, a form of chemical energy, at ATPase. Electrons obtained by water oxidation are utilized for reducing carbon dioxide to synthesize sugars together with ATP.

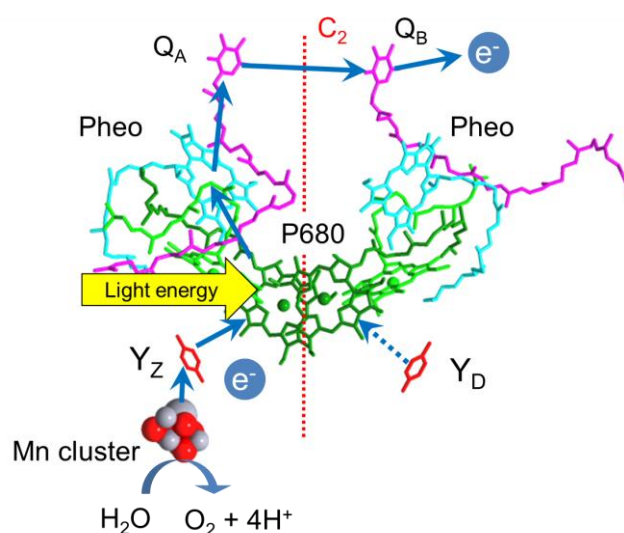


Figure 1.1 Redox cofactors and electron transfer chain of PSII

Electron transfer and water oxidation reactions in PSII starts with light-induced charge separation at the excited state of reaction center chlorophylls (a coupled excited state of special pair chlorophyll, P680, and monomer chlorophyll, Chl_{D1}). An electron is ejected to a pheophytin electron acceptor (Pheo) and then transferred to plastoquinone electron acceptors (Q_A and Q_B).⁸ On the electron-donor side, the generated P680⁺ cation abstracts an electron from the water-oxidizing center (WOC) via a redox-active tyrosine Y_Z (D1-Y161).

There is also another redox-active tyrosine, Y_D (D2-Y160), in PSII (Figure 1.1). These two redox-active tyrosines, Y_Z and Y_D, are symmetrically located in PSII.^{9, 10} It is known that these tyrosines take place proton-coupled electron transfer reactions (Figure 1.2):¹¹⁻²⁵ Namely,

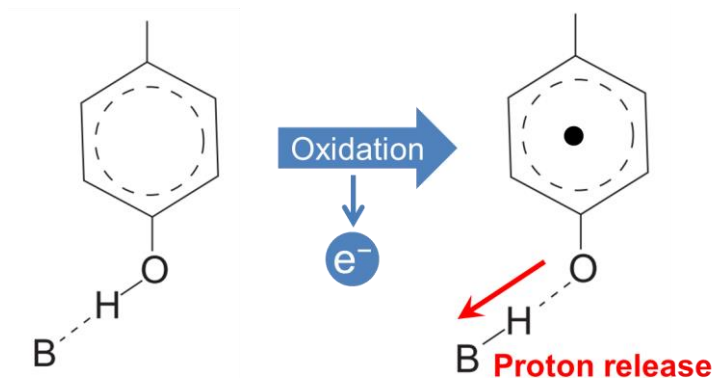


Figure 1.2 Proton-coupled electron transfer of a tyrosine side chain

when a tyrosine side chain is oxidized, its phenolic proton is released to form a neutral radical (Y_Z^{\bullet} or Y_D^{\bullet}) due to a low pK_a value ($pK_a = -2.0$) in the oxidized state.^{23, 26, 27} However, the roles of these tyrosines are significantly different. Y_D functions as a secondary electron donor to $P680^+$, whereas Y_Z functions as a major electron donor to $P680^+$ and then accepts an electron from the WOC. This asymmetry of electron transfer is crucial for the high quantum efficiency of water oxidation in PSII. However, the origin of this asymmetry has not been clarified.

Recent X-ray crystallographic analysis has revealed the detailed structure of the WOC and the surrounding protein environment (Figure 1.3A).^{9, 10, 28-30} The catalytic core is the Mn cluster, which is a cubane-like cluster formed with three Mn atoms (Mn1-Mn3), one Ca atom, and four oxygen atoms (O1-O3, and O5), combined with a dangling Mn atom (Mn4) connected by two oxygen atoms (O4 and O5). The Mn cluster is surrounded by amino acid ligands of six carboxylate groups [D1-D170, D1-E189, D1-E333, D1-D342, D1-A344 (C-terminus), and CP43-

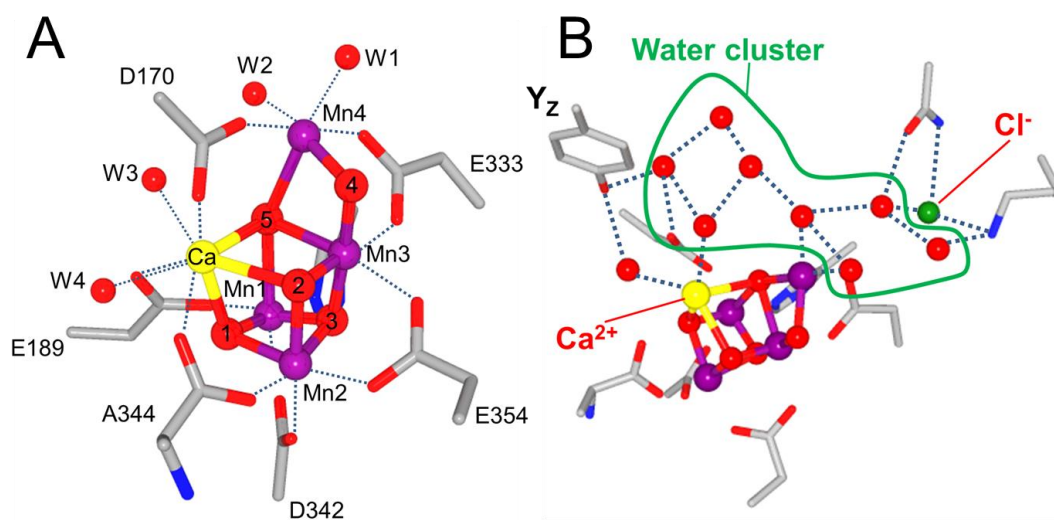


Figure 1.3 (A) Structure of the Mn cluster and the surrounding amino acids and (B) the water cluster

E354] and an imidazole group (D1-H332). In addition, four water ligands on Mn4 (W1 and W2) and Ca (W3 and W4) have been identified. A guanidine group (CP43-R357), an imidazole group (D1-H337), and water molecules are hydrogen-bonded with the Mn cluster. Moreover, several water molecules form a water cluster near the Mn cluster (Figure 1.3B). However, the roles of these amino acid residues and water molecules for water oxidation have not been clarified yet.

The water oxidation reaction proceeds through a cycle of five intermediates called the S_i state ($i = 0-4$) (Figure 1.4).^{31, 32} The S_1 state is the most stable in the dark, while the other S_i states ($i = 0-3$) advance to the S_{i+1} state upon oxidation by Y_Z^{\cdot} . The S_4 state is the highest oxidation state and immediately relaxes to the S_0 state releasing an oxygen molecule. In the S-state cycle, four protons are produced from two water molecules and released into the lumen. Proton release occurs in the $S_0 \rightarrow S_1$, $S_1 \rightarrow S_2$, $S_2 \rightarrow S_3$, and $S_3 \rightarrow S_0$ transitions with a stoichiometry of 1 : 0 : 1 : 2.³³⁻³⁵ This means that an excess positive charge is accumulated on the Mn cluster in the S_2 and S_3 states.

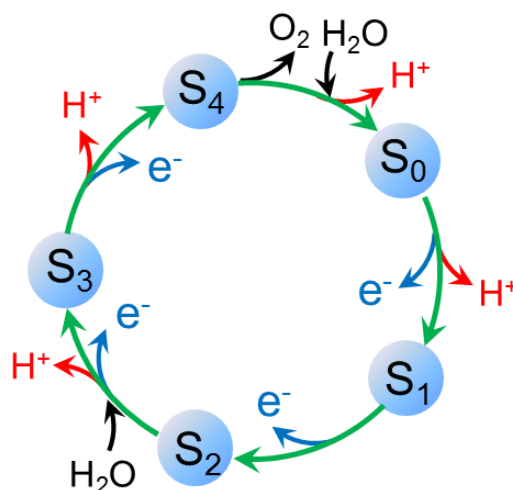


Figure 1.4 S-state cycle of WOC

In water oxidation, proton transfer is a crucial process. The recent high-resolution X-ray structure^{9, 10, 29} suggested several candidates of proton transfer pathways from the WOC to the lumen. However, it has not been clarified yet which pathways are suitable for proton release. One candidate is the hydrogen bond network from the Mn cluster to the lumen via Y_Z (Figure 1.5).⁹ Thus, it is possible that Y_Z plays a key role in not only electron transfer but also proton transfer in the water oxidation mechanism.

In spite that the high-resolution X-ray crystallographic structure of the WOC has been revealed, the molecular mechanism of photosynthetic water oxidation is still largely unresolved. One of the main reasons for this is that the X-ray structures reported so far have not resolved hydrogen atoms.^{9, 10, 28-30} The information of the structures and reactions of protons is crucial to

reveal the process of water oxidation. Thus, it is necessary to investigate the protonation and

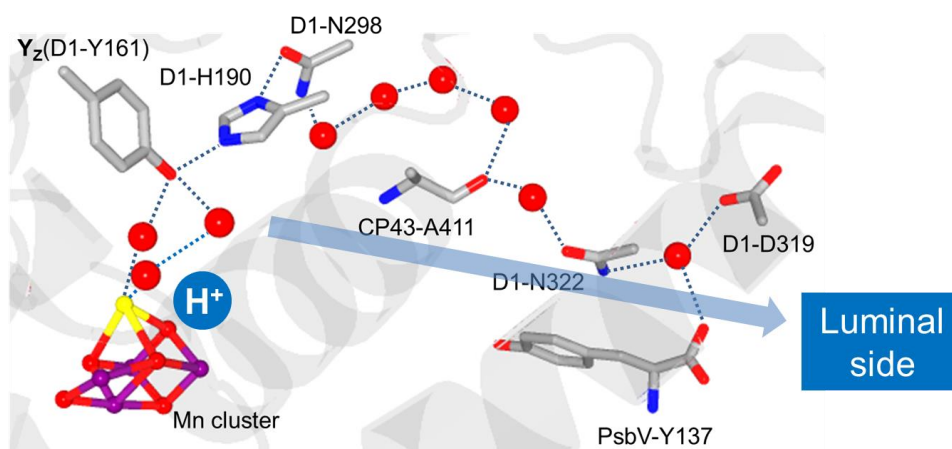


Figure 1.5 Hydrogen bond network from the Mn cluster to the lumen via Y_z hydrogen-bonded structures of water molecules and proteins in the WOC for full understanding of the water oxidation mechanism.

1.2. Fourier transform infrared spectroscopy (FTIR)

Infrared spectroscopy is widely used to investigate the structural information of molecules. The energy of infrared light corresponds to the excitation of molecular vibrations, which reflect the structures and interactions of molecules. Infrared absorption occurs when the dipole moments of the vibrations are changed upon excitation. The coordinates of normal modes, their vibrational frequencies, and the intensities of infrared absorption are very sensitive to subtle structural changes of the molecules. Thus, infrared spectroscopy is a powerful method to detect the changes in chemical bonds in reactions, in particular, changes in protonation structures and hydrogen-bond interactions. For instance, in an OH stretching vibration, a hydrogen-bond interaction induces a downshift of the vibrational frequency by weakening the strength of the O-H bond.

Infrared spectroscopy has been extensively used to obtain the structural information of proteins, because all of amino acids forming polypeptide chains and water molecules are infrared active. However, infrared absorption spectra of proteins mainly provide the bands of amide groups of polypeptide main chains. In addition, bands of all of amino-acid side chains and water molecules overlap to form relatively broad spectral features. Hence, specific information of the active site of a protein, which is necessary for detailed analysis of enzymatic reactions, cannot be obtained only from its original infrared spectrum. To extract signals specific to the active site of a protein, the reaction-induced Fourier transform infrared (FTIR) difference technique has been

developed.³⁶ In this method, by taking a difference between spectra measured before and after the reaction, a large absorption that is not involved in the reaction is canceled and only the infrared bands of the active site affected by the reaction are obtained (Figure 1.6). With this method, the change of even a single chemical bond in a very large protein (e.g., > 500 kDa) can be detected. In such a measurement, a very small absorption change ($\Delta A < 10^{-4}$) must be detected and hence this technique requires an extremely high accuracy.

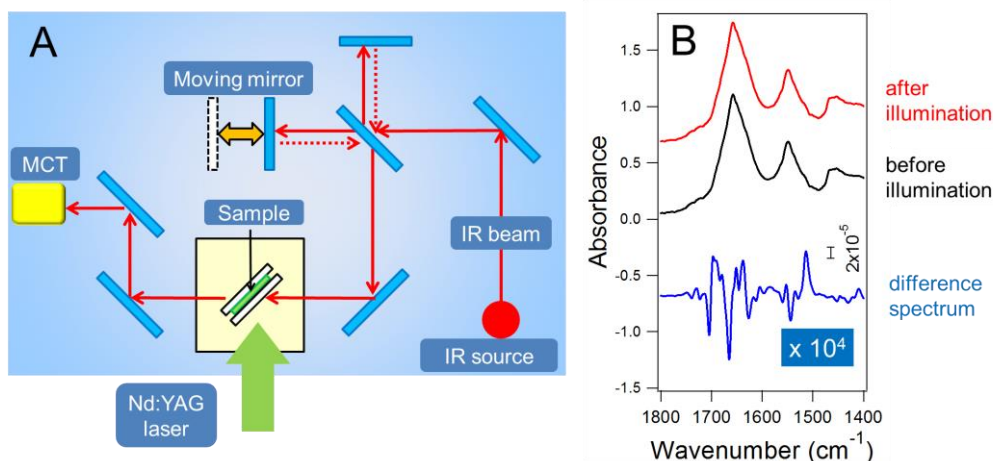


Figure 1.6 (A) The diagram of light-induced FTIR difference measurements and (B) an example of the different spectrum (blue line) between spectra before (red line) and after (black line) illumination

FTIR spectroscopy realizes such a high accuracy in the wavenumber axis by using a Michelson interferometer. Infrared light from an IR source, which passes through a Michelson interferometer and a sample, is monitored at a mercury cadmium telluride (MCT) detector as a function of the position of a moving mirror (Figure 1.6). Because this position of the moving mirror is monitored using a He-Ne laser, which has a wavenumber accuracy of more than 7 digits, the obtained spectra also have a high wavenumber accuracy. Thus, FTIR spectroscopy is suitable method for detecting a very small spectral change in a large protein.

The attenuated total reflectance (ATR) technique is also useful in the measurement of reaction-induced FTIR difference spectra (Figure 1.7).^{37, 38} In contrast to a conventional

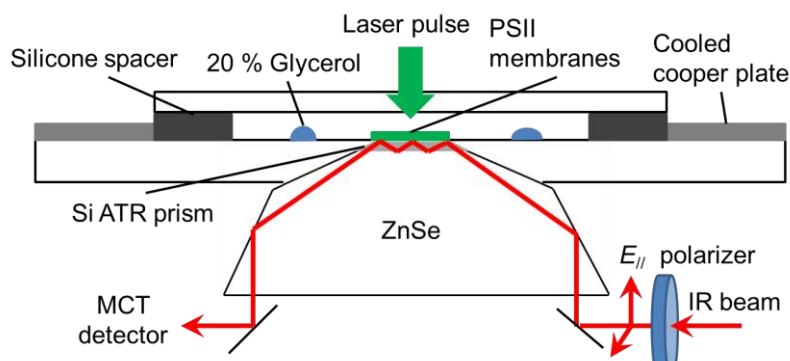


Figure 1.7 Diagram of polarized ATR-FTIR measurement

transmission method, it detects infrared absorption utilizing the penetration of the evanescent wave of infrared light into the sample on the surface of the internal reflection element (IRE).³⁹ Using the ATR method, the condition of the sample can be changed by exchanging buffers on the sample adsorbed on the IRE surface.⁴⁰ Furthermore, polarized FTIR measurement is readily applied to an oriented sample on the IRE surface, to estimate the directions of the dipole moments of molecular vibrations.⁴¹

The reaction-induced FTIR difference spectroscopy has been applied to various biological systems. As a trigger to initiate reactions in proteins, light illumination is the most convenient. This method, light-induced FTIR difference spectroscopy, has been used to investigate the reaction mechanism of many photo-sensitive proteins, such as photosynthetic proteins and bacteriorhodopsin.⁴²⁻⁴⁴ In particular, the mechanism of water oxidation in PSII has been investigated using this technique, and the information of the structural and interaction changes in amino acid side chains, polypeptide main chains, and water molecules, and that of the proton releases and transition efficiencies during the S-state cycle have been obtained.⁴⁵⁻⁴⁷

1.3. Quantum chemical calculation

Quantum chemical calculations theoretically predict the most stable structures and the vibrational frequencies of chemical compounds.⁴⁸ In particular, density functional theory (DFT) is a highly versatile method for the analysis of various types of compounds from a small molecule to a biopolymer.⁴⁹ Quantum chemical calculations make it possible to simulate the protonation structure and the conformational changes during the reaction in a protein, which are difficult to obtain by X-ray crystallography. Thus, with the aid of vibrational analysis using quantum chemical calculations, detailed structural information can be obtained from experimental infrared

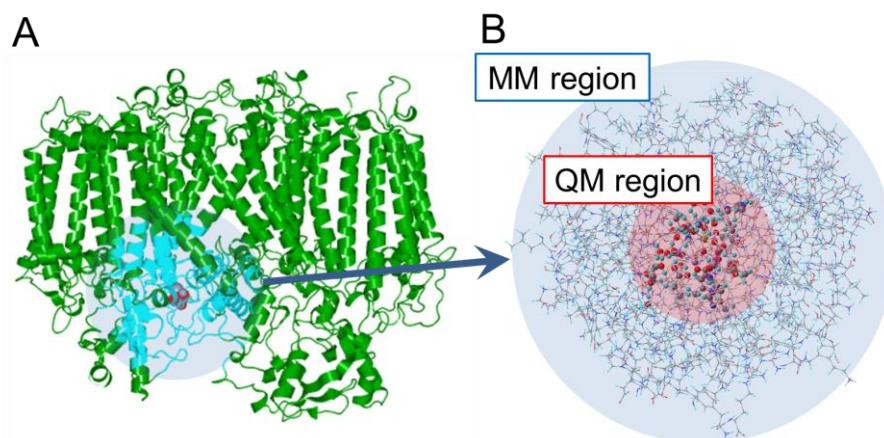


Figure 1.8 (A) Example of the region of the QM/MM system in PSII and (B) the MM and QM regions in QM/MM calculation

spectra.⁵⁰⁻⁵²

The QM/MM method is widely applied to the simulations of large systems. The calculation system is separated into two regions, MM and QM regions (Figure 1.8).⁵³⁻⁵⁵ QM calculations provide highly accurate simulation, although calculation costs are very high. In contrast, the cost of MM calculations is low in spite of lower accuracy than the QM calculations. The QM/MM calculations combine these merits of the two calculations. Thus, QM/MM method is suitable for the simulation of an active-site structure in a large system such as WOC in a PSII protein complex.

1.4. Purpose of this study

Unanswered essential questions regarding the electron transfer and water oxidation mechanisms of PSII mentioned above are summarized as follows. (1) What is the reason for the asymmetry in electron transfer of Y_Z and Y_D in spite of their symmetric locations? The electron transfer rate of Y_Z is much faster than that of Y_D, causing a high quantum efficiency of water oxidation. (2) What is the role of a hydrogen-bond network formed by water molecules around the Mn cluster in proton transfer? Which pathway is used for proton exit during water oxidation? (3) What are the roles of amino acid residues near the Mn cluster in the water oxidation mechanism?

To answer these questions, we used a combinatorial approach of experimental and computational methods, i.e., light-induced FTIR difference spectroscopy and QM/MM calculations. As for the question (1), proton-coupled electron transfer of a tyrosine side chain should be a key process to solve the problem, and hence the hydrogen-bonded structures of Y_Z and Y_D were investigated and compared (Chapter 2). To further examine the difference in proton transfer reactions, the quantities of protons released from Y_Z and Y_D upon their oxidation were estimated by monitoring protonation signals of buffer molecules using the isotope-edited FTIR method (Chapter 3). From these studies, it was found that Y_Z and Y_D indeed have significantly different hydrogen-bonded structures and proton release reactions, which explains the significant difference in the electron transfer rate. The question (2) was investigated using QM/MM calculations (Chapter 4). The OH stretching bands of water molecules in the FTIR difference spectrum of WOC were analyzed and the experimental spectrum was reproduced. We suggested that a delocalized water vibration plays an important role in rapid proton transfer by the Grotthuss mechanism. For the question (3), the role of carboxylate ligands to the Mn cluster was studied by normal-mode analysis using QM/MM calculations (Chapter 5). It was shown that the vibration of a key carboxylate ligand bridging the Mn and Ca ions regulates the reactivity of water ligands. Furthermore, polarized ATR-FTIR spectroscopy combined with the QM/MM analysis was used

to investigate the role of a His side chain hydrogen-bonded with the Mn cluster (Chapter 6). It was proved that this His residue has a protonated cation form during the S-state cycle of water oxidation, playing an important role in keeping the redox potential of the Mn cluster high enough to oxidize water. In the last chapter (Chapter 7), the conclusion of this work is summarized.

References

- [1] Debus, R. J. (1992) The manganese and calcium ions of photosynthetic oxygen evolution, *Biochim. Biophys. Acta* 1102, 269-352.
- [2] Grundmeier, A., and Dau, H. (2012) Structural models of the manganese complex of photosystem II and mechanistic implications, *Biochim. Biophys. Acta* 1817, 88-105.
- [3] McEvoy, J. P., and Brudvig, G. W. (2006) Water-splitting chemistry of photosystem II, *Chem. Rev.* 106, 4455-4483.
- [4] Vinyard, D. J., Ananyev, G. M., and Dismukes, G. C. (2013) Photosystem II: the reaction center of oxygenic photosynthesis, *Annu. Rev. Biochem.* 82, 577-606.
- [5] Hillier, W., and Messinger, J. (2005) Mechanism of photosynthetic oxygen production, In *Photosystem II: The Light-Driven Water: Plastoquinone Oxidoreductase* (Wydrzynski, T. J., and Satoh, K., Eds.), pp 567-608, Springer, Dordrecht, The Netherlands.
- [6] Renger, G. (2012) Photosynthetic water splitting: Apparatus and mechanism, In *Photosynthesis: Plastid Biology, Energy Conversion and Carbon Assimilation* (Eaton-Rye, J. J., Tripathy, B. C., and Sharkey, T. D., Eds.), pp 359-414, Springer, Dordrecht, The Netherlands.
- [7] Messinger, J., Noguchi, T., and Yano, J. (2011) Photosynthetic O₂ evolution, In *Molecular solar fuels* (Wydrzynski, T. J., and Hillier, W., Eds.), pp 163-207, Royal Society of Chemistry, Cambridge, U.K.
- [8] Renger, G., and Holzwarth, A. R. (2005) Primary electron transfer, In *Photosystem II: The Light-Driven Water: Plastoquinone Oxidoreductase* (Wydrzynski, T. J., and Satoh, K., Eds.), pp 139-175, Springer, Dordrecht, The Netherlands.
- [9] Umena, Y., Kawakami, K., Shen, J. R., and Kamiya, N. (2011) Crystal structure of oxygen-evolving photosystem II at a resolution of 1.9 Å, *Nature* 473, 55-60.
- [10] Suga, M., Akita, F., Hirata, K., Ueno, G., Murakami, H., Nakajima, Y., Shimizu, T., Yamashita, K., Yamamoto, M., Ago, H., and Shen, J. R. (2015) Native structure of photosystem II at 1.95 Å resolution viewed by femtosecond X-ray pulses, *Nature* 517, 99-103.
- [11] Diner, B. A., and Britt, R. D. (2005) The redox-active tyrosines Y_Z and Y_D, In *Photosystem II: The Light-Driven Water: Plastoquinone Oxidoreductase* (Wydrzynski, T. J., and Satoh,

- K., Eds.), pp 207-233, Springer, Dordrecht, The Netherlands.
- [12] Renger, G. (2012) Mechanism of light induced water splitting in Photosystem II of oxygen evolving photosynthetic organisms, *Biochim. Biophys. Acta* 1817, 1164-1176.
- [13] Styring, S., Sjöholm, J., and Mamedov, F. (2012) Two tyrosines that changed the world: Interfacing the oxidizing power of photochemistry to water splitting in photosystem II, *Biochim. Biophys. Acta* 1817, 76-87.
- [14] Babcock, G. T., Barry, B. A., Debus, R. J., Hoganson, C. W., Atamian, M., McIntosh, L., Sithole, I., and Yocum, C. F. (1989) Water oxidation in photosystem II: From radical chemistry to multielectron chemistry, *Biochemistry* 28, 9557-9565.
- [15] Faller, P., Debus, R. J., Brettel, K., Sugiura, M., Rutherford, A. W., and Boussac, A. (2001) Rapid formation of the stable tyrosyl radical in photosystem II, *Proc. Natl. Acad. Sci. U. S. A.* 98, 14368-14373.
- [16] Faller, P., Rutherford, A. W., and Debus, R. J. (2002) Tyrosine D oxidation at cryogenic temperature in photosystem II, *Biochemistry* 41, 12914-12920.
- [17] Faller, P., Goussias, C., Rutherford, A. W., and Un, S. (2003) Resolving intermediates in biological proton-coupled electron transfer: a tyrosyl radical prior to proton movement, *Proc. Natl. Acad. Sci. U. S. A.* 100, 8732-8735.
- [18] Rutherford, A. W., Boussac, A., and Faller, P. (2004) The stable tyrosyl radical in photosystem II: why D?, *Biochim. Biophys. Acta* 1655, 222-230.
- [19] Berthomieu, C., and Hienerwadel, R. (2005) Vibrational spectroscopy to study the properties of redox-active tyrosines in photosystem II and other proteins, *Biochim. Biophys. Acta* 1707, 51-66.
- [20] Havelius, K. G., and Styring, S. (2007) pH dependent competition between Y_Z and Y_D in photosystem II probed by illumination at 5 K, *Biochemistry* 46, 7865-7874.
- [21] Hammarström, L., and Styring, S. (2011) Proton-coupled electron transfer of tyrosines in Photosystem II and model systems for artificial photosynthesis: the role of a redox-active link between catalyst and photosensitizer, *Energy Environ. Sci.* 4, 2379-2388.
- [22] Matsuoka, H., Shen, J. R., Kawamori, A., Nishiyama, K., Ohba, Y., and Yamauchi, S. (2011) Proton-coupled electron-transfer processes in photosystem II probed by highly resolved g-anisotropy of redox-active tyrosine Y_Z, *J. Am. Chem. Soc.* 133, 4655-4660.
- [23] Saito, K., Shen, J. R., Ishida, T., and Ishikita, H. (2011) Short hydrogen bond between redox-active tyrosine Y_Z and D1-His190 in the photosystem II crystal structure, *Biochemistry* 50, 9836-9844.
- [24] Chatterjee, R., Coates, C. S., Milikisiyants, S., Lee, C. I., Wagner, A., Poluektov, O. G., and Lakshmi, K. V. (2013) High-frequency electron nuclear double-resonance spectroscopy studies of the mechanism of proton-coupled electron transfer at the tyrosine-D residue of

- photosystem II, *Biochemistry* 52, 4781-4790.
- [25] Saito, K., Rutherford, A. W., and Ishikita, H. (2013) Mechanism of tyrosine D oxidation in Photosystem II, *Proc. Natl. Acad. Sci. U.S.A.* 110, 7690-7695.
- [26] Dixon, W. T., and Murphy, D. (1976) Determination of the acidity constants of some phenol radical cations by means of electron spin resonance, *J. Chem. Soc., Faraday Trans. 2* 72, 1221-1230.
- [27] Rappaport, F., Boussac, A., Force, D. A., Peloquin, J., Brynda, M., Sugiura, M., Un, S., Britt, R. D., and Diner, B. A. (2009) Probing the coupling between proton and electron transfer in photosystem II core complexes containing a 3-fluorotyrosine, *J. Am. Chem. Soc.* 131, 4425-4433.
- [28] Suga, M., Akita, F., Sugahara, M., Kubo, M., Nakajima, Y., Nakane, T., Yamashita, K., Umena, Y., Nakabayashi, M., Yamane, T., Nakano, T., Suzuki, M., Masuda, T., Inoue, S., Kimura, T., Nomura, T., Yonekura, S., Yu, L. J., Sakamoto, T., Motomura, T., Chen, J. H., Kato, Y., Noguchi, T., Tono, K., Joti, Y., Kameshima, T., Hatsui, T., Nango, E., Tanaka, R., Naitow, H., Matsuura, Y., Yamashita, A., Yamamoto, M., Nureki, O., Yabashi, M., Ishikawa, T., Iwata, S., and Shen, J. R. (2017) Light-induced structural changes and the site of O=O bond formation in PSII caught by XFEL, *Nature* 543, 131-135.
- [29] Tanaka, A., Fukushima, Y., and Kamiya, N. (2017) Two different structures of the oxygen-evolving complex in the same polypeptide frameworks of photosystem II, *J. Am. Chem. Soc.* 139, 1718-1721.
- [30] Young, I. D., Ibrahim, M., Chatterjee, R., Gul, S., Fuller, F., Koroidov, S., Brewster, A. S., Tran, R., Alonso-Mori, R., Kroll, T., Michels-Clark, T., Laksmono, H., Sierra, R. G., Stan, C. A., Hussein, R., Zhang, M., Douthit, L., Kubin, M., de Lichtenberg, C., Long Vo, P., Nilsson, H., Cheah, M. H., Shevela, D., Saracini, C., Bean, M. A., Seuffert, I., Sokaras, D., Weng, T. C., Pastor, E., Weninger, C., Fransson, T., Lassalle, L., Brauer, P., Aller, P., Docker, P. T., Andi, B., Orville, A. M., Glowacka, J. M., Nelson, S., Sikorski, M., Zhu, D., Hunter, M. S., Lane, T. J., Aquila, A., Koglin, J. E., Robinson, J., Liang, M., Boutet, S., Lyubimov, A. Y., Uervirojnangkoorn, M., Moriarty, N. W., Liebschner, D., Afonine, P. V., Waterman, D. G., Evans, G., Wernet, P., Dobbek, H., Weis, W. I., Brunger, A. T., Zwart, P. H., Adams, P. D., Zouni, A., Messinger, J., Bergmann, U., Sauter, N. K., Kern, J., Yachandra, V. K., and Yano, J. (2016) Structure of photosystem II and substrate binding at room temperature, *Nature* 540, 453-457.
- [31] Joliot, P., Barbieri, G., and Chabaud, R. (1969) A new model of photochemical centers in system II, *Photochem. Photobiol.* 10, 309-329.
- [32] Kok, B., Forbush, B., and McGloin, M. (1970) Cooperation of charges in photosynthetic O₂ evolution-I. A linear four step mechanism, *Photochem. Photobiol.* 11, 457-475.

- [33] Fowler, C. F. (1977) Proton evolution from photosystem II. stoichiometry and mechanistic considerations, *Biochim. Biophys. Acta* 462, 414-421.
- [34] Schlodder, E., and Witt, H. T. (1999) Stoichiometry of proton release from the catalytic center in photosynthetic water oxidation. Reexamination by a glass electrode study at pH 5.5-7.2, *J. Biol. Chem.* 274, 30387-30392.
- [35] Suzuki, H., Sugiura, M., and Noguchi, T. (2009) Monitoring proton release during photosynthetic water oxidation in photosystem II by means of isotope-edited infrared spectroscopy, *J. Am. Chem. Soc.* 131, 7849-7857.
- [36] Mäntele, W. (1993) Reaction-induced infrared difference spectroscopy for the study of protein function and reaction mechanisms, *Trends Biochem. Sci.* 18, 197-202.
- [37] Harrick, N. J. (1960) Surface chemistry from spectral analysis of totally internally reflected radiation, *J. Phys. Chem.* 64, 1110-1114.
- [38] Fahrenfort, J. (1961) Attenuated total reflection: A new principle for the production of useful infra-red reflection spectra of organic compounds, *Spectrochim. Acta* 17, 698-&.
- [39] Goormaghtigh, E., Raussens, V., and Ruyschaert, J. M. (1999) Attenuated total reflection infrared spectroscopy of proteins and lipids in biological membranes, *Biochim. Biophys. Acta* 1422, 105-185.
- [40] Okubo, T., and Noguchi, T. (2007) Selective detection of the structural changes upon photoreactions of several redox cofactors in photosystem II by means of light-induced ATR-FTIR difference spectroscopy, *Spectrochim. Acta, Part A* 66, 863-868.
- [41] Iizasa, M., Suzuki, H., and Noguchi, T. (2010) Orientations of carboxylate groups coupled to the Mn cluster in the photosynthetic oxygen-evolving center as studied by polarized ATR-FTIR spectroscopy, *Biochemistry* 49, 3074-3082.
- [42] Zscherp, C., and Barth, A. (2001) Reaction-induced infrared difference spectroscopy for the study of protein reaction mechanisms, *Biochemistry* 40, 1875-1883.
- [43] Berthomieu, C., and Hienerwadel, R. (2009) Fourier transform infrared (FTIR) spectroscopy, *Photosynthesis Res.* 101, 157-170.
- [44] Noguchi, T., and Berthomieu, C. (2005) Molecular analysis by vibrational spectroscopy, In *Photosystem II: The Light-Driven Water: Plastoquinone Oxidoreductase*. (Wydrzynski, T., and Satoh, K., Eds.), Springer, Dordrecht, The Netherlands.
- [45] Chu, H. A. (2013) Fourier transform infrared difference spectroscopy for studying the molecular mechanism of photosynthetic water oxidation, *Front. Plant Sci.* 4, 146.
- [46] Debus, R. J. (2015) FTIR studies of metal ligands, networks of hydrogen bonds, and water molecules near the active site Mn₄CaO₅ cluster in Photosystem II, *Biochim. Biophys. Acta* 1847, 19-34.
- [47] Noguchi, T. (2015) Fourier transform infrared difference and time-resolved infrared

- detection of the electron and proton transfer dynamics in photosynthetic water oxidation, *Biochim. Biophys. Acta* 1847, 35-45.
- [48] Szabo, A., and Ostlund, N. S. (1996) *Modern Quantum Chemistry: Introduction to Advanced Electronic Structure Theory*, Courier Corporation.
- [49] Parr, R. G. (1980) Density functional theory of atoms and molecules, In *Horizons of Quantum Chemistry* (Fukui, K., and Pullman, B., Eds.), pp 5-15, Springer, Dordrecht, The Netherlands.
- [50] Hasegawa, K., Ono, T., and Noguchi, T. (2000) Vibrational spectra and ab initio DFT calculations of 4-methylimidazole and its different protonation forms: Infrared and Raman markers of the protonation state of a histidine side chain, *J. Phys. Chem. B* 104, 4253-4265.
- [51] O'Malley, P. J. (2002) Density functional calculations modelling tyrosine oxidation in oxygenic photosynthetic electron transfer, *Biochim. Biophys. Acta* 1553, 212-217.
- [52] Ashizawa, R., and Noguchi, T. (2014) Effects of hydrogen bonding interactions on the redox potential and molecular vibrations of plastoquinone as studied using density functional theory calculations, *Phys. Chem. Chem. Phys.* 16, 11864-11876.
- [53] Warshel, A., and Levitt, M. (1976) Theoretical studies of enzymic reactions: dielectric, electrostatic and steric stabilization of the carbonium ion in the reaction of lysozyme, *J. Mol. Biol.* 103, 227-249.
- [54] Maseras, F., and Morokuma, K. (1995) IMOMM: A new integrated ab initio+ molecular mechanics geometry optimization scheme of equilibrium structures and transition states, *J. Comput. Chem.* 16, 1170-1179.
- [55] Vreven, T., Byun, K. S., Komaromi, I., Dapprich, S., Montgomery, J. A., Morokuma, K., and Frisch, M. J. (2006) Combining quantum mechanics methods with molecular mechanics methods in ONIOM, *J. Chem. Theory Comput.* 2, 815-826.

Hydrogen bond structure of redox active tyrosines in photosystem II

2.1. Introduction

On the electron donor side of PSII, P680⁺ first oxidizes the redox-active tyrosine Y_Z (D1-Tyr161) and then Y_Z oxidizes the Mn cluster, where water is oxidized via a light-driven cycle of five intermediates called S_i states (*i* = 0–4).^{1–7} When Y_Z is oxidized by P680⁺, the phenolic proton is released. The X-ray structure of PSII revealed that the phenolic oxygen of Y_Z is within hydrogen bonding distance of the neighboring D1-His190 (Figure 2.1A).^{8–10} In particular, the recent high-resolution (1.9 Å) X-ray structure exhibited a significantly short distance of 2.46 Å between the Y_Z oxygen and the N τ atom of D1-His190,¹⁰ which was reproduced by the quantum mechanics/molecular mechanics (QM/MM) calculation, showing the presence of a strong hydrogen bond with a single well potential.¹¹ Upon oxidation, the proton of Y_Z is thought to shift to N τ of D1-His190 along this strong hydrogen bond, which is the basic mechanism of the fast

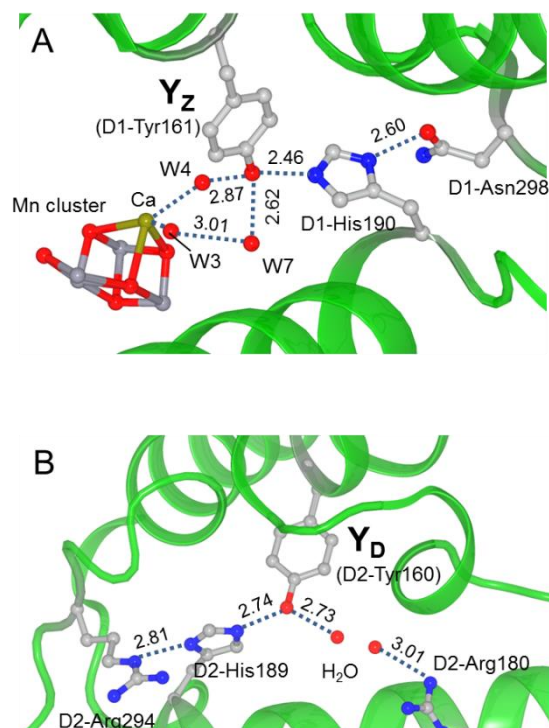


Figure 2.1 Structures of the hydrogen bond networks around Y_Z (A) and Y_D (B) deduced from the X-ray crystallographic structure of photosystem II at 1.9 Å resolution (PDB entry 3ARC).

proton-coupled electron transfer (PCET) of Y_Z .¹¹⁻¹⁵ Whether the positive charge remains on this His residue during the lifetime of Y_Z^\bullet has been a matter of debate.¹⁵⁻¹⁹ Although several lines of data supported the presence of a positive charge near Y_Z^\bullet ,^{15, 16, 20, 21} further direct evidence is necessary to reach the final conclusion.

The high-resolution X-ray structure¹⁰ also showed that Y_Z interacts with the Mn cluster via a water cluster that consists of several water molecules (Figure 2.1A). Water W4 (the nomenclature of the water molecules and Mn atoms follows that of Umena et al.¹⁰) directly connects the Y_Z oxygen and the Ca atom, while W3, another water ligand to Ca, interacts with Y_Z through W7. W2, the water ligand to Mn4, also interacts with Y_Z through the water molecules, W5, W6, W3, and W7. The X-ray structure further showed that Y_Z is located in a hydrogen bond network connecting the Mn cluster to the lumen, which has been suggested to be one of the proton exit or water access pathways.^{10, 22-24} It is thus possible that Y_Z functions as a proton transfer mediator in this pathway during water oxidation.

Another redox-active tyrosine Y_D (D2-Tyr160) in PSII (Figure 2.1B), which is symmetrically related to Y_Z , also donates an electron to $P680^+$. The structure of the Y_D site is very similar to that of Y_Z . The phenolic oxygen of Y_D is within hydrogen bonding distance of D2-His189 and a water molecule (Figure 2.1B). However, the rate of oxidation of Y_D is much slower than that of Y_Z , and the resultant Y_D^\bullet radical is considerably stable at room temperature.^{12, 15} Thus, Y_D functions only as a peripheral electron donor to $P680^+$ and is not directly related to water oxidation. The lower redox potential of Y_D (700–800 mV)^{25, 26} compared with that of Y_Z (900–1000 mV)^{26, 27} and the proton release mechanism involving a mobile water²⁸ have been suggested as causes for its radical stability and the slow kinetics of the redox reaction.

One of the major questions relevant to Y_Z function is its role in the water oxidation mechanism.^{14, 15, 17, 29, 30} Does Y_Z function only as an electron mediator between $P680$ and the Mn cluster, or is it more deeply involved in the proton release processes during water oxidation? If the latter is the case, what is the mechanism of the PCET involving Y_Z and the Mn cluster, and does the proton pathway involving Y_Z actually function in some of the S-state transitions? With this respect, it is important to answer the question of whether a proton is released from D1-His190 upon Y_Z oxidation or a positive charge is trapped on this His throughout the lifetime of Y_Z^\bullet ? If the proton is released into the bulk, Y_Z^\bullet can abstract a proton of substrate water through the hydrogen bond network concomitant with electron transfer, as was previously proposed as a hydrogen abstraction model by Babcock and co-workers.¹⁷ In addition, it has been argued that a positive charge near Y_Z^\bullet triggers the release of the proton from substrate water by electrostatic interaction with the Mn cluster.²⁹⁻³³ It is also crucial to obtain the information about the protonation structures and hydrogen bonding interactions of Y_Z and the coupled His to argue the possibility of transfer of the proton through Y_Z for releasing a proton from the Mn center.

In this study, we have investigated the hydrogen-bonded structure of the Y_Z -His moiety and its change upon photooxidation using light-induced Fourier transform infrared (FTIR) difference spectroscopy. The Y_Z^\bullet -minus- Y_Z FTIR difference spectrum (hereafter designated the Y_Z^\bullet/Y_Z difference spectrum) in the 1800–1000 cm^{-1} region was previously reported by Berthomieu et al.³⁴ Here, we have obtained Y_Z^\bullet/Y_Z spectra that include the higher-frequency region that involves the vibrations of protons. The spectra were analyzed by isotopic substitutions and pH changes, and also by comparison with a Y_D^\bullet/Y_D difference spectrum. Furthermore, we have performed quantum chemical calculations using density functional theory (DFT) and QM/MM methods for the Y_Z -His and Y_D -His pairs to interpret the experimental spectra and obtain structural information. The proton trapped between Y_Z and D1-His190 upon its photooxidation was directly detected as a broad N-H stretching band of the His, revealing a large proton polarizability. Information about the protonation and hydrogen-bonded structures of Y_Z and D1-His190 and the nearby hydrogen bond network was also obtained. On the basis of the results, the roles of Y_Z and the coupled His in the PCET mechanism of water oxidation are discussed.

2.2. Materials and Methods

Preparation of PSII Core Complexes. The thermophilic cyanobacterium *Thermosynechococcus elongates* 47-H strain, in which a six-histidine tag was introduced onto the C-terminus of the CP47 subunit, was grown in a BG11 medium³⁵ supplemented with 10 mM Hepes (pH 7.5) by stirring and bubbling with air containing 3% (v/v) CO_2 .³⁶ Global ^{15}N substitution was performed by culturing cells in a BG11 medium containing $\text{Na}^{15}\text{NO}_3$ (SI Science Co., Ltd.; 99.7 atom % ^{15}N) and CoCl_2 instead of unlabeled NaNO_3 and $\text{Co}(\text{NO}_3)_2$, respectively.

Oxygen-evolving PSII complexes were purified using the method by Boussac et al.³⁷ with some modifications. Cells were washed once with a 40 mM sodium phosphate buffer (pH 7.0) containing 1 mM EDTA and then suspended in a buffer containing 40 mM Mes (pH 6.5), 10 mM CaCl_2 , 10 mM MgCl_2 , 10% (w/v) glycerol, and 1 M betaine (buffer A). The cells were disrupted in buffer A in the presence of 0.2% (w/v) bovine serum albumin, 1 mM benzamidine, 1 mM aminocaproic acid, and 50 $\mu\text{g}/\text{mL}$ DNase I by agitation with glass beads (100 μm in diameter), repeating the on (10 s) and off (3 min) cycle 19 times on ice in the dark. The lysate was diluted with an equal volume of a buffer containing 40 mM Mes- NaOH (pH 6.5), 10 mM CaCl_2 , and 10 mM MgCl_2 . Unbroken cells were removed by centrifugation at 3000g for 5 min, and the supernatant was subsequently centrifuged at 48000g for 20 min. Obtained thylakoid membranes suspended in buffer A were solubilized with 1% (w/v) n-dodecyl β -D-maltoside (DM) at a chlorophyll (Chl) concentration of 1.0 mg/mL while being gently stirred for 10 min on ice in the dark. After centrifugation at 48000g for 10 min, the resultant supernatant was applied to a Ni^{2+}

affinity column equilibrated with buffer A containing 20 mM imidazole, 100 mM NaCl, and 0.03% DM. PSII complexes were eluted with buffer A containing 200 mM imidazole, 100 mM NaCl, and 0.03% DM and then washed with buffer A containing 0.03% DM by ultrafiltration (Vivaspin 20, Sartorium Stedim, 100 kDa molecular mass cutoff). The O₂ evolution activity of the obtained PSII core complexes with 0.5 mM 2,6-dichloro-1,4-benzoquinone as an electron acceptor was 2400–2700 μmol of O₂ (mg of Chl)⁻¹ h⁻¹. Mn depletion was performed via a 10 mM NH₂OH treatment for 30 min at room temperature, followed by a wash with buffer A containing 0.03% DM by ultrafiltration (Vivaspin 20).

FTIR Measurements. For Y_Z[•]/Y_Z FTIR measurements, Mn-depleted PSII core complexes were suspended in a buffer that consisted of 20 mM Mes (pH 6.5 or 5.5) or 20 mM Hepes (pH 7.5) containing 40 mM sucrose, 10 mM NaCl, 5 mM MgCl₂, and 0.06% DM and concentrated to ~6 mg/mL Chl by ultrafiltration (Vivaspin 500, 100 kDa molecular mass cutoff). Four microliters of the suspension was mixed with 1 μL of 100 mM potassium ferricyanide and then dried on a BaF₂ plate (13 mm in diameter) under a N₂ gas flow. The sample was sandwiched with another BaF₂ plate with 0.8 μL of H₂O. For the preparation of samples in D₂O, the dried core complexes were resuspended in 3 μL of D₂O and dried again. This process was repeated several times, and finally, the sample was sandwiched with 0.8 μL of D₂O. The sample temperature was adjusted to 250 K in a cryostat (Oxford DN1704).

Flash-induced FTIR spectra were recorded on a Bruker IFS-66/S spectrophotometer equipped with an MCT detector (D313-L). Flash illumination was performed using a Qswitched Nd:YAG laser (INDI-40-10; 532 nm; ~7 ns full width at half-maximum; ~7 mJ pulse⁻¹ cm⁻²). For Y_Z[•]/Y_Z spectra, single-beam spectra with 50 scans (25 s accumulation) were recorded twice before and once after single-flash illumination. The measurement was repeated with a dark interval of 225 s between measurements (flash illumination every 5 min). The spectra of 350–1000 loops recorded using one to four samples were averaged to calculate a light-minus-dark difference spectrum as a Y_Z[•]/Y_Z difference spectrum and a dark-minus-dark difference spectrum before illumination representing the baseline and noise level.

The Y_D[•]/Y_D FTIR spectrum was measured with the method described previously³⁸ with some modification. Briefly, 5 μL of a suspension of the Mn-depleted PSII complexes (3 mg/mL Chl) in a pH 6.5 Mes buffer (10 mM Mes, 5 mM NaCl, and 0.06% DM) was mixed with 1 μL of 20 mM potassium ferricyanide and 1 μL of 20 mM potassium ferrocyanide. The sample was dried on a BaF₂ plate to make a film and then sealed with another BaF₂ plate with 2 μL of a 40% (v/v) glycerol/H₂O mixture without touching the sample. H/D exchange was performed by repeating drying and resuspension in D₂O, which was similar to the process used for samples for Y_Z measurements. The sample temperature was adjusted to 283 K by circulating cold water in a copper holder. Single-beam spectra with 100 scans (50 s accumulation) were recorded twice

before and once after five flashes (1 Hz) from the Nd:YAG laser, and the measurement was repeated with a dark interval of 750 s. The spectra of 54 loops were averaged to calculate a light-minus-dark difference spectrum as a Y_D^\bullet/Y_D spectrum and a dark-minus-dark difference spectrum as the baseline.

Quantum Chemical Calculations. Quantum chemical calculations were performed using the Gaussian09 program package.³⁹ For DFT calculations for the Tyr-His models, the B3LYP functional^{40, 41} with the 6-31++G(d,p) basis set was used to optimize the geometries and calculate the vibrational frequencies and IR intensities. QM/MM calculations were performed using the ONIOM (our own n-layered integrated molecular orbital and molecular mechanics) method.⁴² For Y_Z calculations, the atomic coordinates of amino acid residues, water molecules, the Mn cluster, and Cl^- ions located within 20 Å of the Ca atom were taken from the X-ray structure of the PSII complexes at 1.9 Å resolution (PDB entry 3ARC¹⁰). The hydrogen atoms were generated and optimized using Amber. The geometry of the Mn cluster and surrounding groups (Cl^- ions, amino acid ligands to Mn, Ca, and Cl^- , Y_Z , D1-His190, D1-Asp61, W1–W7, HOH446, and HOH442) was then optimized as a QM region fixing other atoms as a MM region. In this optimization, we used the model of the Mn cluster with (Mn1, Mn2, Mn3, Mn4) = (III, IV, IV, III), W2 = H₂O, and O5 = O²⁻.⁴³ Using the obtained coordinates and atomic partial charges, further geometry optimization and vibrational analysis were performed for Y_Z and the surrounding groups (D1-His190, D1-Asn298, D1-Gln165, Ca, W3–W7, HOH387, HOH394, HOH398, HOH778, HOH923, and HOH1117) as a QM region, fixing the other atoms in the MM region using ONIOM (B3LYP:Amber). As basis sets in the QM calculation, LANL2DZ is used for Ca and Mn and 6-31++G(d,p) for other atoms. For Y_D calculation, the atomic coordinates of amino acid residues and water molecules located within 20 Å of Y_D were taken from the X-ray structure (PDB entry 3ARC¹⁰), and then the hydrogen atoms were generated and optimized using Amber. Geometry optimization and vibrational analysis were performed for Y_D and the surrounding groups (D2-His189, D2-Arg294, D2-Arg180, and HOH1) as a QM region, fixing the other atoms in the MM region using ONIOM [B3LYP/6-31++G(d,p):Amber].

Calculated vibrational frequencies by the DFT and ONIOM methods were scaled to adjust the CO frequencies of the Y_Z^\bullet and Y_D^\bullet radicals to the experimental frequencies 1514 and 1504 cm⁻¹, respectively. The scaling factors for the Y_Z -His and Y_D -His pairs were 0.979 and 0.987, respectively, in the DFT calculations and 0.968 and 0.973, respectively, in the ONIOM calculations. The calculated frequencies of free 4-methylimidazole (4-MeIm) were scaled by a factor of 0.980 following the previous DFT calculation of the various protonation forms of 4-MeIm.⁴⁴

2.3. Results

An FTIR difference spectrum (3000–1000 cm^{-1}) of Y_Z upon its photooxidation (Y_Z^\bullet/Y_Z spectrum), which was measured using the Mn-depleted PSII core complexes from *Thermosynechococcus elongatus* at pH 6.5, is shown in Figure 2.2 (solid line) together with a dark/dark spectrum (dotted line) representing the baseline. The large peaks at 2116 and 2038 cm^{-1} arise from the CN stretching vibrations of ferricyanide and ferrocyanide, respectively, reflecting the flow of an electron from the electron donor side to the acceptor side. Note that small peaks at the same positions in opposite signs in the dark/dark spectrum are due to the residual back reaction ($\sim 4\%$ of the forward reaction) during the measurements of the two dark spectra before illumination (see Materials and Methods). The Y_Z^\bullet/Y_Z spectrum in the 1800–1000 cm^{-1} region (expanded in Figure 2.3) is very similar to the spectrum previously reported by Berthomieu et al.³⁴ using the Mn-depleted preparations of the PSII core complexes from *Synechocystis sp.* PCC 6803 and PSII enriched membranes from spinach. The positive band at 1514 cm^{-1} arises from the CO stretching (νCO) vibration of the oxidized Y_Z^\bullet radical,^{34, 45} while the corresponding band of Y_D^\bullet was observed at 1504 cm^{-1} (Figure 2.3).^{38, 46} Berthomieu et al.³⁴ previously assigned a negative band at 1255 cm^{-1} in their Y_Z^\bullet/Y_Z spectrum to the COH bending (δCOH) vibration of reduced Y_Z and a small negative peak at 1279 cm^{-1} to its νCO vibration. We did not observe the

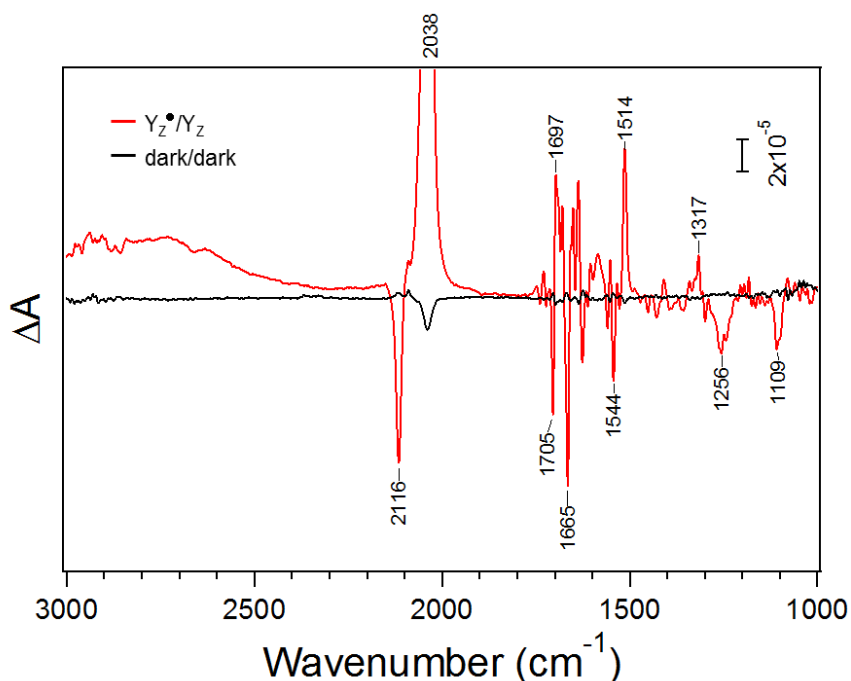


Figure 2.2 Light-induced Y_Z^\bullet/Y_Z FTIR difference spectrum (3000–1000 cm^{-1}) of the PSII core complexes from *T. elongatus* (red line) together with a dark-minus-dark spectrum representing the baseline (black line).

latter peak and prefer the assignment of the relatively broad band at 1256 cm^{-1} (Figure 2.3) to the overlap of the δCOH and νCO vibrations, which are more or less coupled with each other.^{47, 48} Indeed, in D_2O (Figure 2.3), a narrower band was left at an upshifted position of 1262 cm^{-1} , which is assigned to the pure νCO vibration decoupled from the δCOH vibration.⁴⁸ The differential signal at $1705/1697\text{ cm}^{-1}$ was temporally assigned to the electrochromic shift of the keto CO band of P680 by Y_Z oxidation,³⁴ while most of the other bands in the $1700\text{--}1600\text{ cm}^{-1}$ region probably arise from the amide I vibrations (CO stretches) of backbone amides due to the conformational changes of the polypeptide main chains surrounding Y_Z . The amide II bands (NH bends and CN stretches) coupled to the amide I bands were observed at $1560, 1553, \text{ and } 1544\text{ cm}^{-1}$, which were confirmed by the downshifts to $1545, 1538, \text{ and } 1530\text{ cm}^{-1}$, respectively, by global ^{15}N

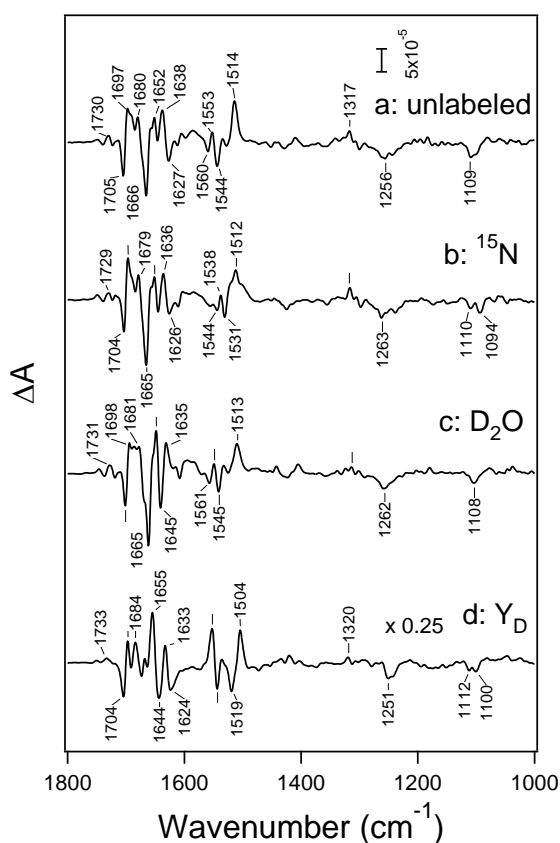


Figure 2.3 $\text{Y}_Z^\bullet/\text{Y}_Z$ FTIR difference spectra ($1800\text{--}1000\text{ cm}^{-1}$) of unlabeled (a) and globally ^{15}N -labeled (b) PSII complexes and of PSII complexes in D_2O (c), in comparison with a $\text{Y}_D^\bullet/\text{Y}_D$ difference spectrum (d). Ticks without labels indicate the same frequencies as in spectrum a. The spectra were measured in buffers at pH or pD 6.5. The intensity of the $\text{Y}_D^\bullet/\text{Y}_D$ difference spectrum (d) was multiplied by 0.25 because of its intensity greater than that of the $\text{Y}_Z^\bullet/\text{Y}_Z$ spectrum due to the rather stable formation of Y_D^\bullet .

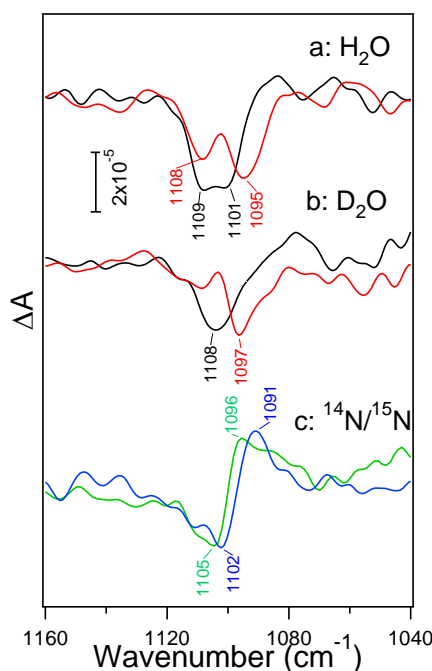


Figure 2.4 His CN stretching region of the Y_Z^\bullet/Y_Z FTIR difference spectra of unlabeled (black lines) and ^{15}N -labeled (red lines) PSII complexes in H_2O (a) and D_2O (b). (c) Unlabeled-minus- ^{15}N -labeled double-difference spectra in H_2O (blue) and D_2O (green). The spectra were measured in buffers at pH or pD 6.5.

substitution (Figure 2.3). The ^{15}N substitution also downshifted a negative band from 1101 to 1095 cm^{-1} (Figure 2.3), indicative of the presence of the His CN vibration^{44, 49, 50} around this position (the expanded view of this region is presented in Figure 2.4). Indeed, the ^{14}N -minus- ^{15}N double-difference spectrum (Figure 2.4, blue line) exhibited a differential signal with peaks at 1102 and 1091 cm^{-1} . It was previously shown that the extent of the deuteration shift of the His CN stretch is dependent on the protonation structure.⁴⁴ The His CN region of the Y_Z^\bullet/Y_Z spectra measured in D_2O showed a negative band at 1108 cm^{-1} in the unlabeled sample and at 1097 cm^{-1} in the ^{15}N -substituted sample (Figure 2.4), providing a differential signal at $1105/1096\text{ cm}^{-1}$ in the ^{14}N -minus- ^{15}N double difference spectrum (Figure 2.4, green line). Thus, the His CN signal was only slightly upshifted (by $3\text{--}5\text{ cm}^{-1}$) upon deuteration.

The higher-frequency region above 2200 cm^{-1} of the Y_Z^\bullet/Y_Z spectrum has not been reported previously. A broad positive feature around 2800 cm^{-1} , which begins from $\sim 2300\text{ cm}^{-1}$ and continues at least to 3000 cm^{-1} (the region above 3000 cm^{-1} could not be observed because of saturation by bulk water absorption), appeared in the spectrum. On this broad feature, small peaks were observed at 2902, 2882, 2856, 2659, and 2630 cm^{-1} , which downshifted to 2871, 2857,

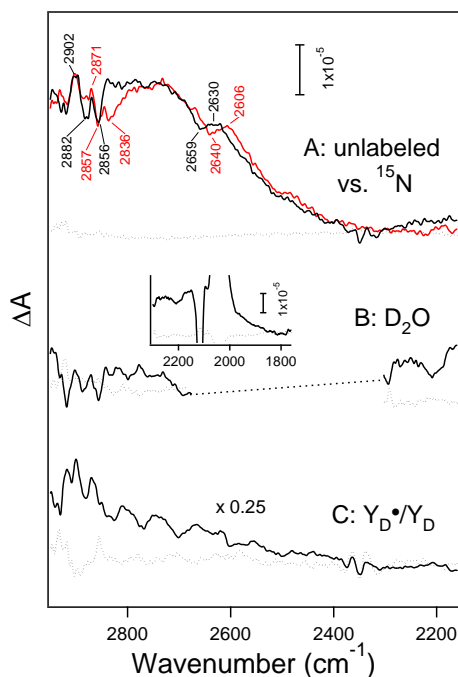


Figure 2.5 2900–2200 cm^{-1} region of the Y_Z^\bullet/Y_Z FTIR difference spectra of unlabeled (A, black line) and globally ^{15}N -labeled (A, red line) PSII complexes and of PSII complexes in D_2O (B), in comparison with a Y_D^\bullet/Y_D difference spectrum (C). The inset shows the 2300–1800 cm^{-1} region of the Y_Z^\bullet/Y_Z spectrum in D_2O . Dotted curves are dark-minus-dark spectra representing baselines. The region connected by a dashed line in spectrum c is saturated by the strong OD stretching bands of bulk D_2O . PSII samples are in buffers at pH or pD 6.5.

2836, 2640, and 2606 cm^{-1} , respectively, by 31–19 cm^{-1} upon global ^{15}N substitution (Figure 2.5). These ^{15}N -sensitive peaks in the 3000–2500 cm^{-1} region on the broad feature are similar to those previously observed in the Q_A^-/Q_A , Q_B^-/Q_B , and S_2/S_1 difference spectra,⁵⁰⁻⁵⁴ in which the peaks have been attributed to the Fermi resonance of the overtones and combinations of the vibrations of a His side chain with its NH stretching mode. The broad feature itself also downshifted by ~ 10 cm^{-1} upon ^{15}N substitution (Figure 2.5). Thus, it is highly likely that the broad feature with the Fermi resonance peaks originates from the NH stretching vibration of His. This NH assignment was supported by the observation that the broad band around 2800 cm^{-1} disappeared in D_2O (Figure 2.5), and instead, another broad band appeared around 2100 cm^{-1} overlapping the ferricyanide (2116 cm^{-1}) and ferrocyanide (2038 cm^{-1}) peaks (Figure 2.5, inset).

Figure 2.6 presents the Y_Z^\bullet/Y_Z spectra (A, 1800–1000 cm^{-1} ; B, 3000–2200 cm^{-1}) measured at pH 7.5 (a) and pH 5.5 (c) in comparison with the spectrum at pH 6.5. A drastic change was observed at pH 5.5. The broad band around 2800 cm^{-1} disappeared at this pH, leaving small

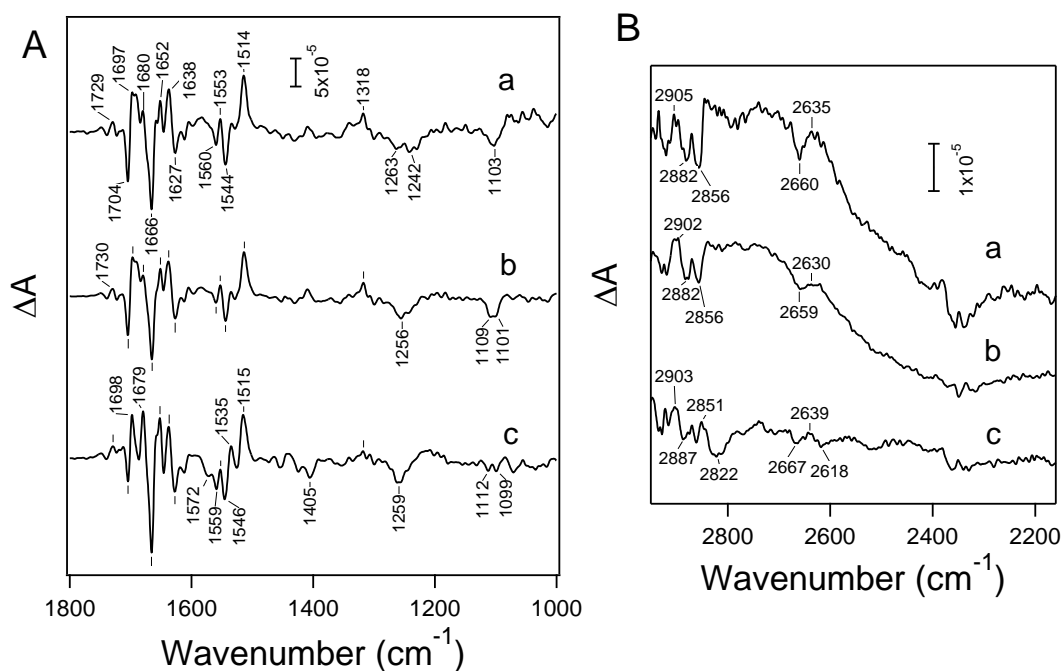


Figure 2.6. pH dependence of the Y_Z^\bullet/Y_Z FTIR difference spectra in the regions of 1800–1000 cm^{-1} (A) and 2900–2200 cm^{-1} (B) at pH 7.5 (a), pH 6.5 (b), and pH 5.5 (c). The spectra at pH 6.5 (b) are identical to the spectra in Figures 2.3 and 2.5 (black line). The structures around 2350 cm^{-1} (in spectra a and c in panel B) are artifacts of CO_2 absorption. Ticks without labels indicate the same frequencies as in spectrum a.

peaks at slightly different frequencies (Figure 2.6B, spectrum c), whereas the feature in this region was basically unchanged at pH 7.5 except for a slight increase in its intensity. The positive νCO peak of Y_Z^\bullet at 1514 cm^{-1} was virtually identical throughout the pH range of 5.5–7.5. However, the negative $\nu\text{CO}/\delta\text{COH}$ peak at 1256 cm^{-1} at pH 6.5 was shifted to 1259 cm^{-1} at pH 5.5, while it seems to be slightly broadened (or could be split into two peaks) at pH 7.5 (Figure 2.6A). These changes indicate that the hydrogen-bonded structures of Y_Z and the coupled D1-His190 are significantly different between pH 5.5 and 7.5, while the structure at pH 6.5 is mostly identical to that at pH 7.5 except for a minor mixing of the structure at pH 5.5.

Although the νCO frequency most straightforwardly reflects the hydrogen bond interaction of a Tyr side chain,⁴⁸ the coupling and overlap of the δCOH vibration hamper the identification of the original νCO frequency of reduced Y_Z in the Y_Z^\bullet/Y_Z FTIR spectra. To identify the pure νCO band of Y_Z at different pH values, Y_Z^\bullet/Y_Z spectra were measured in D_2O buffers to remove the δCOH vibration from the νCO region (Figure 2.7). The νCO band of reduced Y_Z was observed at 1263, 1262, and 1259 cm^{-1} at pD 7.5, 6.5, and 5.5, respectively (Figure 2.7C). Thus, the frequency downshifted by 4 cm^{-1} with a change in pD from 7.5 to 5.5, while only the 1 cm^{-1} shift was observed at pH 6.5. In contrast, the νCO band of Y_Z^\bullet at 1513 cm^{-1} did not change at all

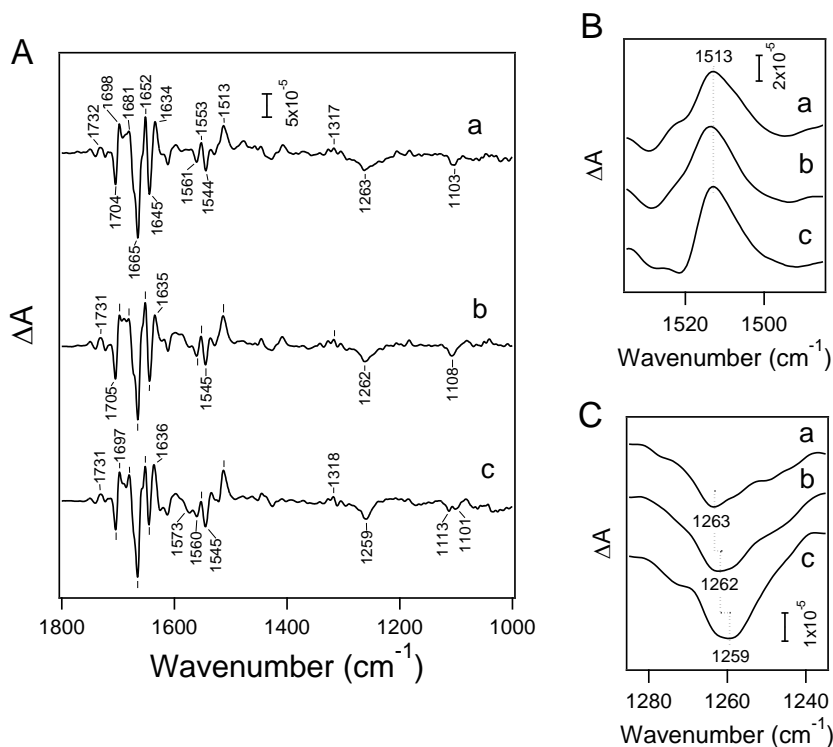


Figure 2.7 pD dependence of the Y_Z^\bullet/Y_Z FTIR difference spectra in D_2O buffers in the 1800–1000 cm^{-1} region (A) and the expanded views of the ν_{CO} bands of Y_Z^\bullet (B) and Y_Z (C) at pD 7.5 (a), pD 6.5 (b), and pD 5.5 (c). The spectrum at pD 6.5 (b) is identical to the spectrum in Figure 2.3. Ticks without labels indicate the same frequencies as in spectrum a.

(Figure 2.7B), in agreement with the result in H_2O (Figure 2.6A). These observations are consistent with the view that the hydrogen-bonded structure of reduced Y_Z is changed so that the C–O bond is weakened as the pH or pD is decreased from 7.5 to 5.5, whereas that of oxidized Y_Z^\bullet is unchanged.

To further investigate the origin of the broad feature in the Y_Z^\bullet/Y_Z spectrum and the hydrogen-bonded structures of Y_Z and Y_D and their coupled His, DFT and QM/MM calculations of the Y_Z -His and Y_D -His pairs were performed. In DFT calculations, *p*-cresol and 4-MeIm were used as models of Tyr and His side chains (Figure 2.8), respectively. The imidazole group of the His side chain has four protonation structures, i.e., the two neutral tautomers ($N\tau$ -H and $N\pi$ -H forms) and the protonated imidazolium cation and deprotonated imidazolate anion forms. Because there are many combinations of the protonation and hydrogen-bonded structures in Tyr-His complexes, we assumed the most probable models for Y_Z , Y_Z^\bullet , Y_D , and Y_D^\bullet , taking into consideration the interactions with surrounding amino acids, and examined the agreement of the calculated results with the experimental data. $N\pi$ of D1-His190 coupled to Y_Z is within hydrogen

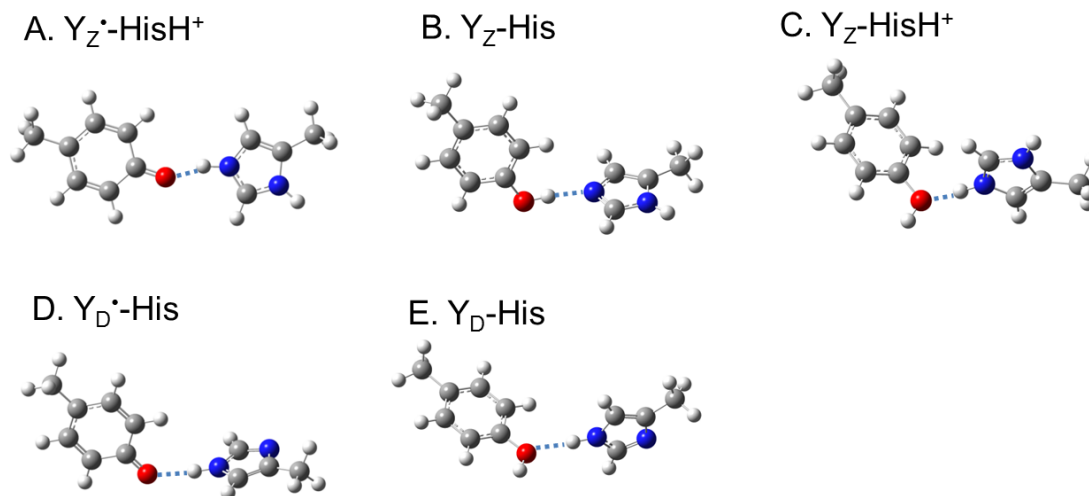


Figure 2.8 Optimized geometries of the model complexes of Y_Z and Y_D coupled with His obtained by DFT calculations: (A) Y_Z^\bullet -HisH⁺, (B) Y_Z -His, (C) Y_Z -HisH⁺, (D) Y_D^\bullet -His, and (E) Y_D -His. *p*-Cresol and 4-methylimidazole were used as models of $Y_{Z(D)}$ and a histidine side chain, respectively.

bonding distance (2.60 Å) of the amide oxygen of D1-Asn298 in the X-ray structure (Figure 2.1A),¹⁰ and hence, this $N\pi$ is probably protonated to form a hydrogen bond to D1-Asn298. Thus, in the oxidized Y_Z^\bullet state, D1-His190 most likely has a HisH⁺ cation form to have a hydrogen bond at $N\tau$ -H with the deprotonated oxygen of Y_Z^\bullet (Figure 2.8A). In the reduced Y_Z state, there are two possibilities. (1) His has a neutral $N\pi$ -H form, and the OH of Y_Z is hydrogen bonded to $N\tau$ of His (Figure 2.8B). (2) His has a HisH⁺ cation form, and its $N\tau$ -H is hydrogen bonded to the oxygen atom of Y_Z OH (Figure 2.8C). The latter structure may be realized at lower pH values. In contrast to Y_Z , $N\pi$ of D2-His189 coupled to Y_D is within hydrogen bonding distance (2.81 Å) of $N\epsilon$ of the guanidinium cation of D2-Arg294 (Figure 2.1B), and hence, $N\pi$ of this His is probably deprotonated to accept a hydrogen bond from this Arg.²⁸ Thus, D2-His189 probably has a neutral $N\tau$ -H form in both the Y_D^\bullet and Y_D states to donate a hydrogen bond to the deprotonated and protonated oxygen, respectively, of Tyr (Figure 2.8D,E).

In the QM/MM calculations of the Y_Z -His site, D1-Asn298, D1-Gln165, Ca, and 11 nearby water molecules along with Y_Z and D1-His190 were assigned to the QM region and the surrounding moieties (including the Mn and Cl⁻ ions) were treated as a MM region. Note that geometry optimization of the QM region in the reduced Y_Z state did not significantly change the positions of the heavy atoms, especially those of water oxygens, from the initial positions taken from the 1.9 Å X-ray structure¹⁰. For the Y_D -His site, Y_D , D2-His189, D2-Arg294, D2-Arg180, and a water molecule interacting Y_D were assigned to the QM region.

The calculated frequencies of the $N\tau$ -H stretching vibration of His together with the

O \cdots N τ hydrogen bond distances are summarized in Table 2.1. The QM/MM calculation of Y_Z provided a short O \cdots N τ distance of 2.49 Å, which is consistent with the distance in the X-ray structure (2.46 Å)¹⁰ as well as in the previous QM/MM calculation (2.47 Å),¹¹ although the DFT calculation showed a longer distance of 2.82 Å. The relatively long O \cdots N τ distance in Y_D-His as determined by DFT (3.02 Å) and QM/MM (2.79 Å) calculations is also consistent with that in the X-ray structure (2.74 Å).¹⁰ Thus, the hydrogen bonding interactions between Y_{Z(D)} and the coupled His were satisfactorily reproduced in calculations.

The frequency of the N τ -H vibration, which is a significantly localized mode, of the Y_Z \bullet -HisH⁺ model was calculated at 2810 cm⁻¹ in the DFT calculation (Table 2.1). In the QM/MM calculation of Y_Z \bullet -HisH⁺, the symmetric and asymmetric N τ -H/N π -H stretching vibrations were calculated at 2986 and 2748 cm⁻¹, respectively, the latter having a high intensity. These values are

Table 2.1 N τ -H stretching frequencies (cm⁻¹) of the His coupled to Y_Z and Y_D estimated by DFT and QM/MM calculations

	calculation			experimental	
	method	frequency (IR intensity) ^a	rO \cdots N τ (Å) ^b	frequency ^c	rO \cdots N τ (Å) ^b
Y _Z \bullet -HisH ⁺	DFT	2810 (4569)	2.63	~2800	
	QM/MM	2986 (1390)/	2.63		
		2748(3554) ^d			
Y _Z \bullet -HisD ^{+e}	DFT	2106 (2154)	-	~2100	
Y _Z -His	DFT	-	2.82		2.46 ^f
	QM/MM	-	2.49		
Y _Z -HisH ⁺	DFT	3027 (2211)	2.75		
Y _D \bullet -His	DFT	3417 (1141)	2.95		
	QM/MM	3162 (2083)	2.77		
Y _D -His	DFT	3511 (658)	3.02		2.74 ^f
	QM/MM	3250 (1490)	2.79		
4-MeIm (N τ H)	DFT	3601 (58)			
4-MeImH ⁺	DFT	3554 (72)/			
		3546 (281) ^d			

^aIR intensity calculated in kilometers per mole. ^bHydrogen bond distance between the oxygen atom of Tyr and N τ of His. ^cExperimental frequency observed in this study. ^dCoupled symmetric and asymmetric stretching vibrations of N τ -H and N π -H. ^eThe exchangeable protons of N τ -H and N π -H of HisH⁺ are deuterated. ^fValue from the X-ray structure of PSII (PDB entry 3ARC).

Table 2.2 CN stretching frequencies (cm^{-1}) of His coupled to Y_Z estimated by DFT and QM/MM calculations

		protonated		deuterated ^a		
		frequency (¹⁵ N shift) ^b	IR intensity ^c	frequency (¹⁵ N shift) ^b	IR intensity ^c	H/D shift ^d
DFT	Y _Z -His	1121 (-7)	54	1144 (-6)	48	-1
	Y _Z [•] -HisH ⁺	1097 (-5)	3	1136 (-4)	7	16
QM/MM	Y _Z -His	1109 (-4)	94	1149 (-4)	114	3
	Y _Z [•] -HisH ⁺	1086 (-3)	18	1139 (-2)	7	17

^aAll the exchangeable protons are deuterated. ^bAll the nitrogen atoms in His (DFT) and in the QM region (QM/MM) are substituted with ¹⁵N. ^cIR intensity calculated in kilometers per mole. ^dFrequency shift upon deuteration.

significantly lower than the N τ -H frequencies of free 4-MeIm and 4-MeImH⁺ (3601–3546 cm^{-1}), and the IR intensities are much larger than those in the latter free molecules (Table 2.1). The His side chain in Y_Z-His (Figure 2.8B) is deprotonated at N τ , and hence, there is no N τ -H vibration; Y_Z-HisH⁺ (Figure 2.8C) showed a relatively low N τ -H frequency of 3027 cm^{-1} . In all of the Y_Z models ¹⁵N substitution downshifts the N-H frequencies by 9–11 cm^{-1} (not shown in the table). In contrast to Y_Z[•] and Y_Z, Y_D[•]-His and Y_D-His (Figure 2.8D,E) exhibited relatively high N τ -H frequencies (3417–3162 and 3534–3250 cm^{-1} , respectively) in the DFT and QM/MM calculations.

These calculated N τ -H frequencies are consistent with the experimental data (Table 2.1). The presence of a broad positive band around \sim 2800 cm^{-1} in the Y_Z[•]/Y_Z spectrum (Figure 2.5, and 2.6) is in agreement with the strong N τ -H (or coupled N τ -H/N π -H) vibration calculated at 3000–2700 cm^{-1} in Y_Z[•]-HisH⁺ and the absence of the N τ -H vibration in Y_Z-His. The downshift of the broad band to \sim 2100 cm^{-1} in the D₂O measurements (Figure 2.5b, inset) was also reproduced by the frequency of deuterated Y_Z[•]-HisD⁺ at 2106 cm^{-1} in the DFT calculation (Table 2.1), while the ¹⁵N-induced downshift of \sim 10 cm^{-1} (Figure 2.5a) is in agreement with the calculated shift. In addition, the absence of a broad band at pH 5.5 (Figure 2.6Bc) is consistent with the calculated low frequency of N τ -H at \sim 3000 cm^{-1} in Y_Z-HisH⁺, which may cancel the positive band of Y_Z[•]-HisH⁺. Furthermore, the calculated frequency of Y_D[•]-His at 3417–3162 cm^{-1} is in agreement with the observation that the Y_D[•]/Y_D spectrum did not show a positive band in the region lower than 3000 cm^{-1} except for a baseline rise (Figure 2.5c).

Table 2.2 presents the calculated frequencies of the CN stretching vibration of His in the Y_Z-His pair. The frequencies were estimated to be \sim 1100 cm^{-1} , in agreement with the experimental results (Figure 2.4). The HisH⁺ form in Y_Z[•]-HisH⁺ shows a CN frequency lower than that of the neutral N π -H form in Y_Z-His, consistent with the previous calculated and experimental data of free His or 4-MeIm.^{44, 49, 50} The CN frequencies are downshifted by ¹⁵N substitution by 4–7 and 2–5 cm^{-1} in Y_Z-His and Y_Z[•]-HisH⁺, respectively. Upon deuteration, Y_Z-

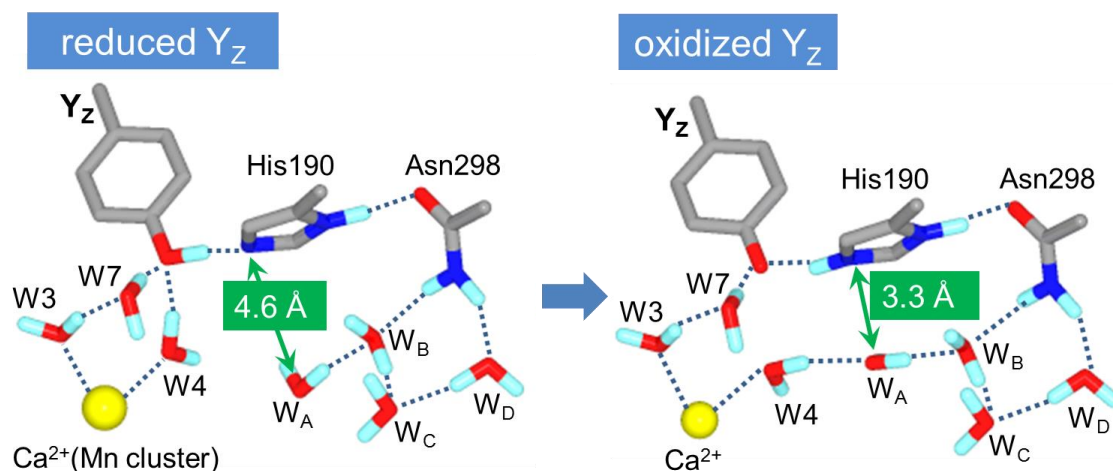


Figure 2.9 Rearrangement of the hydrogen bond network near Y_Z upon its oxidation estimated by QM/MM calculations. Relevant amino acid side chains, water molecules, and the Ca atom were selected from the QM region. In the amino acid side chains, hydrogen atoms other than exchangeable protons have been omitted. The drastic movements of protons and a water molecule are expressed with red circles and red arrows. Upon Y_Z oxidation, the Y_Z proton is shifted to D1-His190, the hydrogen bond of the W4 proton with the Y_Z oxygen is broken and this proton is turned to the W_A side to form a new hydrogen bond, and W_A moves toward D1-His190.

His shows only a minor shift between -1 and 3 cm^{-1} , whereas $Y_Z^\bullet\text{-HisH}^+$ shows a large upshift of $16\text{--}17\text{ cm}^{-1}$, which is in agreement with the previous calculation for free 4-MeIm.⁴⁴ It is notable, however, that the IR intensities of the protonated HisH^+ form in $Y_Z^\bullet\text{-HisH}^+$ are much smaller than those of neutral His in $Y_Z\text{-His}$ by factors of 5–18 in DFT and QM/MM calculations, suggesting that the His bands of the reduced $Y_Z\text{-His}$ state mainly appear in the Y_Z^\bullet/Y_Z spectrum. These calculated results are quite consistent with the experimental spectra in Figure 2.4. The major contribution is a negative band due to the reduced $Y_Z\text{-His}$, which showed a ^{15}N downshift by $\sim 6\text{ cm}^{-1}$ (Figure 2.4a), indicative of the change of the neutral $\text{N}\pi\text{-H}$ form of His to another form upon formation of Y_Z^\bullet . The upshift of $3\text{--}5\text{ cm}^{-1}$ upon deuteration (Figure 2.4c) is also consistent with the minor deuteration effect of the reduced $Y_Z\text{-His}$ (Table 2.2). The CN band of the HisH^+ form in $Y^\bullet\text{-HisH}^+$, which should show a large deuteration shift of $16\text{--}17\text{ cm}^{-1}$, was not identified in the observed FTIR spectra, which is also consistent with the significantly smaller intensity and a slightly smaller ^{15}N shift estimated by calculations. Thus, the FTIR spectra in the His CN region together with DFT and QM/MM calculations support the view that the protonation structure of the His coupled to Y_Z is changed from the neutral $\text{N}\pi\text{-H}$ form to the protonated cation form upon Y_Z oxidation.

The QM/MM calculations for the Y_Z site also exhibited a significant rearrangement of

the hydrogen bond network around Y_Z concomitant with the movements of water molecules upon Y_Z oxidation (Figure 2.9). When Y_Z is oxidized, a proton of Y_Z is released to $N\tau$ of D1-His190, forming a strong hydrogen bond with a neutral Y_Z^\bullet radical. Because the CO bond of the Y_Z^\bullet radical has a double bond character [the CO stretching vibration is significantly upshifted from 1262 to 1513 cm^{-1} (Figure 2.7)], the Y_Z oxygen can accept only two hydrogen bonds. Hence, the hydrogen bond with the W4 proton, which is weaker than that with W7,¹¹ is broken, and this proton turns to the side of another water molecule (designated W_A in Figure 2.9). This rotation of W4 induces the movement of W_A toward D1-His190. The distance between the W_A oxygen and $N\tau$ of D1-His190 is shortened from 4.57 to 3.28 Å upon Y_Z oxidation. A network of water molecules is now formed from W4 to W_D through W_A , W_B , and W_C near D1-Asn298 (Figure 2.9) and is further connected to the hydrogen bond network to the luminal side.¹⁰

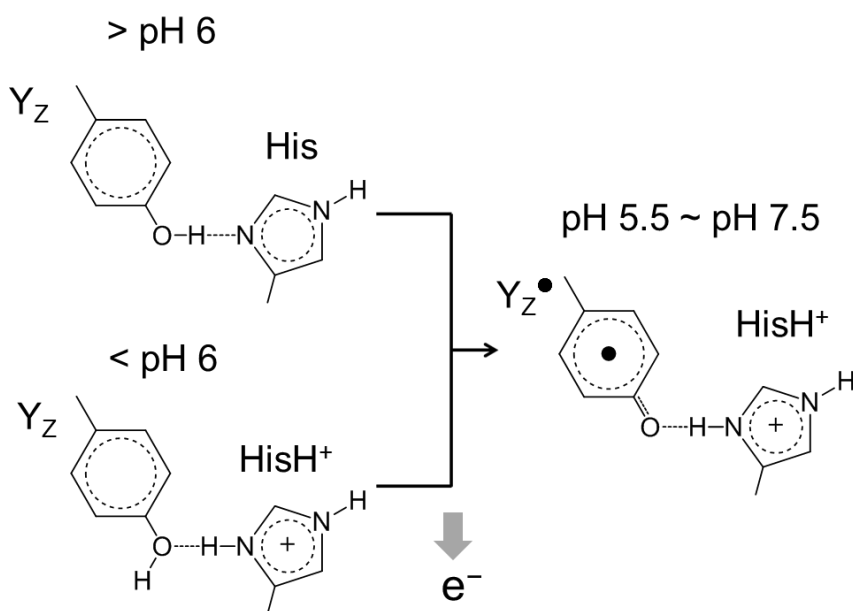


Figure 2.10 Changes in the hydrogen-bonded structures of Y_Z and D1-His190 with pH and photooxidation.

2.4. Discussion

Upon oxidation of Y_Z , a proton is released from the phenolic OH to form a neutral radical Y_Z^\bullet .^{12-15, 55} This FTIR study directly detected this proton that is trapped by the neighboring His residue, D1-His190, as an $N\tau$ -H stretching vibration. The broad positive feature around 2800 cm^{-1} in the Y_Z^\bullet/Y_Z FTIR difference spectrum (Figures 2.2, 2.5, and 2.6) was assigned to this $N\tau$ -H vibration (or the coupled $N\tau$ -H/ $N\pi$ -H vibration) of the protonated HisH⁺ cation. The evidence of this assignment was obtained from isotopic substitutions and quantum chemical calculations.

H/D exchange induced a large downshift from ~ 2800 to ~ 2100 cm^{-1} (Figure 2.5b), indicative of the vibration involving an exchangeable proton. In addition, global ^{15}N substitution showed downshifts of the broad feature and superimposing several small peaks on it (Figure 2.5a), indicating the presence of the NH vibration coupled with other His vibrations by Fermi resonance. The DFT calculation of the $\text{Y}_Z^\bullet\text{-HisH}^+$ model (Figure 2.8a) and the QM/MM calculation taking into account the surrounding amino acids and water molecules provided the $\text{N}\tau\text{-H}$ stretching vibration or the coupled $\text{N}\tau\text{-H}/\text{N}\pi\text{-H}$ vibrations of HisH^+ at $3000\text{--}2700$ cm^{-1} (Table 2.1), reproducing the observed frequency well. The absence of protonated $\text{N}\tau\text{-H}$ in the reduced $\text{Y}_Z\text{-His}$ form (Figure 2.8b) rationalizes the appearance of a positive $\text{N}\tau\text{-H}$ band of HisH^+ in the $\text{Y}_Z^\bullet/\text{Y}_Z$ difference spectrum. In addition, the DFT calculation of deuterated $\text{Y}_Z^\bullet\text{-HisD}^+$ providing the $\text{N}\tau\text{-D}$ frequency of 2106 cm^{-1} (Table 2.1) reproduced a downshift to ~ 2100 cm^{-1} in D_2O (Figure 2.4c, inset). Furthermore, the results of the analysis of the CN stretching vibration of His using ^{15}N substitution and deuteration (Figure 2.4) in combination with DFT and QM/MM calculations (Table 2.2) are consistent with the change in the protonation structure of His from the neutral $\text{N}\pi\text{-H}$ form to the protonated cation form upon Y_Z^\bullet formation.

The pH dependence of the $\text{Y}_Z^\bullet/\text{Y}_Z$ spectrum further supported the assignment given above. The positive feature around ~ 2800 cm^{-1} disappeared at pH 5.5 (Figure 2.6Bc). The DFT calculation of the reduced $\text{Y}_Z\text{-HisH}^+$ (Figure 2.8c), which is thought to be formed at lower pH values (Figure 2.10),^{13, 15, 21, 55} showed a relatively low $\text{N}\tau\text{-H}$ frequency of 3027 cm^{-1} (Table 2.1), comparable to the calculated frequencies at $3000\text{--}2700$ cm^{-1} of $\text{Y}_Z^\bullet\text{-HisH}^+$. Thus, the absence of the band is explained by cancellation of the $\text{N}\tau\text{-H}$ band in the difference spectrum between $\text{Y}_Z\text{-HisH}^+$ and $\text{Y}_Z^\bullet\text{-HisH}^+$. The change in the hydrogen-bonded structure of reduced Y_Z at a low pH (Figure 2.10A,B) was confirmed by the downshift of the pure νCO band of Y_Z , which was decoupled from the δCOH vibration by measurement in D_2O , from 1263 cm^{-1} at pD 7.5 to 1259 cm^{-1} at pD 5.5 (Figure 2.7C). In contrast, the νCO frequency of oxidized Y_Z^\bullet was virtually unchanged throughout the pH or pD range of 5.5–7.5 (Figures 2.6A and 2.7B), consistent with the view that Y_Z^\bullet has a structure identical to that of $\text{Y}_Z^\bullet\text{-HisH}^+$ over this pH or pD range (Figure 2.10C). If the structural models in Figure 2.10 are correct, a proton should be released from the $\text{Y}_Z\text{-His}$ moiety at pH 5.5. Indeed, at this pH, negative bands at 1405 and 1572 cm^{-1} , which can be interpreted as arising from the symmetric and asymmetric carboxylate stretching vibrations, respectively, and a positive feature around 1720 cm^{-1} that can be attributed to the $\text{C}=\text{O}$ stretches of protonated COOH groups were observed (Figure 2.6A, spectrum c), suggesting that some specific or nonspecific carboxylate groups in PSII proteins were protonated by the proton released from Y_Z . Our observation indicates that the pK_a of D1-His190 coupled to the reduced Y_Z is around 6 in our core complexes from *T. elongatus*. Although this value is lower than the general pK_a estimation (~ 7) in Mn-depleted PSII preparations in previous reports^{13, 15, 55} it has also been

shown that the pK_a of this His is significantly dependent on the PSII preparations and the content of metal ions.^{21, 55}

In contrast to Y_Z^\bullet , Y_D^\bullet did not show a broad band at $\sim 2800\text{ cm}^{-1}$ at pH 6.5 (Figure 2.5c) or even at pH 10.5 (data not shown). Indeed, the DFT and QM/MM calculations of the Y_D^\bullet -His (Figure 2.8d) and Y_D -His (Figure 2.8e) models, in which His has a neutral N τ -H form, provided the N τ -H frequencies at much higher frequencies of $3550\text{--}3150\text{ cm}^{-1}$ (Table 2.1), the region of strong water bands. Thus, these calculations also explain well the Y_D^\bullet/Y_D FTIR spectrum, supporting the assignment of the N-H band at $\sim 2800\text{ cm}^{-1}$ in the Y_Z^\bullet/Y_Z spectrum described above.

All of the FTIR data provided above and the results of DFT and QM/MM calculations indicate that D1-His190 coupled with the oxidized Y_Z^\bullet radical has a protonated cation form. The low N-H frequency of $\sim 2800\text{ cm}^{-1}$ reflects the presence of a strong hydrogen bond between Y_Z^\bullet and HisH⁺. Because the similar hydrogen bond with a neutral His in the Y_D^\bullet -His model showed a higher N τ -H frequency ($3417\text{--}3162\text{ cm}^{-1}$) and a longer O \cdots N τ distance ($2.77\text{--}2.96\text{ \AA}$ in comparison with 2.63 \AA in Y_Z^\bullet -HisH⁺) (Table 2.1), this strong hydrogen bonding interaction of Y_Z^\bullet -HisH⁺ most probably originates from the so-called charge-assisted hydrogen bond.⁵⁶⁻⁵⁸ The stronger hydrogen bond in Y_Z^\bullet compared with that in Y_D^\bullet has also been pointed out in the νCO frequency in Y_Z^\bullet (1514 cm^{-1}) being higher than that in Y_D^\bullet (1504 cm^{-1}) (Figure 2.3).³⁴ Theoretical calculations have shown that a stronger hydrogen bond upshifts the νCO frequency of the Tyr \bullet radical.^{59, 60} The retention of a positive charge on D1-His190 after Y_Z oxidation is consistent with the previous reports of the electrochromic shift of Chl absorption upon Y_Z oxidation,¹⁸ the low g_x value in the highfield EPR spectrum,¹⁶ the absence of proton release,²¹ and the Y_Z oxidation capability at ultralow temperatures.¹⁵

The N-H band around $\sim 2800\text{ cm}^{-1}$ in the Y_Z^\bullet/Y_Z spectrum has a very broad width (Figures 2.2 and 2.5a). This type of broad feature in IR spectra has been attributed to a strong hydrogen bond with large proton polarizability, and the crucial role of such a polarizable proton in proton transfer in proteins has been proposed.⁶¹⁻⁶⁵ The broad N-H band of Y_Z^\bullet indicates that the proton in the strong hydrogen bond between Y_Z^\bullet and HisH⁺ is highly polarizable; i.e., it readily moves in response to the change in the electrostatic field in the environment. The presence of a polarizable proton in the hydrogen bond of Y_Z^\bullet is also consistent with the slightly broader νCO band at 1514 cm^{-1} in comparison with that at 1504 cm^{-1} in Y_D^\bullet (Figure 2.3), the observation previously mentioned by Berthomieu et al.³⁴

We used the Mn-depleted PSII core complexes for the measurement of Y_Z^\bullet/Y_Z FTIR difference spectra in this study. The property of Y_Z is predicted to be changed by Mn depletion.¹⁴⁵⁵ In particular, the structure of the water cluster near the Ca atom and Y_Z (Figure 2.1) may be broken upon removal of the Mn cluster. However, the QM/MM calculation including water

molecules and amino acid residues surrounding Y_Z as the QM region provided an N-H frequency (2748 cm^{-1}) similar to that determined by the DFT calculation (2810 cm^{-1}) without these groups (Table 2.1). Experimentally, the high-field EPR study using a PSII crystal also showed that the orientation of Y_Z does not change after Mn depletion and thus concluded that the pattern of hydrogen bonding around Y_Z^\bullet is not influenced drastically by removal of the Mn cluster.¹⁶ Also, it was shown that at alkaline pH values, Mn-depleted PSII is significantly kinetically similar to intact PSII, indicative of the same reaction mechanism of PCET of Y_Z .¹³ Therefore, the conclusion about the hydrogen bonding interaction between Y_Z^\bullet and D1-His190 obtained using Mn-depleted PSII should basically hold also in Mn-intact PSII.

The role of a positive charge on D1-His190 next to the Y_Z^\bullet radical in the water oxidation mechanism has been proposed to be driving the release of the proton from substrate water especially in the S_2 and S_3 states, which has the surplus of a positive charge on the Mn cluster.^{15, 29, 31, 66} On the other hand, retention of the proton at $N\tau$ of D1-His190 without proton release even from $N\pi$ -H is at odds with the previous proposal of the “hydrogen abstraction model”,¹⁷ in which a proton is first released from the Y_Z site to the lumen and then the Y_Z^\bullet radical abstracts a hydrogen atom from substrate water. The arguments against this model have already been made by many authors from experimental^{15, 16, 18, 19} and theoretical⁶⁷ viewpoints. The data in this FTIR study add further evidence that opposes this model. There is another possibility, however, that Y_Z is directly related to proton transfer without releasing a proton upon its oxidation: the Y_Z -His site is simply involved in a proton transfer pathway when a proton is released from substrate water in some S-state transitions.

From the information of the X-ray structure of PSII,⁸⁻¹⁰ possible proton pathways have been predicted.^{10, 22-24, 68} The most probable pathway is the one that starts from D1-Asp61 and passes through Cl-1.^{32, 33, 68-75} The hydrogen bond network connecting Y_Z and the lumen was also proposed as a candidate of the proton pathway.^{10, 24} There is a water cluster between the Mn cluster and Y_Z (Figure 2.1A), and thus, the protons of the water ligands, W4, W3, and W2 (and possibly O5, if this is a hydroxide¹⁰), are readily transferred to the Y_Z oxygen by the Grotthuss mechanism^{76, 77} (Figure 2.11). The “gate” of this proton transfer pathway is the Y_Z -His site that connects the water cluster with the water channel near D1-Asn298 leading to the lumen. The QM/MM calculations showed that upon Y_Z oxidation and concomitant release of a proton to D1-His190, the hydrogen bond between W4 and Y_Z is broken and the W4 proton forms a new hydrogen bond with another water, WA (Figure 2.9). By this hydrogen bond formation, WA significantly moves toward D1-His190 and the distance between $N\tau$ of His190 and the WA oxygen is shortened from 4.57 to 3.28 Å. Because the proton of $N\tau$ -H of D1-His190 is highly polarizable (see above), it is movable responding to the change in the charge distribution in the Mn cluster and the fluctuation of the protein and water environments, and hence, there is a chance to hop to WA, the nearby

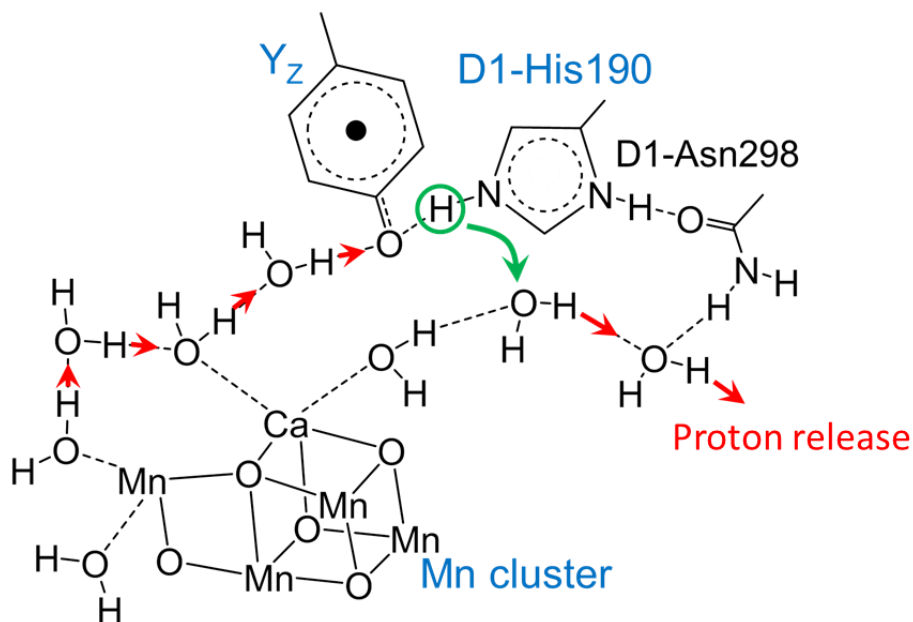


Figure 2.11 Proposed mechanism for the proton release from substrate water on the Mn cluster via the Y_Z^\bullet -HisH⁺ moiety as a gate. The high-polarizability proton detected in this study is marked with a red circle. Hopping of this proton to W_A , which moved toward D1-His190 upon Y_Z oxidation, triggers immediate transfer of a proton from substrate water to Y_Z through the water cluster by the Grotthuss mechanism (red arrows).

proton acceptor. This proton hopping is the rate-limiting step and triggers the shift of the equilibrium of proton transfer between the water ligands and Y_Z^\bullet to the Y_Z^\bullet side, while the proton on W_A is also transferred to the hydrogen bond network near D1-Asn298 via water molecules (Figures 2.9 and 2.11). Thus, eventually a proton is transferred from substrate water to the lumen. An alternative possibility could be hopping of a proton from W_7 to W_4 (the distance between their oxygen atoms is 3.84 Å in the Y_Z^\bullet state), which is now connected to the hydrogen bond network to the lumen through W_A - W_D (Figures 2.9 and 2.11). The key event in this novel proton transfer mechanism is the movement of a water molecule for rearrangement of the hydrogen bond network. The significance of such mobile water in proton pathways has been suggested previously.^{24, 33, 65}

This type of proton transfer can take place before the transfer of an electron from the Mn cluster to Y_Z^\bullet . Such a protonfirst PCET reaction has been proposed to occur at the S_2 and S_3 states, which have an excess positive charge on the Mn cluster, to decrease the redox potentials before electron transfer.^{29, 31, 78, 79} Which proton pathway is preferentially used in each S-state transition may depend on the structural relationship of the proton-releasing substrate with the hydrogen bond network around the Mn cluster. The $S_3 \rightarrow S_0$ transition seems to use the pathway via D1-Asp61 and Cl-1,^{32, 33, 68-75} because mutations at D1-Asp61⁷³⁻⁷⁵ and D2-Lys317,^{71, 72} which

is a ligand to Cl-1, retard the rate of this transition or affects the efficiency. In contrast, in the $S_2 \rightarrow S_3$ transition, another pathway near Y_Z was proposed to be active.²⁹ It is suggested that the electrostatic repulsion between the positive charges on D1-His190 and the Mn cluster in the S_2 state promotes the proton transfer cascade starting from the release of the polarizable proton in Y_Z^\bullet -HisH⁺. In this case, the protons from W4, W3, and W2 (and possibly O5) can be released to the luminal side using the proton transfer mechanism mentioned above (Figure 2.11). The proton transfer via Y_Z^\bullet -HisH⁺ may also take place in concerted PCET. This proton transfer mechanism looks similar to the previous hydrogen abstraction model.¹⁷ The basic difference, however, is that in the mechanism proposed here, the triggering reaction of the transfer of a proton from HisH⁺ determines the rate of the whole PCET process and the stable formation of deprotonated Y_Z^\bullet -His is not required.

Proton rocking along the hydrogen bond between Y_Z and D1-His190 without further proton release is the most effective way to decrease the energy barrier of the redox reactions of Y_Z . The strong hydrogen bond in the Y_Z -His pair in the oxidized form as shown in this study as well as in the reduced form as theoretically revealed by Saito et al.¹¹ particularly contributes to the increase in the rates of Y_Z reactions. In contrast, the absence of proton rocking between Y_D and D2-His189 was also confirmed by the absence of a broad feature at a frequency of $<3000\text{ cm}^{-1}$ (Figure 2.5c), indicative of no formation of the Y_D -HisH⁺ form. This is because D2-His189 has a neutral $N\tau$ -H form by accepting a hydrogen bond at the $N\pi$ site from the guanidinium cation of D2-Arg294 and hence cannot accept a hydrogen bond at $N\tau$ from the Y_D OH (Figure 2.8e). Thus, Y_D releases a proton along a longer proton pathway in the protein, as recently indicated by the QM/MM calculations.²⁸ Such a difference in the proton release mechanism provides a major cause for the kinetic difference between Y_Z and Y_D ^{12, 14, 15} and hence their roles as the main and peripheral electron donor, respectively, to P680⁺.

References

- [1] Debus, R. J. (1992) The manganese and calcium ions of photosynthetic oxygen evolution, *Biochim. Biophys. Acta* 1102, 269-352.
- [2] Hillier, W., and Messinger, J. (2005) Mechanism of photosynthetic oxygen production, In *Photosystem II: The Light-Driven Water: Plastoquinone Oxidoreductase* (Wydrzynski, T. J., and Satoh, K., Eds.), pp 567-608, Springer, Dordrecht, The Netherlands.
- [3] McEvoy, J. P., and Brudvig, G. W. (2006) Water-splitting chemistry of photosystem II, *Chem. Rev.* 106, 4455-4483.
- [4] Messinger, J., Noguchi, T., and Yano, J. (2011) Photosynthetic O₂ evolution, In *Molecular*

- solar fuels* (Wydrzynski, T. J., and Hillier, W., Eds.), pp 163-207, Royal Society of Chemistry, Cambridge, U.K.
- [5] Grundmeier, A., and Dau, H. (2012) Structural models of the manganese complex of photosystem II and mechanistic implications, *Biochim. Biophys. Acta 1817*, 88-105.
- [6] Renger, G. (2012) Photosynthetic water splitting: Apparatus and mechanism, In *Photosynthesis: Plastid Biology, Energy Conversion and Carbon Assimilation* (Eaton-Rye, J. J., Tripathy, B. C., and Sharkey, T. D., Eds.), pp 359-414, Springer, Dordrecht, The Netherlands.
- [7] Vinyard, D. J., Ananyev, G. M., and Dismukes, G. C. (2013) Photosystem II: the reaction center of oxygenic photosynthesis, *Annu. Rev. Biochem.* 82, 577-606.
- [8] Ferreira, K. N., Iverson, T. M., Maghlaoui, K., Barber, J., and Iwata, S. (2004) Architecture of the photosynthetic oxygen-evolving center, *Science* 303, 1831-1838.
- [9] Guskov, A., Kern, J., Gabdulkhakov, A., Broser, M., Zouni, A., and Saenger, W. (2009) Cyanobacterial photosystem II at 2.9 Å resolution and the role of quinones, lipids, channels and chloride, *Nat. Struct. Mol. Biol.* 16, 334-342.
- [10] Umena, Y., Kawakami, K., Shen, J. R., and Kamiya, N. (2011) Crystal structure of oxygen-evolving photosystem II at a resolution of 1.9 Å, *Nature* 473, 55-60.
- [11] Saito, K., Shen, J. R., Ishida, T., and Ishikita, H. (2011) Short hydrogen bond between redox-active tyrosine Y_Z and D1-His190 in the photosystem II crystal structure, *Biochemistry* 50, 9836-9844.
- [12] Diner, B. A., and Britt, R. D. (2005) The redox-active tyrosines Y_Z and Y_D, In *Photosystem II: The Light-Driven Water: Plastoquinone Oxidoreductase* (Wydrzynski, T. J., and Satoh, K., Eds.), pp 207-233, Springer, Dordrecht, The Netherlands.
- [13] Rappaport, F., Boussac, A., Force, D. A., Peloquin, J., Brynda, M., Sugiura, M., Un, S., Britt, R. D., and Diner, B. A. (2009) Probing the coupling between proton and electron transfer in photosystem II core complexes containing a 3-fluorotyrosine, *J. Am. Chem. Soc.* 131, 4425-4433.
- [14] Renger, G. (2012) Mechanism of light induced water splitting in Photosystem II of oxygen evolving photosynthetic organisms, *Biochim. Biophys. Acta 1817*, 1164-1176.
- [15] Styring, S., Sjöholm, J., and Mamedov, F. (2012) Two tyrosines that changed the world: Interfacing the oxidizing power of photochemistry to water splitting in photosystem II, *Biochim. Biophys. Acta 1817*, 76-87.
- [16] Matsuoka, H., Shen, J. R., Kawamori, A., Nishiyama, K., Ohba, Y., and Yamauchi, S. (2011) Proton-coupled electron-transfer processes in photosystem II probed by highly resolved g-anisotropy of redox-active tyrosine Y_Z, *J. Am. Chem. Soc.* 133, 4655-4660.
- [17] Hoganson, C. W., and Babcock, G. T. (1997) A metalloradical mechanism for the generation

- of oxygen from water in photosynthesis, *Science* 277, 1953-1956.
- [18] Rappaport, F., and Lavergne, J. (2001) Coupling of electron and proton transfer in the photosynthetic water oxidase, *Biochim. Biophys. Acta* 1503, 246-259.
- [19] Junge, W., Haumann, M., Ahlbrink, R., Mulkidjanian, A., and Clausen, J. (2002) Electrostatics and proton transfer in photosynthetic water oxidation, *Philos. Trans. R. Soc., B* 357, 1407-1417.
- [20] Rappaport, F., and Lavergne, J. (1997) Charge recombination and proton transfer in manganese-depleted photosystem II, *Biochemistry* 36, 15294-15302.
- [21] Ahlbrink, R., Haumann, M., Cherepanov, D., Bogershausen, O., Mulkidjanian, A., and Junge, W. (1998) Function of tyrosine Z in water oxidation by photosystem II: Electrostatical promotor instead of hydrogen abstractor, *Biochemistry* 37, 1131-1142.
- [22] Ho, F. M., and Styring, S. (2008) Access channels and methanol binding site to the CaMn₄ cluster in Photosystem II based on solvent accessibility simulations, with implications for substrate water access, *Biochim. Biophys. Acta* 1777, 140-153.
- [23] Vassiliev, S., Comte, P., Mahboob, A., and Bruce, D. (2010) Tracking the flow of water through photosystem II using molecular dynamics and streamline tracing, *Biochemistry* 49, 1873-1881.
- [24] Ogata, K., Yuki, T., Hatakeyama, M., Uchida, W., and Nakamura, S. (2013) All-atom molecular dynamics simulation of photosystem II embedded in thylakoid membrane, *J. Am. Chem. Soc.* 135, 15670-15673.
- [25] Boussac, A., and Etienne, A. L. (1984) Midpoint potential of signal-II (slow) in Tris-washed photosystem-II particles, *Biochim. Biophys. Acta* 766, 576-581.
- [26] Vass, I., and Styring, S. (1991) pH-Dependent charge equilibria between tyrosine-D and the S states in photosystem II. Estimation of relative midpoint redox potentials, *Biochemistry* 30, 830-839.
- [27] Metz, J. G., Nixon, P. J., Rogner, M., Brudvig, G. W., and Diner, B. A. (1989) Directed alteration of the D1 polypeptide of photosystem II: Evidence that tyrosine-161 is the redox component, Z, connecting the oxygen-evolving complex to the primary electron-donor, P680, *Biochemistry* 28, 6960-6969.
- [28] Saito, K., Rutherford, A. W., and Ishikita, H. (2013) Mechanism of tyrosine D oxidation in Photosystem II, *Proc. Natl. Acad. Sci. U.S.A.* 110, 7690-7695.
- [29] Klauss, A., Haumann, M., and Dau, H. (2012) Alternating electron and proton transfer steps in photosynthetic water oxidation, *Proc. Natl. Acad. Sci. U.S.A.* 109, 16035-16040.
- [30] Klauss, A., Sikora, T., Suss, B., and Dau, H. (2012) Fast structural changes (200-900 ns) may prepare the photosynthetic manganese complex for oxidation by the adjacent tyrosine radical, *Biochim. Biophys. Acta* 1817, 1196-1207.

- [31] Rappaport, F., Blanchard-Desce, M., and Lavergne, J. (1994) Kinetics of electron transfer and electrochromic change during the redox transitions of the photosynthetic oxygen-evolving complex, *Biochim. Biophys. Acta* 1184, 178-192.
- [32] Siegbahn, P. E. M. (2012) Mechanisms for proton release during water oxidation in the S₂ to S₃ and S₃ to S₄ transitions in photosystem II, *PCCP* 14, 4849-4856.
- [33] Linke, K., and Ho, F. M. (2014) Water in Photosystem II: Structural, functional and mechanistic considerations, *Biochim. Biophys. Acta* 1837, 14-32.
- [34] Berthomieu, C., Hienerwadel, R., Boussac, A., Breton, J., and Diner, B. A. (1998) Hydrogen bonding of redox-active tyrosine Z of photosystem II probed by FTIR difference spectroscopy, *Biochemistry* 37, 10547-10554.
- [35] Stanier, R. Y., Kunisawa, R., Mandel, M., and Cohen-Bazire, G. (1971) Purification and properties of unicellular blue-green algae (order Chroococcales), *Bacteriol. Rev.* 35, 171-205.
- [36] Iwai, M., Suzuki, T., Kamiyama, A., Sakurai, I., Dohmae, N., Inoue, Y., and Ikeuchi, M. (2010) The PsbK subunit is required for the stable assembly and stability of other small subunits in the PSII complex in the thermophilic cyanobacterium *Thermosynechococcus elongatus* BP-1, *Plant Cell Physiol.* 51, 554-560.
- [37] Boussac, A., Rappaport, F., Carrier, P., Verbavatz, J. M., Gobin, R., Kirilovsky, D., Rutherford, A. W., and Sugiura, M. (2004) Biosynthetic Ca²⁺/Sr²⁺ exchange in the photosystem II oxygen-evolving enzyme of *Thermosynechococcus elongatus*, *J. Biol. Chem.* 279, 22809-22819.
- [38] Takahashi, R., Sugiura, M., and Noguchi, T. (2007) Water molecules coupled to the redox-active tyrosine Y_D in photosystem II as detected by FTIR spectroscopy, *Biochemistry* 46, 14245-14249.
- [39] Frisch, M. J., Trucks, G. W., Schlegel, H. B., Scuseria, G. E., Robb, M. A., Cheeseman, J. R., Scalmani, G., Barone, V., Mennucci, B., Petersson, G. A., Nakatsuji, H., Caricato, M., Li, X., Hratchian, H. P., Izmaylov, A. F., Bloino, J., Zheng, G., Sonnenberg, J. L., Hada, M., Ehara, M., Toyota, K., Fukuda, R., Hasegawa, J., Ishida, M., Nakajima, T., Honda, Y., Kitao, O., Nakai, H., Vreven, T., Montgomery, J. A., Jr., Peralta, J. E., Ogliaro, F., Bearpark, M., Heyd, J. J., Brothers, E., Kudin, K. N., Staroverov, V. N., Kobayashi, R., Normand, J., Raghavachari, K., Rendell, A., Burant, J. C., Iyengar, S. S., Tomasi, J., Cossi, M., Rega, N., Millam, J. M., Klene, M., Knox, J. E., Cross, J. B., Bakken, V., Adamo, C., Jaramillo, J., Gomperts, R., Stratmann, R. E., Yazyev, O., Austin, A. J., Cammi, R., Pomelli, C., Ochterski, J. W., Martin, R. L., Morokuma, K., Zakrzewski, V. G., Voth, G. A., Salvador, P., Dannenberg, J. J., Dapprich, S., Daniels, A. D., Farkas, O., Foresman, J. B., Ortiz, J. V., Cioslowski, J., and Fox, D. J. (2009) *Gaussian 09*, revision C.01, *Gaussian Inc., Wallingford CT*.
- [40] Lee, C. T., Yang, W. T., and Parr, R. G. (1988) Development of the Colle-Salvetti correlation-

- energy formula into a functional of the electron density, *Phys. Rev. B* 37, 785-789.
- [41] Becke, A. D. (1993) Density-functional thermochemistry. III. The role of exact exchange, *J. Chem. Phys.* 98, 5648-5652.
- [42] Vreven, T., Byun, K. S., Komaromi, I., Dapprich, S., Montgomery, J. A., Morokuma, K., and Frisch, M. J. (2006) Combining quantum mechanics methods with molecular mechanics methods in ONIOM, *J. Chem. Theory Comput.* 2, 815-826.
- [43] Luber, S., Rivalta, I., Umena, Y., Kawakami, K., Shen, J. R., Kamiya, N., Brudvig, G. W., and Batista, V. S. (2011) S₁-state model of the O₂-evolving complex of photosystem II, *Biochemistry* 50, 6308-6311.
- [44] Hasegawa, K., Ono, T., and Noguchi, T. (2000) Vibrational spectra and ab initio DFT calculations of 4-methylimidazole and its different protonation forms: Infrared and Raman markers of the protonation state of a histidine side chain, *J. Phys. Chem. B* 104, 4253-4265.
- [45] Berthomieu, C., and Hienerwadel, R. (2005) Vibrational spectroscopy to study the properties of redox-active tyrosines in photosystem II and other proteins, *Biochim. Biophys. Acta* 1707, 51-66.
- [46] Hienerwadel, R., Boussac, A., Breton, J., Diner, B. A., and Berthomieu, C. (1997) Fourier transform infrared difference spectroscopy of photosystem II tyrosine D using site-directed mutagenesis and specific isotope labeling, *Biochemistry* 36, 14712-14723.
- [47] Noguchi, T., Inoue, Y., and Tang, X. S. (1997) Structural coupling between the oxygen-evolving Mn cluster and a tyrosine residue in photosystem II as revealed by Fourier transform infrared spectroscopy, *Biochemistry* 36, 14705-14711.
- [48] Takahashi, R., and Noguchi, T. (2007) Criteria for determining the hydrogen-bond structures of a tyrosine side chain by Fourier transform infrared spectroscopy: Density functional theory analyses of model hydrogen-bonded complexes of *p*-cresol, *J. Phys. Chem. B* 111, 13833-13844.
- [49] Onidas, D., Stachnik, J. M., Brucker, S., Kratzig, S., and Gerwert, K. (2010) Histidine is involved in coupling proton uptake to electron transfer in photosynthetic proteins, *Eur. J. Cell Biol.* 89, 983-989.
- [50] Noguchi, T., Inoue, Y., and Tang, X. S. (1999) Structure of a histidine ligand in the photosynthetic oxygen-evolving complex as studied by light-induced Fourier transform infrared difference spectroscopy, *Biochemistry* 38, 10187-10195.
- [51] Breton, J., and Navedryk, E. (1998) Proton uptake upon quinone reduction in bacterial reaction centers: IR signature and possible participation of a highly polarizable hydrogen bond network, *Photosynth. Res.* 55, 301-307.
- [52] Noguchi, T., Inoue, Y., and Tang, X. S. (1999) Hydrogen bonding interaction between the primary quinone acceptor Q_A and a histidine side chain in photosystem II as revealed by

- Fourier transform infrared spectroscopy, *Biochemistry* 38, 399-403.
- [53] Suzuki, H., Nagasaka, M., Sugiura, M., and Noguchi, T. (2005) Fourier transform infrared spectrum of the secondary quinone electron acceptor Q_B in photosystem II, *Biochemistry* 44, 11323-11328.
- [54] Iwata, T., Paddock, M. L., Okamura, M. Y., and Kandori, H. (2009) Identification of FTIR bands due to internal water molecules around the quinone binding sites in the reaction center from *Rhodobacter sphaeroides*, *Biochemistry* 48, 1220-1229.
- [55] Hays, A. M. A., Vassiliev, I. R., Golbeck, J. H., and Debus, R. J. (1999) Role of D1-His190 in the proton-coupled oxidation of tyrosine Y_Z in manganese-depleted photosystem II, *Biochemistry* 38, 11851-11865.
- [56] Meot-Ner, M. (2005) The ionic hydrogen bond, *Chem. Rev.* 105, 213-284.
- [57] Gilli, P., Pretto, L., Bertolasi, V., and Gilli, G. (2009) Predicting hydrogen-bond strengths from acid-base molecular properties. The pK_a slide rule: Toward the solution of a long-lasting problem, *Acc. Chem. Res.* 42, 33-44.
- [58] Freindorf, M., Kraka, E., and Cremer, D. (2012) A comprehensive analysis of hydrogen bond interactions based on local vibrational modes, *Int. J. Quantum Chem.* 112, 3174-3187.
- [59] O'Malley, P. J. (2000) Density functional studies of phenoxy-Na⁺ ion complexes: implications for tyrosyl free radical interactions in vitro, *Chem. Phys. Lett.* 325, 69-72.
- [60] O'Malley, P. J. (2002) Density functional calculations modelling tyrosine oxidation in oxygenic photosynthetic electron transfer, *Biochim. Biophys. Acta* 1553, 212-217.
- [61] Janosche, R., Weideman, E. G., Pfeiffer, H., and Zundel, G. (1972) Extremely high polarizability of hydrogen-bonds, *J. Am. Chem. Soc.* 94, 2387-2396.
- [62] Zundel, G. (1988) Proton transfer in and proton polarizability of hydrogen bonds: IR and theoretical studies regarding mechanisms in biological systems, *J. Mol. Struct.* 177, 43-68.
- [63] Zundel, G. (2000) Hydrogen bonds with large proton polarizability and proton transfer processes in electrochemistry and biology, *Adv. Chem. Phys.* 111, 1-217.
- [64] Wang, J. P., and El-Sayed, M. A. (2001) Time-resolved Fourier transform infrared spectroscopy of the polarizable proton continua and the proton pump mechanism of bacteriorhodopsin, *Biophys. J.* 80, 961-971.
- [65] Freier, E., Wolf, S., and Gerwert, K. (2011) Proton transfer via a transient linear water-molecule chain in a membrane protein, *Proc. Natl. Acad. Sci. U.S.A.* 108, 11435-11439.
- [66] Nugent, J. H. A., Ball, R. J., and Evans, M. C. W. (2004) Photosynthetic water oxidation: the role of tyrosine radicals, *Biochim. Biophys. Acta* 1655, 217-221.
- [67] Siegbahn, P. E. M., and Blomberg, M. R. A. (2010) Quantum chemical studies of proton-coupled electron transfer in metalloenzymes, *Chem. Rev.* 110, 7040-7061.
- [68] Ishikita, H., Saenger, W., Loll, B., Biesiadka, J., and Knapp, E. W. (2006) Energetics of a

- possible proton exit pathway for water oxidation in photosystem II, *Biochemistry* 45, 2063-2071.
- [69] Bao, H., Dilbeck, P. L., and Burnap, R. L. (2013) Proton transport facilitating water-oxidation: the role of second sphere ligands surrounding the catalytic metal cluster, *Photosynth. Res.* 116, 215-229.
- [70] Pokhrel, R., McConnell, I. L., and Brudvig, G. W. (2011) Chloride regulation of enzyme turnover: Application to the role of chloride in photosystem II., *Biochemistry* 50, 2725-2734.
- [71] Suzuki, H., Yu, J. F., Kobayashi, T., Nakanishi, H., Nixon, P. J., and Noguchi, T. (2013) Functional roles of D2-Lys317 and the interacting chloride ion in the water oxidation reaction of photosystem II as revealed by Fourier transform infrared analysis, *Biochemistry* 52, 4748-4757.
- [72] Pokhrel, R., Service, R. J., Debus, R. J., and Brudvig, G. W. (2013) Mutation of lysine 317 in the D2 subunit of photosystem II alters chloride binding and proton transport, *Biochemistry* 52, 4758-4773.
- [73] Clausen, J., Debus, R. J., and Junge, W. (2004) Time-resolved oxygen production by PSII: chasing chemical intermediates, *Biochim. Biophys. Acta* 1655, 184-194.
- [74] Hundelt, M., Hays, A. M. A., Debus, R. J., and Junge, W. (1998) Oxygenic photosystem II: The mutation D1-D61N in *Synechocystis* sp. PCC 6803 retards S-state transitions without affecting electron transfer from Y_Z to $P680^+$, *Biochemistry* 37, 14450-14456.
- [75] Dilbeck, P. L., Hwang, H. J., Zaharieva, I., Gerencser, L., Dau, H., and Burnap, R. L. (2012) The D1-D61N mutation in *Synechocystis* sp. PCC 6803 allows the observation of pH-sensitive intermediates in the formation and release of O_2 from photosystem II, *Biochemistry* 51, 1079-1091.
- [76] de Grotthuss, C. J. T. (1806) Sur la décomposition de l'eau et des corps qu'elle tient en dissolution à l'aide de l'électricité galvanique, *Ann. Chim.* 58, 54-74.
- [77] Cukierman, S. (2006) Et tu, Grotthuss! and other unfinished stories, *Biochim. Biophys. Acta* 1757, 876-885.
- [78] Noguchi, T., Suzuki, H., Tsuno, M., Sugiura, M., and Kato, C. (2012) Time-resolved infrared detection of the proton and protein dynamics during photosynthetic oxygen evolution, *Biochemistry* 51, 3205-3214.
- [79] Haumann, M., Liebisch, P., Muller, C., Barra, M., Grabolle, M., and Dau, H. (2005) Photosynthetic O_2 formation tracked by time-resolved X-ray experiments, *Science* 310, 1019-1021.

Proton release reaction of tyrosine D in photosystem II

3.1. Introduction

The redox-active tyrosine Y_Z (D1-Tyr161) donates an electron to $P680^+$ at 30 ns to 50 μs ^{1, 2} which then abstracts an electron from the Mn cluster, the core part of the water-oxidizing center (WOC), at the rates of 30 μs to 2 ms, depending on different intermediates, called S_i states ($i = 1-4$), of the WOC.³⁻⁶ There is another redox-active tyrosine, Y_D (D2-Tyr160), which is located symmetrically to Y_Z , on the electron donor side of PSII.^{1, 7} In contrast to Y_Z , however, Y_D functions as a peripheral electron donor to $P680^+$ and has only a weak interaction with the Mn cluster.^{8, 9} The rate of electron transfer from Y_D to $P680^+$ is in the millisecond regime,^{10, 11} which is much slower than that from Y_Z . In addition, the oxidized Y_D is significantly stable at room temperature and rereduced by the S_0 state of WOC in hours^{8, 9} Although the exact physiological role of Y_D remains unclear, it has been suggested that Y_D serves functions related to maintaining the WOC in stable higher valence states by oxidation of the overreduced forms, affecting the energetics of $P680^+$, accelerating the photoactivation process of WOC, and protecting against photoinhibition.¹²⁻¹⁴ The remaining question concerns the mechanistic cause of the expression of this significant functional difference between Y_Z and Y_D despite their symmetrical locations in PSII.^{1, 7, 10, 15}

The X-ray crystallographic structures of PSII complexes showed that the $N\tau$ nitrogen of the imidazole group of D1-His190 and D2-His189 is located in close vicinity to the phenolic oxygen of Y_Z and Y_D , respectively (Figure 2.1),¹⁶⁻¹⁹ and it most probably forms a hydrogen bond.^{12, 15, 20-29} Thus, it has been thought that these His side chains function as proton acceptors of Y_Z and Y_D . Indeed, there are several lines of experimental and theoretical evidence that a proton moves back and forth between Y_Z and D1-His190 through a strong hydrogen bond upon oxidation and rereduction.^{7, 26, 27, 29-33} This proton rocking mechanism explains the rapid proton-coupled electron transfer reactions of Y_Z . In the previous chapter, we directly detected the proton transferred from Y_Z to D1-His190 as its $N\tau$ -H stretching vibration at $\sim 2800\text{ cm}^{-1}$ using light-induced Fourier transform infrared (FTIR) difference spectroscopy.²⁹ A corresponding NH band was absent in the FTIR difference spectra of Y_D ,²⁹ suggesting the difference in the hydrogen-bonded structure and proton transfer mechanism between Y_Z and Y_D . It has also been suggested that some other nearby

residues function as proton acceptors of Y_D .^{34, 35} Saito et al.¹⁵ performed theoretical calculations of Y_D reactions using the high-resolution (1.9 Å) X-ray structure of PSII. The result showed that when Y_D was oxidized, its proton is transferred away from Y_D to the luminal side through a water chain near Y_D , and they suggested that this long-distance proton transfer is the cause of the much slower rate of the Y_D reaction compared with that of the Y_Z reaction.

To understand the mechanism of the functional difference between Y_Z and Y_D in PSII, it is crucial to experimentally monitor the fate of the proton released from Y_D upon its photooxidation and to determine whether the proton is released from the protein or trapped in a certain residue in the protein. In the present study, we estimated the number of protons released into the bulk upon Y_D oxidation using light-induced FTIR difference spectroscopy. We employed the method that was previously used for the detection of protons from WOC during water oxidation:³⁶ protons trapped by the Mes buffer were monitored by isotope-edited Mes signals in light-induced FTIR difference spectra. The results showed that the proton from Y_D is released from the protein upon oxidation, supporting the theoretical prediction by Saito et al.¹⁵ The structural factors contributing to the difference in the proton transfer reactions of Y_Z and Y_D and their relevance to the functions of these Tyr residues are discussed.

3.2. Materials and Methods

PSII core complexes of *Thermosynechococcus elongatus*, in which the C-terminus of the CP47 subunit was histidine tagged,³⁷ were isolated following the method described previously.²⁹ Mn depletion was performed by 10 mM NH_2OH treatment for 30 min at room temperature. The Mn-depleted core complexes were then washed more than four times with a buffer containing 1 mM Mes-NaOH (pH 6.5), 5 mM NaCl, and 0.06% DM by ultrafiltration (Vivaspin 500; 100 kDa MWCO; Sartorius Stedim) to be finally concentrated to 3 mg chlorophyll/mL.

For Y_D^\bullet/Y_D FTIR measurements, an aliquot (5 μ L) of the Mn-depleted PS II sample (3 mg chlorophyll/mL) in the 1 mM Mes buffer mentioned above was mixed with 1 μ L of 20 mM potassium ferricyanide, 1 μ L of 40 mM potassium ferrocyanide, and 2 μ L of 200 mM Mes or Mes- d_{12} (pH 6.5).⁴⁸ The Mes- d_{12} buffer was prepared by dissolving all-deuterated Mes (Mes- d_{13} ; Cambridge Isotope Laboratories, Inc., 98% D) in H_2O , where the sulfonic acid group is ionized. To make a hydrated film, the sample was first dried on a BaF_2 plate (25 \times 25 mm²) under a N_2 gas flow and then sealed with another BaF_2 plate and a silicone spacer (0.5 mm in thickness). In the sealed cell, 2 μ L of 40% (v/v) glycerol/ H_2O was enclosed without touching the sample to produce 95% relative humidity.³⁸ The sample cell was cooled to 10 °C by circulating the cold water in a copper holder.

Light-induced FTIR spectra were recorded on a Bruker IFS-66/S spectrophotometer equipped with an MCT detector (D313-L). Flash illumination was performed using a Qswitched Nd:YAG laser (Quanta-Ray INDI-40-10; 532 nm; ~7 ns full-width at half-maximum; ~7 mJ pulse⁻¹ cm⁻²). For Y_D[•]/Y_D difference spectra, single-beam spectra with 100 scans (50 s accumulation) were recorded twice before illumination, once after one flash, and once after additional five flashes (1 Hz). This measurement was repeated 100 times with a dark interval of 450 s, and the spectra were averaged. Note that Y_D[•] was rereduced by ferrocyanide ($\tau \sim 200$ s) during this dark interval. The Y_D[•]/Y_D difference spectrum was obtained by taking the difference between the spectra after the first flash and the next five flashes, whereas the difference between the two spectra before illumination represents a noise level and a background change. The spectrum upon the first flash involves the contamination of the Fe²⁺/Fe³⁺ signal of the nonheme iron on the electron acceptor side^{39, 40} because the nonheme iron was partially preoxidized in the ferricyanide/ferrocyanide redox couple and accepted an electron at the first flash. However, the signals of the nonheme iron were not involved after the second flash because it was fully reduced by the first flash. By contrast, the quantum efficiency of Y_D oxidation is relatively low; hence, full accumulation of the oxidized Y_D[•] requires several flashes. Thus, the difference spectrum by the next five flashes provided a pure Y_D[•]/Y_D spectrum without contamination of the nonheme iron. There was no contribution of the signals from Y_Z and the Q_A and Q_B electron acceptors because of the fast relaxation of Y_Z[•] at 10 °C and the quick electron transfer from the quinone to ferricyanide, which was confirmed by the absence of signals typical of Y_Z[•] (CO stretch at 1515 cm⁻¹) and Q_{A(B)}⁻ (CO/CC stretch at ~1480 cm⁻¹). Because reduction of the nonheme iron is known to accompany the uptake of a proton,⁴¹ we abandoned the difference spectrum by the first flash and that by the next five flashes was adopted as a Y_D[•]/Y_D difference spectrum to estimate the number of protons from Y_D.

For measurements of the FTIR difference spectra upon water oxidation at WOC, PSII complexes were washed with a buffer containing 1 mM Mes-NaOH (pH 6.5), 5 mM NaCl, 5 mM CaCl₂, and 0.06% DM and were concentrated to 3 mg chlorophyll/mL by ultrafiltration. An aliquot (5 μ L) of a PSII suspension was mixed with 1 μ L of 100 mM potassium ferricyanide and 2 μ L of 200 mM Mes or Mes-*d*₁₂ (pH 6.5).³⁶ A hydrated film was prepared using the same procedure used for the Y_D measurements. The sample temperature was maintained at 10 °C. Single-beam spectra with 40 scans (20 s accumulation) were recorded twice before flashes and once after 12 flashes (1 Hz). The measurement was repeated six times with a dark interval of 90 min. The spectra were averaged for the calculation of a light-minus-dark difference spectrum.

Y_Z[•]/Y_Z FTIR spectra were measured following the method described previously²⁹ with slight modification. An aliquot (6 μ L) of Mn-depleted PSII core complexes (6 mg chlorophyll/mL) in a buffer containing 1 mM Mes-NaOH (pH 6.5), 40 mM sucrose, 10 mM NaCl,

5 mM MgCl₂, and 0.06% DM was mixed with 1 μL of 100 mM potassium ferricyanide and 1 μL of 200 mM Mes or Mes-*d*₁₂ (pH 6.5). After the sample was dried on a BaF₂ plate (13 mm in diameter) under a N₂ gas flow, it was mixed with 1 μL of 200 mM Mes or Mes-*d*₁₂ (pH6.5) and then sandwiched with another BaF₂ plate. The sample temperature was adjusted to 250 K in a cryostat (Oxford DN1704). Single-beam spectra with 50 scans (25 s accumulation) were recorded twice before and once after applying a single flash. This measurement was repeated 400 times with a dark interval of 225 s, and the average spectra were used to calculate a Y_Z[•]/Y_Z spectrum.

Spectral fitting to estimate the number of protons trapped by Mes was performed using Igor Pro (WaveMetrics Inc.). The regions of 1330–1150 and 2800–2400 cm⁻¹ were separately fitted, and the estimated values were averaged to obtain a final value.

3.3. Results

In this study, we applied the proton detection method using FTIR spectroscopy, which was developed by Suzuki et al.³⁶ to monitor the proton release during water oxidation at WOC, to the proton release from Y_D upon its photo-oxidation. In this method, protons released from PSII core complexes into the bulk were trapped by a high-concentration Mes buffer, and the protonation reaction of a Mes molecule (Figure 3.1) was monitored by FTIR difference spectroscopy. The FTIR signals of only Mes molecules were obtained by taking a double difference between Mes and deuterated Mes (Mes-*d*₁₂) to cancel the protein bands. At the same time, electron transfer was monitored using the CN stretching band of ferricyanide, which functions as an exogenous electron acceptor of PSII. Thus, the number of protons released from PSII during one turnover reaction of electron transfer can be estimated.³⁶

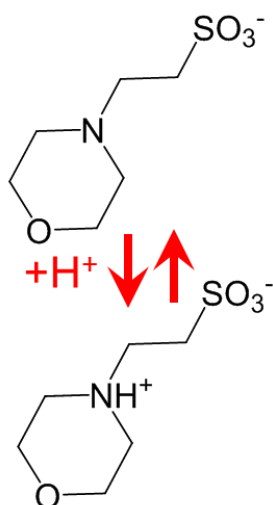


Figure 3.1 Protonation and deprotonation reactions of a Mes molecule

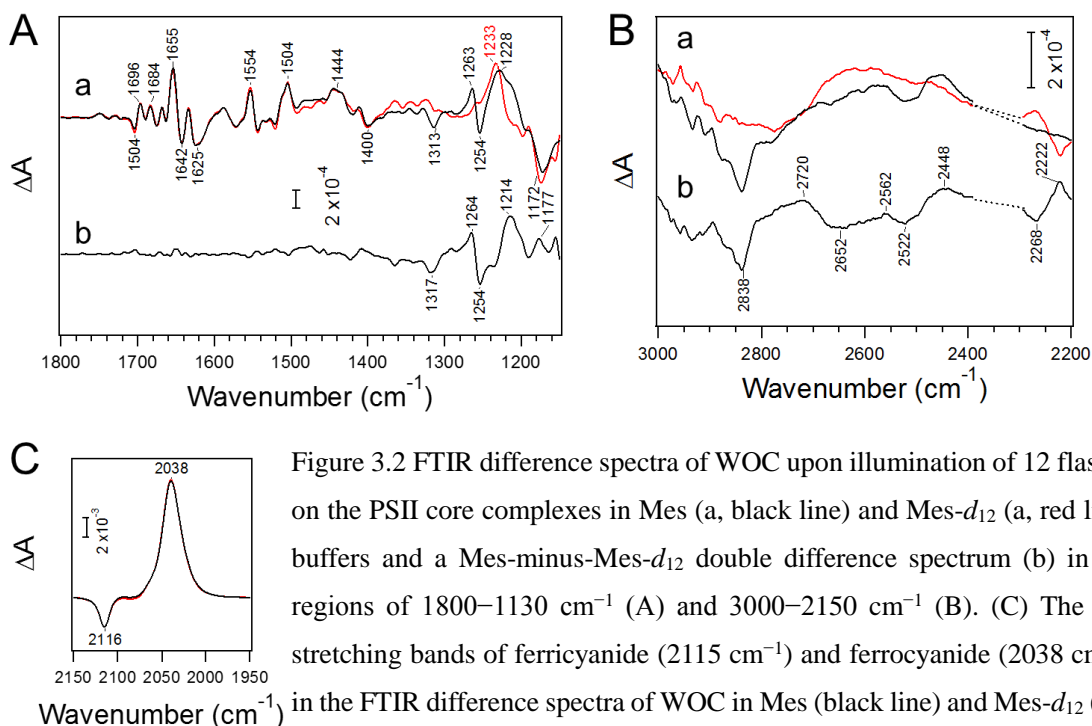


Figure 3.2 FTIR difference spectra of WOC upon illumination of 12 flashes on the PSII core complexes in Mes (a, black line) and Mes- d_{12} (a, red line) buffers and a Mes-minus-Mes- d_{12} double difference spectrum (b) in the regions of 1800–1130 cm^{-1} (A) and 3000–2150 cm^{-1} (B). (C) The CN stretching bands of ferricyanide (2115 cm^{-1}) and ferrocyanide (2038 cm^{-1}) in the FTIR difference spectra of WOC in Mes (black line) and Mes- d_{12} (red line). The dotted lines in panel B are the frequency region of CO_2 in atmosphere.

Y_D/Y_D difference spectra were measured using a hydrated film of PSII complexes.^{29, 42} The CN band of ferricyanide at 2115 cm^{-1} was slightly wider in the hydrated film than in the solution sample previously used.³⁶ Thus, we first performed proton detection from WOC using the film sample to determine the standard intensity of the Mes signal relative to the intensity of the ferricyanide band for the same amounts of Mes and ferricyanide. Because water oxidation at WOC generates four protons and four electrons per one S-state cycle, the numbers of protons and electrons from WOC should be identical when a relatively large number of flashes are applied to PSII.

Figure 3.2 shows FTIR difference spectra of WOC upon illumination of 12 flashes on the PSII samples in Mes (a, black line) and Mes- d_{12} (a, red line) buffers (Figure 3.2A, 1800–1130 cm^{-1} ; Figure 3.2B, 3000–2150 cm^{-1}). The spectra in trace a are normalized at the ferricyanide band at 2115 cm^{-1} (Figure 3.2C). (Note that the ferricyanide peak was used for normalization rather than the stronger ferrocyanide peak at 2038 cm^{-1} because the latter signal often changes the shape depending on the condition.³⁶) The spectra represent the structural difference between the dark stable S_1 state and randomized S states as well as protonation of the Mes buffer by protons produced by water oxidation. The frequency region lower than 1130 cm^{-1} , which was used in the previous proton detection study,³⁶ was not shown in Figure 3.2 because the spectra in this region

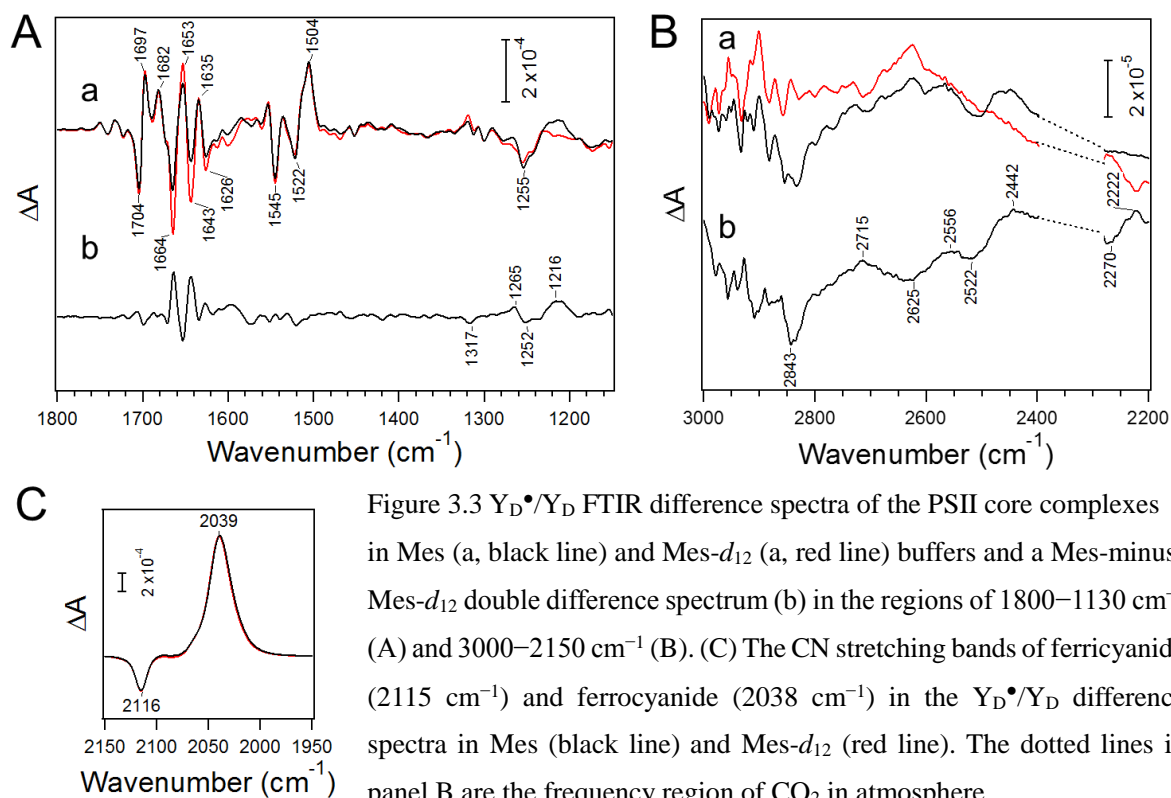


Figure 3.3 Y_D^\bullet/Y_D FTIR difference spectra of the PSII core complexes in Mes (a, black line) and Mes- d_{12} (a, red line) buffers and a Mes-minus-Mes- d_{12} double difference spectrum (b) in the regions of 1800–1130 cm^{-1} (A) and 3000–2150 cm^{-1} (B). (C) The CN stretching bands of ferricyanide (2115 cm^{-1}) and ferrocyanide (2038 cm^{-1}) in the Y_D^\bullet/Y_D difference spectra in Mes (black line) and Mes- d_{12} (red line). The dotted lines in panel B are the frequency region of CO_2 in atmosphere.

were found to be slightly saturated because of the relatively low sensitivity of the MCT detector and the large buffer absorption. In the present study, in addition to the mid-infrared region (Figure 3.2A), the high-frequency region (3000–2150 cm^{-1} ; Figure 3.2B) was newly used for detection of proton release. This region involves the vibrations of the CH stretches ($\sim 2840 \text{ cm}^{-1}$), the NH stretch (2800–2400 cm^{-1}) probably coupled with the overtones and combinations of lower frequency vibrations, and the CD stretches (2270–2220 cm^{-1}) of Mes and/or Mes- d_{12} . The merit of using this high frequency region is that major protein bands of WOC and Y_D are absent;^{29, 43} hence, the bands of Mes buffer mostly appear in this region. The Mes-only signals without protein contributions were obtained in a Mes-minus-Mes- d_{12} double difference spectrum (Figure 3.2A,B; trace b). It was shown that the bands of Mes affected by its protonation are located in frequencies lower than 1350 cm^{-1} and higher than 2200 cm^{-1} .

Figure 3.3 shows Y_D^\bullet/Y_D FTIR difference spectra of PSII samples in Mes (a, black line) and Mes- d_{12} (a, red line) buffers (Figure 3.3A, 1800–1130 cm^{-1} ; Figure 3.3B, 3000–2150 cm^{-1}). These spectra are virtually identical to the previously reported Y_D^\bullet/Y_D difference spectra.^{23, 29, 35, 42, 44-48} The positive peak at 1504 cm^{-1} and the negative peak at 1255 cm^{-1} originate from the CO stretch of Y_D^\bullet and the coupled mode of the CO stretch/COH bend of Y_D , respectively.^{35, 45, 49} The Mes-minus-Mes- d_{12} double difference spectrum of Y_D (Figures 3.3A,B; trace b) showed several bands in the regions of 1350–1130 and 2850–2200 cm^{-1} , very similar to those of the

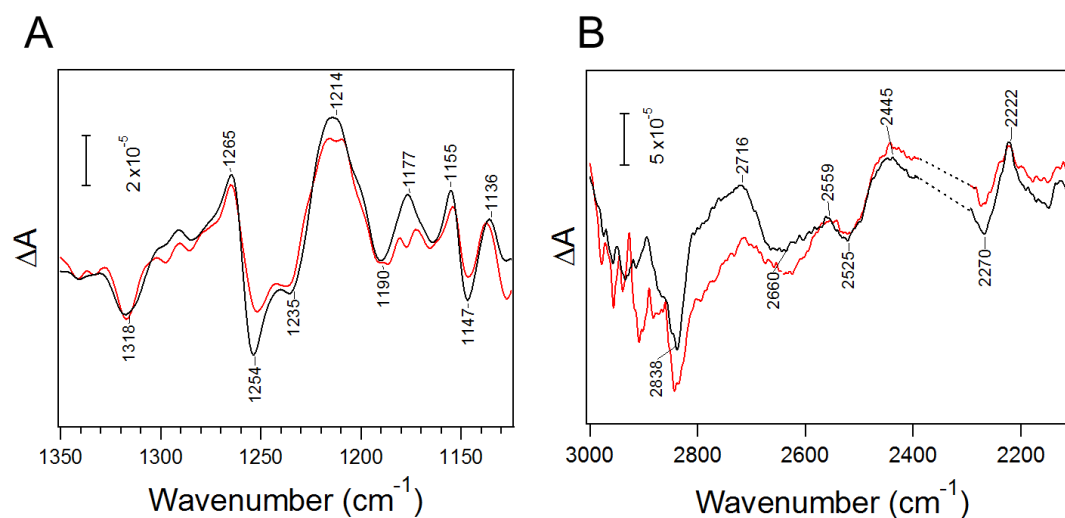


Figure 3.4 Comparison of the Mes-minus-Mes- d_{12} double difference spectra of WOC (black line) and Y_D^\bullet/Y_D (red line) in the regions of 1350–1130 cm^{-1} (A) and 3000–2150 cm^{-1} (B). The intensity of the spectrum of WOC was scaled based on the intensity of the ferricyanide peak at 2115 cm^{-1} in the original difference spectrum (Figure 3C, black line) relative to that of Y_D^\bullet/Y_D (Figure 4C, black line). The dotted lines in panel B are the frequency region of CO_2 in atmosphere.

corresponding double difference spectrum of WOC (Figures 3.2A,B; trace b). Note that some bands around 1650 cm^{-1} (Figure 3.3A; trace b) are artifacts due to the saturation of absorption by strong amide I and water bending bands ($A \sim 1.2$) in the samples for the Y_D^\bullet/Y_D measurement. As shown in trace b of Figure 3.2A, no Mes signal originated in this region.

To estimate the number of protons released from Y_D , the intensity of the Mes-minus-Mes- d_{12} double difference spectrum of WOC (Figures 3.2A,B; trace b) was normalized to that of Y_D (Figures 3.3A,B; trace b) so that the intensity of the ferricyanide band at 2115 cm^{-1} in the original difference spectrum (Figure 3.2C) was adjusted to that of the Y_D^\bullet/Y_D spectrum (Figure 3.3C). Thus, the number of protons released from WOC and that from Y_D can be compared with respect to the same number of electrons transferred to ferricyanide on the electron acceptor side. Because an average of one proton is released from WOC per one electron transferred to ferricyanide (12 flashes are sufficient to randomize the S-state cycle), the relative intensity of the Mes signal indicates the number of protons released by the oxidation of one Y_D . In Figure 3.4, the normalized Mes spectra of WOC (black line) and Y_D (red line) are compared in the regions of 1350–1130 (Figure 3.4A) and 3000–2150 cm^{-1} (Figure 3.4B). The intensity ratio of the Mes signals of Y_D relative to those of WOC was estimated by fitting the spectra in the regions of 1330–1150 and 2800–2400 cm^{-1} , yielding a value of 0.84 ± 0.10 . This result indicates that 0.8–0.9 protons are released into the bulk upon oxidation of one Y_D .

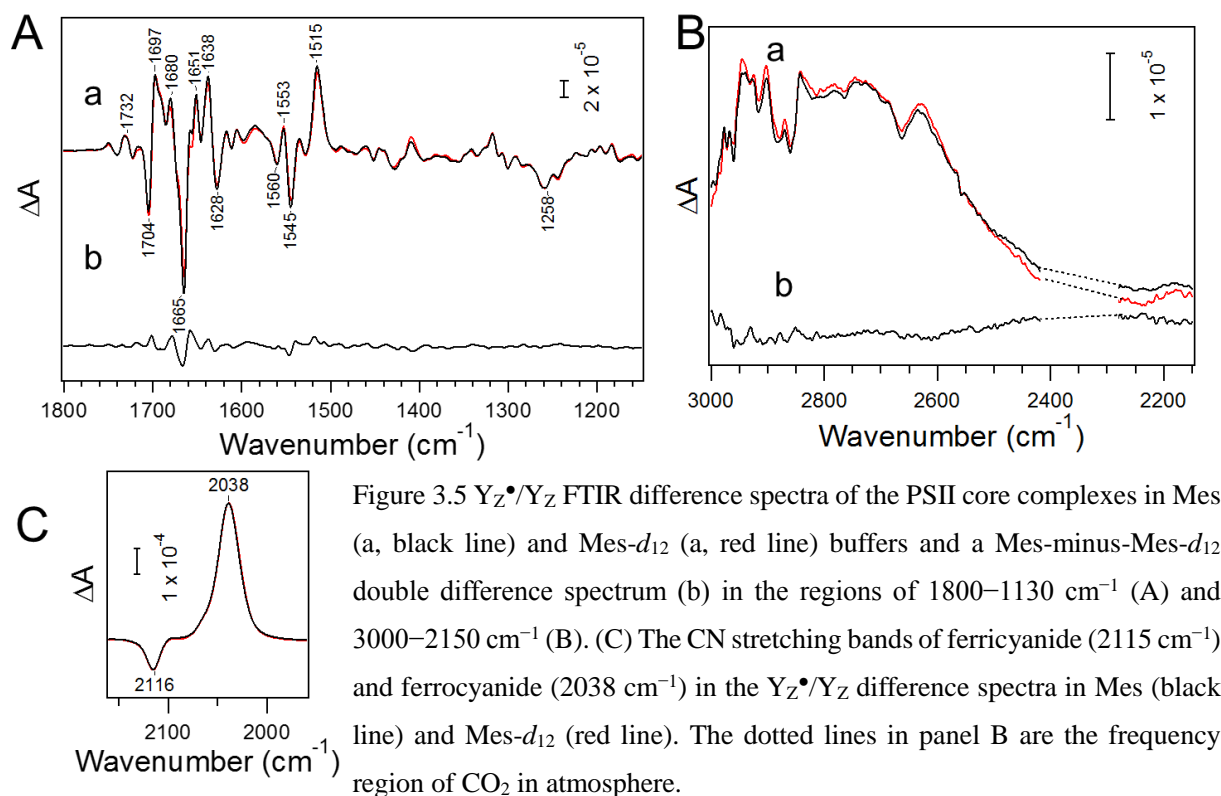


Figure 3.5 Y_Z^\bullet/Y_Z FTIR difference spectra of the PSII core complexes in Mes (a, black line) and Mes- d_{12} (a, red line) buffers and a Mes-minus-Mes- d_{12} double difference spectrum (b) in the regions of 1800–1130 cm^{-1} (A) and 3000–2150 cm^{-1} (B). (C) The CN stretching bands of ferricyanide (2115 cm^{-1}) and ferrocyanide (2038 cm^{-1}) in the Y_Z^\bullet/Y_Z difference spectra in Mes (black line) and Mes- d_{12} (red line). The dotted lines in panel B are the frequency region of CO_2 in atmosphere.

As a control experiment, we studied proton release into the bulk upon Y_Z oxidation. Figure 3.5 shows the Y_Z^\bullet/Y_Z FTIR difference spectra in high-concentration Mes and Mes- d_{12} buffers in the regions of 1800–1130 (Figure 3.5A) and 3000–2150 cm^{-1} (Figure 3.5B) with ferricyanide/ferrocyanide peaks at 2115/2038 cm^{-1} (Figure 3.5C). The spectra were characterized by a positive peak at 1515 cm^{-1} arising from the CO stretching vibration of Y_Z^\bullet ,²⁹ which was detected at a higher frequency by 11 cm^{-1} compared with the corresponding peak of Y_D^\bullet at 1504 cm^{-1} (Figure 3.3A). It was shown that the spectra in Mes and Mes- d_{12} are virtually identical, which was confirmed by their double difference spectrum showing no specific bands throughout the regions (trace b in Figure 3.5A,B). In Figure 3.6, the double difference spectrum is compared with the corresponding spectrum of WOC, which was normalized with the intensity of the ferricyanide band at 2115 cm^{-1} in a way that was analogous to the Y_D case. It was shown that the isotopeedited Mes bands by Y_Z oxidation are almost undetectable and, hence, significantly smaller than those of WOC. This observation confirms that a proton is virtually unreleased into the bulk when Y_Z is oxidized.

3.4. Discussion

We estimated the number of protons that are released from the proteins upon oxidation

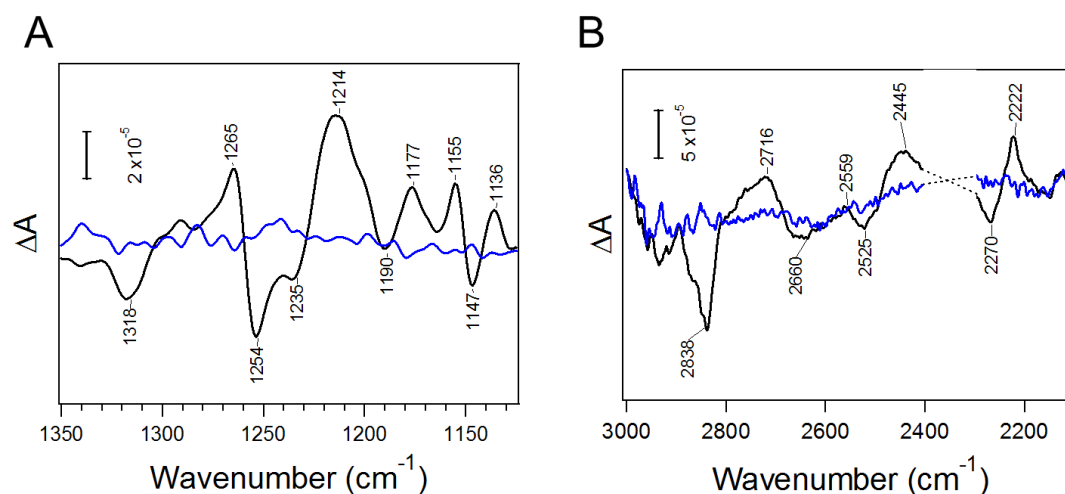


Figure 3.6 Comparison of the Mes-minus-Mes- d_{12} double difference spectra of WOC (black line) and Y_Z^\bullet/Y_Z (blue line) in the regions of 1350–1130 cm^{-1} (A) and 3000–2150 cm^{-1} (B). The intensity of the spectrum of WOC was scaled based on the intensity of the ferricyanide peak at 2115 cm^{-1} in the original difference spectrum (Figure 3C, black line) relative to that of Y_Z^\bullet/Y_Z (Figure 6C, black line). The dotted lines in panel B are the frequency region of CO_2 in atmosphere.

of Y_D using the proton detection method that utilizes isotope-edited FTIR signals of Mes buffer (Mes-minus-Mes- d_{12}).³⁶ By comparing these Mes signals by Y_D oxidation with the standard Mes signals by water oxidation, we showed that 0.84 ± 0.10 protons are released into the bulk upon oxidation of Y_D (Figure 3.4). This result indicates that the proton of Y_D is mostly released from the proteins and is not trapped by the neighboring D2-His189 with a putative hydrogen bond with Y_D . This is consistent with our recent FTIR result showing that no $\text{N}\tau\text{-H}$ stretching band of protonated HisH^+ corresponding to a broad band at $\sim 2800 \text{ cm}^{-1}$ due to protonated D1-His190 in a Y_Z^\bullet/Y_Z spectrum was detected in a Y_D^\bullet/Y_D spectrum.²⁹ The absence of proton release into the bulk upon Y_Z , in contrast to Y_D , oxidation was confirmed by FTIR measurements of Y_Z^\bullet/Y_Z in Mes and Mes- d_{12} buffers (Figure 3.5). The Mes-minus-Mes- d_{12} double difference spectrum showed almost no feature (Figure 3.6). This observation also demonstrates the validity of the proton detection method using the Mes signals.

The absence of a proton trap by the Mes buffer upon Y_Z oxidation (Figure 3.6) further suggests that the detection of proton release upon Y_D oxidation is not an artifact induced by high-concentration Mes buffer. In addition, previous Y_D^\bullet/Y_D FTIR spectra measured in a lower concentration buffer at pH 6.0^{35, 45} showed a broad positive feature around 1720 cm^{-1} , indicative of the protonation of nonspecific carboxylate groups on the protein surface by protons released

into the bulk. These observations suggest that high-concentration Mes buffer does not influence the proton release reaction from Y_D , and the number of protons detected by the Mes buffer reflects the real number of protons released from Y_D upon its oxidation.

The remaining 0.1–0.2 protons, which were not detected by the Mes buffer in the bulk, may be trapped in the proteins. A previous EPR study conducted by Faller et al.¹⁰ showed the rapid formation of Y_D^\bullet at higher pHs with a pK_a of 7.7. Hienerwadel et al.³⁵ also showed in their FTIR study the change in the hydrogen bond interaction of the reduced form of Y_D with pK_a of ~7. The presence of a proton acceptor with a pK_a of 7.0–7.7, which was speculated to be the imidazolate form of D2-His189 (see below),¹⁵ explains the remaining proton of ~15% at pH 6.5, the pH used in the present study.

It has been generally thought that the proton of Y_D is transferred to D2-His189, which is most probably hydrogen-bonded with Y_D ,^{16-20, 28, 50-52} similar to the case of Y_Z , whose proton is transferred to the neighboring D1-His190 upon its oxidation.^{7, 26, 27, 29-33} However, theoretical calculation by Saito et al.¹⁵ based on the 1.9 Å resolution structure of PSII¹⁸ showed that the proton of Y_D is not trapped by D2-His189 but moves to the hydrogen-bonded water molecule and is then transferred away from Y_D through a hydrogen bond network involving a water chain (Figure 2.1A). They suggested that the proton is released into the bulk via D2-His61 located in the proton pathway. Our FTIR data showing proton detection in the bulk upon Y_D oxidation is in agreement with this theoretical prediction and hence supports the proton release process proposed by Saito et al.¹⁵

The clear difference in the proton transfer reactions between Y_Z and Y_D arises from the difference in the hydrogen-bonded structures of these Tyr side chains, the coupled His (D1-His190 and D2-His189, respectively), and the amino acid residue hydrogen-bonded to the $N\pi$ site of this His (Figure 3.7). Whereas the amide C=O of D1-Asn298 interacts with D1-His190 as a hydrogen bond acceptor (Figure 3.7B), D2-Arg294, which most probably has a guanidinium cation form, donates a hydrogen bond to D2-His189 coupled to Y_D . Because of these different hydrogen bond interactions of D1-Asn298 and D2-Arg294 at the $N\pi$ site, D1-His190 and D2-His189, in turn, function as a hydrogen bond acceptor and donor, respectively, to the phenolic oxygen of Tyr.^{15, 29} Thus, whereas the proton of Y_Z is transferred to D1-His190 through a hydrogen bond, the proton of Y_D cannot be transferred to D1-His189, which is already protonated at the $N\tau$ site, but it is transferred to a hydrogen-bonded water molecule, leading to a long-distance proton transfer (Figure 3.7).¹⁷ The presence of such a water molecule interacting with Y_D was also detected by the previous FTIR measurement.⁴² The hydrogen bond network from Y_D to the luminal side via D2-Arg180 and D2-His61 (Figure 2.1A), involving the movement of a hydronium cation from Y_D to D2-Arg180 shown in the quantum mechanics/molecular mechanics (QM/MM) study of Saito et al.,¹⁵ may be used for the proton release pathway upon Y_D oxidation. Site-directed mutants

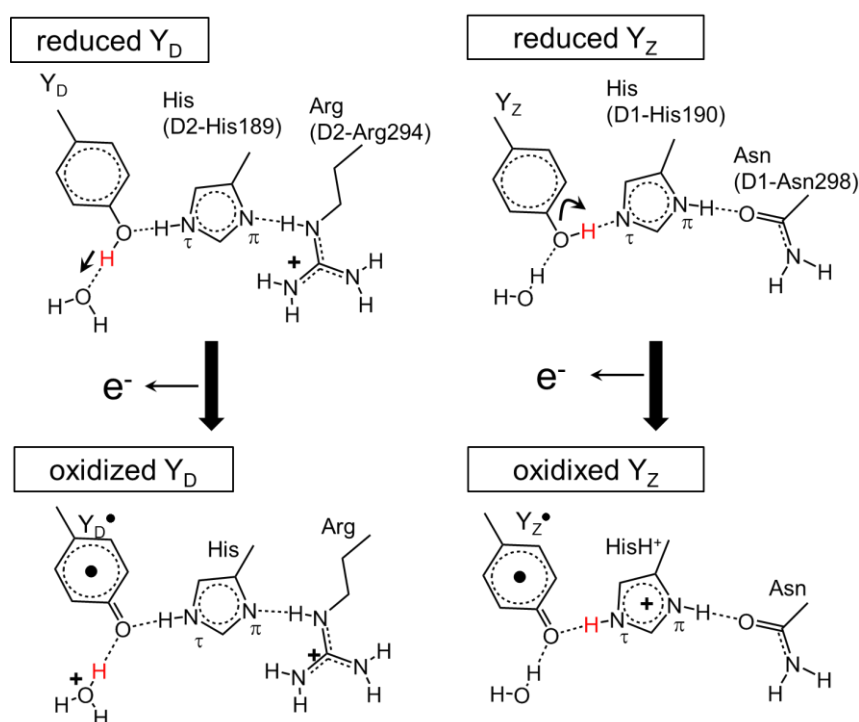


Figure 3.7 Schematic picture of the hydrogen-bonded structures of Y_D -His (left) and Y_Z -His (right) and the proton transfer reactions upon oxidation.

at D2-Arg180 showed significant alterations of the EPR signal of Y_D^\bullet , indicating a strong interaction between Y_D and D2-Arg180,³⁴ and it was recently shown that a water molecule between Y_D and D2-Arg180 is important for the H/D exchange of Y_D .⁵³ These observations also support the significance of the hydrogen bond network via D2-Arg180 as a proton pathway from Y_D to the bulk.¹⁵

Oxidation and reduction of Y_D slower than that of Y_Z ^{8,11} can be explained by this long-distance proton transfer for Y_D , providing a high-energy barrier in the reaction coordinate,¹⁵ in contrast to the short proton transfer for Y_Z through a strong hydrogen bond, which requires almost no energy barrier.²⁷ Previous observations of the fast redox reaction and low-temperature oxidation of Y_D at high pH values^{10, 21, 22, 24} are explained by deprotonation of D2-His189 to be an imidazolite anion form inducing rapid proton transfer from Y_D to D2-His189 without proton release into the bulk.¹⁵ In addition, the lower E_m value of Y_D (+700–800 mV)^{8, 54} than that of Y_Z (+900–1000 mV)^{8, 55} may be partly attributed to the stabilization of the oxidized form of Y_D due to an entropy increase by the diffusion of a proton into the bulk, in addition to the electrostatic effects of partial charges in the protein moieties.⁵⁶

In conclusion, we provided experimental evidence that the proton of Y_D is released from the protein upon its oxidation, supporting the previous QM/MM study by Saito et al.¹⁵ This long-distance proton transfer should significantly contribute to the functional difference between Y_D

and Y_Z. The key amino acid residues controlling the hydrogen-bonded structures and proton transfer reactions of Y_D and Y_Z are D2-Arg294 and D1-Asn298 interacting with the coupled His as a hydrogen bond donor and acceptor, respectively, in the Y_D-His-Arg and Y_Z-His-Asn triads.

References

- [1] Diner, B. A., and Britt, R. D. (2005) The redox-active tyrosines Y_Z and Y_D, In *Photosystem II: The Light-Driven Water: Plastoquinone Oxidoreductase* (Wydrzynski, T. J., and Satoh, K., Eds.), pp 207-233, Springer, Dordrecht, The Netherlands.
- [2] Renger, G., and Renger, T. (2008) Photosystem II: The machinery of photosynthetic water splitting, *Photosynth. Res.* 98, 53-80.
- [3] Rappaport, F., Blanchard-Desce, M., and Lavergne, J. (1994) Kinetics of electron transfer and electrochromic change during the redox transitions of the photosynthetic oxygen-evolving complex, *Biochim. Biophys. Acta* 1184, 178-192.
- [4] Haumann, M., Liebisch, P., Muller, C., Barra, M., Grabolle, M., and Dau, H. (2005) Photosynthetic O₂ formation tracked by time-resolved X-ray experiments, *Science* 310, 1019-1021.
- [5] Noguchi, T., Suzuki, H., Tsuno, M., Sugiura, M., and Kato, C. (2012) Time-resolved infrared detection of the proton and protein dynamics during photosynthetic oxygen evolution, *Biochemistry* 51, 3205-3214.
- [6] Klauss, A., Haumann, M., and Dau, H. (2015) Seven steps of alternating electron and proton transfer in photosystem II water oxidation traced by time-resolved photothermal beam deflection at improved sensitivity, *J. Phys. Chem. B* 119, 2677-2689.
- [7] Styring, S., Sjöholm, J., and Mamedov, F. (2012) Two tyrosines that changed the world: Interfacing the oxidizing power of photochemistry to water splitting in photosystem II, *Biochim. Biophys. Acta* 1817, 76-87.
- [8] Vass, I., and Styring, S. (1991) pH-Dependent charge equilibria between tyrosine-D and the S states in photosystem II. Estimation of relative midpoint redox potentials, *Biochemistry* 30, 830-839.
- [9] Styring, S., and Rutherford, A. W. (1987) In the oxygen-evolving complex of Photosystem II the S₀ state is oxidized to the S₁ state by D⁺ (Signal II slow), *Biochemistry* 26, 2401-2405.
- [10] Faller, P., Debus, R. J., Brettel, K., Sugiura, M., Rutherford, A. W., and Boussac, A. (2001) Rapid formation of the stable tyrosyl radical in photosystem II, *Proc. Natl. Acad. Sci. U. S. A.* 98, 14368-14373.
- [11] Buser, C. A., Thompson, L. K., Diner, B. A., and Brudvig, G. W. (1990) Electron-transfer

- reactions in manganese-depleted photosystem II, *Biochemistry* 29, 8977-8985.
- [12] Rutherford, A. W., Boussac, A., and Faller, P. (2004) The stable tyrosyl radical in photosystem II: why D?, *Biochim. Biophys. Acta* 1655, 222-230.
- [13] Magnuson, A., Rova, M., Mamedov, F., Fredriksson, P. O., and Styring, S. (1999) The role of cytochrome b_{559} and tyrosine_D in protection against photoinhibition during in vivo photoactivation of photosystem II, *Biochim. Biophys. Acta* 1411, 180-191.
- [14] Ananyev, G. M., Sakiyan, I., Diner, B. A., and Dismukes, G. C. (2002) A functional role for tyrosine-D in assembly of the inorganic core of the water oxidase complex of photosystem II and the kinetics of water oxidation, *Biochemistry* 41, 974-980.
- [15] Saito, K., Rutherford, A. W., and Ishikita, H. (2013) Mechanism of tyrosine D oxidation in Photosystem II, *Proc. Natl. Acad. Sci. U.S.A.* 110, 7690-7695.
- [16] Ferreira, K. N., Iverson, T. M., Maghlaoui, K., Barber, J., and Iwata, S. (2004) Architecture of the photosynthetic oxygen-evolving center, *Science* 303, 1831-1838.
- [17] Guskov, A., Kern, J., Gabdulkhakov, A., Broser, M., Zouni, A., and Saenger, W. (2009) Cyanobacterial photosystem II at 2.9 Å resolution and the role of quinones, lipids, channels and chloride, *Nat. Struct. Mol. Biol.* 16, 334-342.
- [18] Umena, Y., Kawakami, K., Shen, J. R., and Kamiya, N. (2011) Crystal structure of oxygen-evolving photosystem II at a resolution of 1.9 Å, *Nature* 473, 55-60.
- [19] Suga, M., Akita, F., Hirata, K., Ueno, G., Murakami, H., Nakajima, Y., Shimizu, T., Yamashita, K., Yamamoto, M., Ago, H., and Shen, J. R. (2015) Native structure of photosystem II at 1.95 Å resolution viewed by femtosecond X-ray pulses, *Nature* 517, 99-103.
- [20] Babcock, G. T., Barry, B. A., Debus, R. J., Hoganson, C. W., Atamian, M., McIntosh, L., Sithole, I., and Yocum, C. F. (1989) Water oxidation in photosystem II: From radical chemistry to multielectron chemistry, *Biochemistry* 28, 9557-9565.
- [21] Faller, P., Rutherford, A. W., and Debus, R. J. (2002) Tyrosine D oxidation at cryogenic temperature in photosystem II, *Biochemistry* 41, 12914-12920.
- [22] Faller, P., Goussias, C., Rutherford, A. W., and Un, S. (2003) Resolving intermediates in biological proton-coupled electron transfer: a tyrosyl radical prior to proton movement, *Proc. Natl. Acad. Sci. U. S. A.* 100, 8732-8735.
- [23] Berthomieu, C., and Hienerwadel, R. (2005) Vibrational spectroscopy to study the properties of redox-active tyrosines in photosystem II and other proteins, *Biochim. Biophys. Acta* 1707, 51-66.
- [24] Havelius, K. G., and Styring, S. (2007) pH dependent competition between Y_Z and Y_D in photosystem II probed by illumination at 5 K, *Biochemistry* 46, 7865-7874.
- [25] Hammarström, L., and Styring, S. (2011) Proton-coupled electron transfer of tyrosines in

- Photosystem II and model systems for artificial photosynthesis: the role of a redox-active link between catalyst and photosensitizer, *Energy Environ. Sci.* *4*, 2379-2388.
- [26] Matsuoka, H., Shen, J. R., Kawamori, A., Nishiyama, K., Ohba, Y., and Yamauchi, S. (2011) Proton-coupled electron-transfer processes in photosystem II probed by highly resolved g-anisotropy of redox-active tyrosine Y_Z, *J. Am. Chem. Soc.* *133*, 4655-4660.
- [27] Saito, K., Shen, J. R., Ishida, T., and Ishikita, H. (2011) Short hydrogen bond between redox-active tyrosine Y_Z and D1-His190 in the photosystem II crystal structure, *Biochemistry* *50*, 9836-9844.
- [28] Chatterjee, R., Coates, C. S., Milikisiyants, S., Lee, C. I., Wagner, A., Poluektov, O. G., and Lakshmi, K. V. (2013) High-frequency electron nuclear double-resonance spectroscopy studies of the mechanism of proton-coupled electron transfer at the tyrosine-D residue of photosystem II, *Biochemistry* *52*, 4781-4790.
- [29] Nakamura, S., Nagao, R., Takahashi, R., and Noguchi, T. (2014) Fourier transform infrared detection of a polarizable proton trapped between photooxidized tyrosine Y_Z and a coupled histidine in photosystem II: relevance to the proton transfer mechanism of water oxidation, *Biochemistry* *53*, 3131-3144.
- [30] Ahlbrink, R., Haumann, M., Cherepanov, D., Bogershausen, O., Mulikidjanian, A., and Junge, W. (1998) Function of tyrosine Z in water oxidation by photosystem II: Electrostatical promotor instead of hydrogen abstractor, *Biochemistry* *37*, 1131-1142.
- [31] Hays, A. M. A., Vassiliev, I. R., Golbeck, J. H., and Debus, R. J. (1999) Role of D1-His190 in the proton-coupled oxidation of tyrosine Y_Z in manganese-depleted photosystem II, *Biochemistry* *38*, 11851-11865.
- [32] Rappaport, F., and Lavergne, J. (2001) Coupling of electron and proton transfer in the photosynthetic water oxidase, *Biochim. Biophys. Acta* *1503*, 246-259.
- [33] Rappaport, F., Boussac, A., Force, D. A., Peloquin, J., Brynda, M., Sugiura, M., Un, S., Britt, R. D., and Diner, B. A. (2009) Probing the coupling between proton and electron transfer in photosystem II core complexes containing a 3-fluorotyrosine, *J. Am. Chem. Soc.* *131*, 4425-4433.
- [34] Manna, P., LoBrutto, R., Eijkelhoff, C., Dekker, J. P., and Vermaas, W. (1998) Role of Arg180 of the D2 protein in photosystem II structure and function, *Eur. J. Biochem.* *251*, 142-154.
- [35] Hienerwadel, R., Diner, B. A., and Berthomieu, C. (2008) Molecular origin of the pH dependence of tyrosine D oxidation kinetics and radical stability in photosystem II, *Biochim. Biophys. Acta* *1777*, 525-531.
- [36] Suzuki, H., Sugiura, M., and Noguchi, T. (2009) Monitoring proton release during photosynthetic water oxidation in photosystem II by means of isotope-edited infrared

- spectroscopy, *J. Am. Chem. Soc.* *131*, 7849-7857.
- [37] Iwai, M., Suzuki, T., Kamiyama, A., Sakurai, I., Dohmae, N., Inoue, Y., and Ikeuchi, M. (2010) The PsbK subunit is required for the stable assembly and stability of other small subunits in the PSII complex in the thermophilic cyanobacterium *Thermosynechococcus elongatus* BP-1, *Plant Cell Physiol.* *51*, 554-560.
- [38] Noguchi, T., and Sugiura, M. (2002) Flash-induced FTIR difference spectra of the water oxidizing complex in moderately hydrated photosystem II core films: Effect of hydration extent on Sstate transitions, *Biochemistry* *41*, 2322-2330.
- [39] Hienerwadel, R., and Berthomieu, C. (1995) Bicarbonate binding to the non-heme iron of photosystem II investigated by Fourier transform infrared difference spectroscopy and ¹³C-labeled bicarbonate, *Biochemistry* *34*, 16288-16297.
- [40] Noguchi, T., and Inoue, Y. (1995) Identification of Fourier transform infrared signals from the non-heme iron in photosystem II, *J. Biochem.* *118*, 9-12.
- [41] Berthomieu, C., and Hienerwadel, R. (2001) Iron coordination in photosystem II: interaction between bicarbonate and the Q_B pocket studied by Fourier transform infrared spectroscopy, *Biochemistry* *40*, 4044-4052.
- [42] Takahashi, R., Sugiura, M., and Noguchi, T. (2007) Water molecules coupled to the redox-active tyrosine Y_D in photosystem II as detected by FTIR spectroscopy, *Biochemistry* *46*, 14245-14249.
- [43] Noguchi, T., and Sugiura, M. (2002) FTIR detection of water reactions during the flash-induced S-state cycle of the photosynthetic water-oxidizing complex, *Biochemistry* *41*, 15706-15712.
- [44] Hienerwadel, R., Boussac, A., Breton, J., and Berthomieu, C. (1996) Fourier transform infrared difference study of tyrosine_D oxidation and plastoquinone Q_A reduction in photosystem II, *Biochemistry* *35*, 15447-15460.
- [45] Hienerwadel, R., Boussac, A., Breton, J., Diner, B. A., and Berthomieu, C. (1997) Fourier transform infrared difference spectroscopy of photosystem II tyrosine D using site-directed mutagenesis and specific isotope labeling, *Biochemistry* *36*, 14712-14723.
- [46] Hienerwadel, R., Gourion-Arsiquaud, S., Ballottari, M., Bassi, R., Diner, B. A., and Berthomieu, C. (2005) Formate binding near the redox-active tyrosine_D in photosystem II: consequences on the properties of tyr_D, *Photosynth. Res.* *84*, 139-144.
- [47] Noguchi, T., Inoue, Y., and Tang, X. S. (1997) Structural coupling between the oxygen-evolving Mn cluster and a tyrosine residue in photosystem II as revealed by Fourier transform infrared spectroscopy, *Biochemistry* *36*, 14705-14711.
- [48] Chu, H.-A., Hillier, W., and Debus, R. J. (2004) Evidence that the C-terminus of the D1 polypeptide of photosystem II is ligated to the manganese ion that undergoes oxidation

- during the S₁ to S₂ transition: An isotope-edited FTIR study, *Biochemistry* 43, 3152-3166.
- [49] Takahashi, R., and Noguchi, T. (2007) Criteria for determining the hydrogen-bond structures of a tyrosine side chain by Fourier transform infrared spectroscopy: Density functional theory analyses of model hydrogen-bonded complexes of *p*-cresol, *J. Phys. Chem. B* 111, 13833-13844.
- [50] Tommos, C., Davidsson, L., Svensson, B., Madsen, C., Vermaas, W., and Styring, S. (1993) Modified EPR spectra of the tyrosine_D radical in photosystem II in site-directed mutants of *Synechocystis* sp. PCC 6803: Identification of side chains in the immediate vicinity of tyrosine_D on the D2 protein, *Biochemistry* 32, 5436-5441.
- [51] Tang, X. S., Chisholm, D. A., Dismukes, G. C., Brudvig, G. W., and Diner, B. A. (1993) Spectroscopic evidence from site-directed mutants of *Synechocystis* PCC6803 in favor of a close interaction between histidine 189 and redox-active tyrosine 160, both of polypeptide D2 of the photosystem II reaction center, *Biochemistry* 32, 13742-13748.
- [52] Kessen, S., Teutloff, C., Kern, J., Zouni, A., and Bittl, R. (2010) High-Field ²H-mims-ENDOR spectroscopy on PSII single crystals: Hydrogen bonding of Y_D^{*}, *ChemPhysChem* 11, 1275-1282.
- [53] Sjöholm, J., Mamedov, F., and Styring, S. (2014) Spectroscopic evidence for a redox-controlled proton gate at tyrosine D in Photosystem II, *Biochemistry* 53, 5721-5723.
- [54] Boussac, A., and Etienne, A. L. (1984) Midpoint potential of signal-II (slow) in Tris-washed photosystem-II particles, *Biochim. Biophys. Acta* 766, 576-581.
- [55] Metz, J. G., Nixon, P. J., Rogner, M., Brudvig, G. W., and Diner, B. A. (1989) Directed alteration of the D1 polypeptide of photosystem II: Evidence that tyrosine-161 is the redox component, Z, connecting the oxygen-evolving complex to the primary electron-donor, P680, *Biochemistry* 28, 6960-6969.
- [56] Ishikita, H., and Knapp, E. W. (2006) Function of redox-active tyrosine in photosystem II, *Biophys. J.* 90, 3886-3896.

Vibrational analysis of water network around the Mn cluster

4.1. Introduction

Water oxidation proceeds through a cycle of five intermediates designated as S_n states ($n = 0-4$), with a larger value of n implying a higher oxidation state.^{1, 2} Among them, the S_1 state is the most stable in the dark and the S_n state ($n = 0-3$) advances to the S_{n+1} state by abstraction of an electron by a photo-oxidized chlorophyll dimer P680 through a redox-active tyrosine Y_Z (D1-Y161). The S_4 state is a transient state that immediately relaxes to the S_0 state by releasing O_2 . A breakthrough of the water oxidation research was the X-ray crystallographic structure of PSII at 1.9 Å resolution,³ which provided the atomic structure of WOC, including oxygen atoms bridging Mn and Ca ions, four water ligands, and two nearby Cl^- ions (Cl-1 and Cl-2). There was, however, a criticism that the Mn cluster in this structure suffered from damage by a large dose of X-ray radiation and actually represented oxidation states lower than the S_1 state.^{4, 5} Suga et al.⁶ recently reported a 1.95 Å structure free from X-ray damage obtained using ultrashort X-ray pulses from an X-ray free electron laser (XFEL) and showed that the basic structure of the Mn cluster was the same between the two structures, although partial reduction of Mn ions was found in the former 1.9 Å structure. In these 1.9–1.95 Å structures, in addition to the four water ligands (W1 and W2 attached to Mn4 and W3 and W4 to Ca), several water molecules were found interacting with the water ligands forming a hydrogen bond network between the Cl-1/D1-D61 and Y_Z sites.^{3, 6} However, without resolving hydrogen atoms, the protonation states of the water molecules and their hydrogen bond structures remain unknown.

During an S-state cycle, four protons are released by oxidation of two water molecules. The proton release pattern was shown to be 1:0:1:2 for the $S_0 \rightarrow S_1$, $S_1 \rightarrow S_2$, $S_2 \rightarrow S_3$, and $S_3 \rightarrow S_0$ transitions, respectively.⁷⁻⁹ Because an electron is abstracted in each transition, this proton release pattern indicates that an excessive positive charge accumulates on the Mn cluster in the S_2 and S_3 states. It was suggested that the presence of an excessive positive charge requires proton release before electron transfer in the $S_2 \rightarrow S_3$ and $S_3 \rightarrow S_0$ transitions, whereas an electron was proposed to be first transferred before proton transfer in the $S_0 \rightarrow S_1$ transition.¹⁰⁻¹⁵ In the clarification of the water oxidation mechanism, it is crucial to know which water molecule releases a proton and how the water network around the Mn cluster is used for the proton transfer.

Relevant unanswered questions are which channel leading from the WOC to the lumen^{3, 16-23} is functional in proton release and water insertion and whether the channel is different depending on the S-state transitions.

In this study, the role of the water network around the Mn cluster was investigated. We assigned the OH vibrations of water molecules in a Fourier transform infrared (FTIR) difference spectrum of WOC using quantum mechanics/molecular mechanics (QM/MM) calculations. Quantum chemical calculations were recently extensively applied to the water oxidation mechanism.^{4, 24-40} Density functional theory (DFT) and QM/MM calculations based on the X-ray crystallographic structures provided the structures of the Mn cluster in all the individual S states and hence could predict the reaction mechanism of water oxidation. Based on the result, the role of the water network in the water oxidation mechanism is discussed.

4.2. Materials and Methods

Quantum chemical calculations were performed using the Gaussian09 program package.⁴¹ QM/MM calculations were performed using the ONIOM (our own n-layered integrated molecular orbital and molecular mechanics) method⁴² as described previously.¹⁴ The atomic coordinates of amino acid residues, water molecules, the Mn cluster, and Cl⁻ ions located within 20 Å of the Ca atom were taken from the X-ray structure of the PSII complex at 1.95 Å resolution by XFEL [Protein Data Bank (PDB) entry 4UB6].⁶ The hydrogen atoms were generated and optimized using Amber. The QM region consists of the Mn cluster, Cl-1, nine water molecules near Ca [W1–W9 (see Figure 4.1 for the numbering of the water molecules)], amino acid ligands to the Mn and Ca ions (D1-D170, D1-E189, D1-H332, D1-E333, D1-D342, D1-A344, and CP43-E354), Yz, D1-H190, and nearby amino acid side chains and backbones (D1-D61, CP43-R357, D2-K317, and backbones between D1-F182 and D1-M183 and between D1-S169 and D1-G171), while other atoms in the selected region of PSII [amino acid residues and Cl⁻ within 20 Å of the Ca] were assigned to the MM region (Amber was used as a force field). The geometry of the QM region was optimized by fixing other atoms in the MM region using ONIOM (B3LYP:Amber). Normal mode calculations were performed for the optimized geometries of the QM region. As basis sets in QM calculations, LANL2DZ is used for Ca and Mn and 6-31G(d) for other atoms. The absence of vibrations with imaginary frequencies was checked to confirm the structure in an energy minimum. No scaling was adopted for the calculated frequencies.

4.3. Results

To assign the OH stretching vibrations of water molecules around the Mn cluster in the

Table 4.1 Calculated hydrogen bond distances (Å) of water molecules (between water oxygen and an acceptor atom) in comparison with the experimental distances in the X-ray structure

S state (oxidized Mn in S ₂)	calculation			experiment ^c
	S ₁ [Δd] ^b	S ₂ (Mn4)	S ₂ (Mn1)	S ₁
W1 _a -D61 ^a	2.63 [-0.06]	2.57	2.53	2.69
W1 _b -S169	2.99 [+0.16]	3.08	2.94	2.83
W2 _a -W5	2.79 [+0.03]	2.78	2.75	2.76
W2 _b -W8	2.68 [+0.05]	2.66	2.60	2.63
W3 _a -W7	2.80 [-0.12]	2.75	2.76	2.92
W3 _b -W5	2.73 [-0.19]	2.75	2.76	2.92
W4 _a -YZ	2.78 [-0.12]	2.75	2.74	2.90
W4 _b -Q165	2.72 [+0.06]	2.70	2.69	2.66
W5 _a -W6	2.68 [-0.02]	2.65	2.65	2.70
W5 _b -D170	3.19 [-0.14]	3.24	3.25	3.33
W6 _a -W7	2.83 [-0.10]	2.86	2.85	2.93
W6 _b -F182	2.99 [+0.15]	2.95	2.93	2.84
W7 _a -YZ	2.67 [+0.14]	2.65	2.65	2.53
W7 _b -E189	2.86 [-0.11]	2.94	2.93	2.97
W8 _a -Cl	3.29 [0.00]	3.22	3.21	3.29
W8 _b -N181	2.77 [-0.09]	2.76	2.70	2.86
W9 _a -D61	2.71 [+0.02]	2.74	2.73	2.69
W9 _b -W8	2.90 [0.00]	2.89	2.90	2.90
average	2.83 [-0.03]	2.83	2.81	2.86

^aSee Figure 4.1C for the numbering of water and its protons. ^bDifference from the experimental value. ^cAverage of the XFEL X-ray structures of four monomers in two dimers (PDB entries 4UB6 and 4UB8)

S₂/S₁ difference spectra, we performed normal mode analysis using the QM/MM method. The QM region includes the Mn cluster, Cl-1, and nine water molecules (W1–W9) together with surrounding amino acid residues. We assumed the oxidation states of the Mn atoms in the S₁ state as (Mn1, Mn2, Mn3, Mn4) = (III, IV, IV, III) following a widely accepted view,^{4, 24-28, 30-39} and protonation states of O5 and W2 as O²⁻ and H₂O, respectively.^{4, 24, 25} Calculations were performed on the basis of the X-ray structure by XFEL at 1.95 Å resolution (PDB entry 4UB6).⁶ The heavy

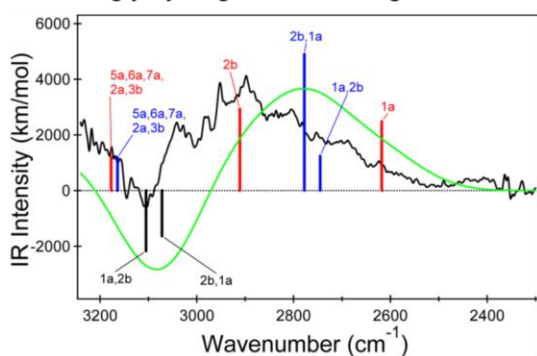
Table 4.2 Frequencies (cm^{-1}) and assignments of the OH stretching vibrations of water molecules around the Mn cluster estimated by QM/MM calculations

S ₁			S ₂ (Mn4 = IV)			S ₂ (Mn1 = IV)		
assignment ^c	frequency (IR intensity) ^b	assignment ^c	frequency (IR intensity) ^b	assignment ^c	frequency (IR intensity) ^b	assignment ^c	frequency (IR intensity) ^b	assignment ^c
W6 _{a,b}	3715 (322)	W6 _{a,b} , W7 _b	3685 (640)	W6 _{a,b} , W7 _b , W5 _b	3685 (574)	W6 _{a,b} , W7 _b , W5 _b	3685 (574)	W6 _{a,b} , W7 _b , W5 _b
W1 _b	3706 (483)	W5 _b	3677 (259)	W5 _b	3681 (311)	W5 _b	3681 (311)	W5 _b
W5 _b , W3 _b , W2 _a	3679 (190)	W1 _a	3638 (693)	W1 _a	3648 (896)	W7 _b , W1 _b , W6 _b	3648 (896)	W7 _b , W1 _b , W6 _b
W8 _a , W9 _b	3648 (207)	W7 _b , W6 _{a,b} , W3 _a	3634 (470)	W7 _b , W6 _{a,b} , W3 _a	3647 (271)	W9 _b	3647 (271)	W9 _b
W9 _b , W8 _a	3623 (224)	W9 _b , W8 _a	3628 (308)	W9 _b , W8 _a	3647 (342)	W1 _b , W7 _b , W9 _b	3647 (342)	W1 _b , W7 _b , W9 _b
W7 _b , W3 _a , W6 _b , W4 _a	3592 (523)	W6 _{a,b} , W7 _{a,b}	3581 (205)	W6 _{a,b} , W7 _{a,b}	3582 (302)	W6 _{a,b}	3582 (302)	W6 _{a,b}
W7 _{a,b} , W2 _{a,b} , W4 _b , W6 _{a,b}	3590 (629)	W8 _a , W9 _b	3549 (330)	W8 _a , W9 _b	3565 (318)	W8 _a	3565 (318)	W8 _a
W4 _a , W7 _a , W3 _{a,b} , W6 _a	3578 (959)	W3 _b , W4 _{a,b} , W2 _a	3504 (995)	W3 _b , W4 _{a,b} , W2 _a	3505 (875)	W3 _b , W2 _{a,b} , W4 _a	3505 (875)	W3 _b , W2 _{a,b} , W4 _a
W3 _b , W2 _a , W5 _{a,b} , W6 _{a,b} , W7 _b	3542 (627)	W4 _{a,b} , W3 _b	3498 (548)	W4 _{a,b} , W3 _b	3492 (563)	W4 _a	3492 (563)	W4 _a
W6 _a , W7 _b	3534 (509)	W3 _{a,b} , W7 _{a,b} , W6 _a	3427 (862)	W3 _{a,b} , W7 _{a,b} , W6 _a	3437 (769)	W3 _{a,b} , W7 _a	3437 (769)	W3 _{a,b} , W7 _a
W3 _{a,b} , W7 _{a,b} , W4 _{a,b} , W6 _{a,b} , W2 _a	3505 (359)	W2 _{a,b} , W3 _b	3410 (507)	W2 _{a,b} , W3 _b	3401 (689)	W2 _{a,b} , W3 _b	3401 (689)	W2 _{a,b} , W3 _b
W2 _{a,b} , W3 _b , W4 _b	3477 (289)	W4 _b	3392 (940)	W4 _b	3387 (697)	W4 _b	3387 (697)	W4 _b
W4 _b , W3 _b , W2 _a	3468 (1081)	W9 _a	3383 (429)	W9 _a	3364 (647)	W9 _a	3364 (647)	W9 _a
W8 _b	3397 (456)	W8 _b	3323 (1180)	W8 _b	3289 (1029)	W7 _a , W3 _{a,b} , W4 _a	3289 (1029)	W7 _a , W3 _{a,b} , W4 _a
W7 _a , W3 _a	3390 (741)	W7 _a , W3 _{a,b} , W4 _a	3288 (1026)	W7 _a , W3 _{a,b} , W4 _a	3257 (1527)	W8 _b	3257 (1527)	W8 _b
W9 _a	3310 (849)	W5 _a , W6 _{a,b} , W7 _a , W2 _a , W3 _b	3177 (1203)	W5 _a , W6 _{a,b} , W7 _a , W2 _a , W3 _b	3164 (1192)	W5 _a , W6 _{a,b} , W7 _a , W2 _a , W3 _b	3164 (1192)	W5 _a , W6 _{a,b} , W7 _a , W2 _a , W3 _b
W5 _a , W3 _b , W6 _{a,b} , W2 _a	3246 (978)	W2 _b	2911 (2940)	W2 _b	2778 (4903)	W2 _b , W1 _a	2778 (4903)	W2 _b , W1 _a
W1 _a , W2 _b	3105 (2167)	W1 _a	2618 (2485)	W1 _a	2745 (1244)	W1 _a , W2 _b	2745 (1244)	W1 _a , W2 _b
W2 _b , W1 _a	3072 (1631)							

^cSee Figure 4.1C for the numbering of water and its protons. ^bCalculated IR intensity (km/mol)

atoms (C, O, N, S, and Cl) of the MM regions were fixed to the coordinates of these original structures, while the structure of the QM region was optimized. The hydrogen bond structure of water molecules in the optimized geometry in the S_1 state is shown in Figure 4.1. A linear hydrogen bond chain is formed from D2-K317 and D1-D61 near Cl-1 to Y_z through W9, W8, W2, W5, W6, and W7, while a cyclic water cluster is formed by W3 and W5–W7. W1 and W4 are not directly involved in this water network but directly hydrogen-bonded to D1-D61 and Y_z , respectively. The average value of hydrogen bond distances of water molecules was 2.83 Å (Table 4.1), in good agreement with the experimental one (2.86 Å). Hydrogen bond distances between the oxygen atoms of W1 and D61, W2 and W8, W5 and W6, and W7 and Y_z , which were calculated to be 2.63, 2.68, 2.68, and 2.67 Å, respectively, were significantly shorter than other

A. strongly hydrogen-bonded region



B. weakly hydrogen-bonded region

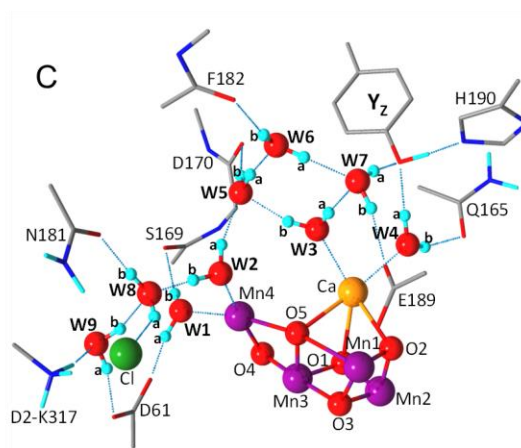
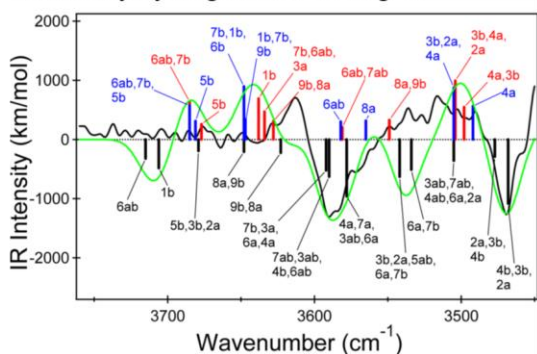


Figure 4.1 OH stretching vibrations of water molecules around the Mn cluster estimated by QM/MM calculation, superimposed on an experimental S_2/S_1 difference spectrum (black curve): (A) strongly hydrogen-bonded region and (B) weakly hydrogen-bonded region. Black negative bars are for the S_1 state; red and blue positive bars are for the S_2 state with Mn4(IV) and Mn1(IV), respectively. A simulated S_2/S_1 difference spectrum (green curves) was obtained assuming Gaussian bands with widths (fwhm) of 200 and 20 cm^{-1} for (A) strongly and (B) weakly hydrogen-bonded OH vibrations, respectively, and a thermal equilibrium of the two S_2 forms. The experimental spectrum of control Ca^{2+} -PSII is identical to the spectrum shown in ref 60. (C) the numbering of water and its protons in assignments of the QM/MM calculations.

hydrogen bonds.

The optimized geometry of the S_2 state was calculated by oxidation of one Mn atom in the S_1 model. It has been shown that two forms of the Mn cluster are stably optimized: an open cubane form with Mn4(IV) and a closed cubane form with Mn1(IV).^{31, 33, 35, 38, 39} Our calculation also provided two forms of the S_2 state with Mn4(IV) and Mn1(IV). The hydrogen bond patterns of water molecules were unchanged by the $S_1 \rightarrow S_2$ transition in both S_2 forms (Table 4.1). Some of the hydrogen bonds such as W1–D61, W3–W7, W4–Y_Z, W5–W6, and W8–Cl bonds were shortened by S_2 formation.

Normal mode analysis was performed for the optimized structures in the S_1 and S_2 states. Normal modes with large contributions of water OH vibrations obtained in the calculation are listed in Table 4.2 and are depicted in Figure 4.1, superimposing the control S_2/S_1 FTIR difference spectrum of Ca²⁺-PSII. It is shown that the OH stretching vibrations of water molecules exhibited frequencies between 3720 and 2600 cm⁻¹, overlapping the weakly hydrogen-bonded water OH bands in a higher-frequency region (Figure 4.1B) and the broad feature of a hydrogen bond network in a lower-frequency region (Figure 4.1A) in the S_2/S_1 difference spectrum. Many modes are significantly delocalized over several water molecules, and lower-frequency vibrations generally have higher intensities (Table 4.2) because of stronger hydrogen bonds.⁴³ Also, the frequencies and intensities of individual modes are rather different between the S_1 (Figure 4.1, negative black bars) and S_2 (red and blue bars) states, and even between the two S_2 forms with Mn4(IV) (red bars) and Mn1(IV) (blue bars). Using the obtained vibrations, S_2/S_1 difference spectra were simulated assuming Gaussian bands with 20 and 200 cm⁻¹ widths (fwhm) for modes in the weakly and strongly hydrogen-bonded OH regions, respectively, and equal populations of the two S_2 forms due to a thermal equilibrium (Figure 4.1, green curve). These bandwidths were

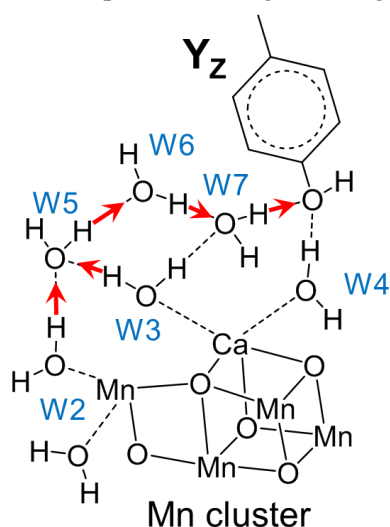


Figure 4.2 Directions of the displacement vectors of the in-phase coupled vibrations of a water network involving W5, W6, W7, W2, and W3.

selected to reproduce the experimental spectrum based on the general tendency that a stronger hydrogen bond significantly broadens the width of a OH band concomitant with a downshifted frequency.^{43, 44} It is noted that in normal mode analysis, normal mode vibrations are estimated only for the optimized geometry, and hence, the effects of thermal fluctuations at room temperature are involved in the assumed bandwidths. In the strongly hydrogen-bonded region of 3200–2400 cm⁻¹, a positive broad feature on the lower-frequency side was reproduced well, although the band center was slightly lower than the experimental one (Figure 4.1A). The lowest-frequency modes of the S₂ forms with Mn4(IV) and Mn1(IV) at 2618 and 2745 cm⁻¹, respectively, arise from the W1a proton (see Figure 4.1C for the numbering of protons) hydrogen-bonded with D1-D61, which has a short hydrogen bond distance of 2.53–2.57 Å (Table 4.1). The second lowest-frequency modes at 2911 cm⁻¹ [S₂ with Mn4(IV)] and 2778 cm⁻¹ [S₂ with Mn1(IV)] are due mainly to the W2b vibration. Intriguing modes in the low-frequency region are those at 3177 cm⁻¹ [S₂ with Mn4(IV)] and 3164 cm⁻¹ [S₂ with Mn1(IV)] arising from the coupled vibrations of W5a, W6a, W7a, W2a, and W3b with the largest contribution of W5a forming a strong hydrogen bond with W6 (the hydrogen bond distance is 2.65 Å). This mode shows an in-phase motion from water ligands, W2 and W3, to W7 hydrogen-bonded with Y_Z through a water network (directions of the displacement vectors are depicted in Figure 4.2). A similar type of coupled vibration of water molecules with a relatively lower frequency was also identified in a water wire in bacteriorhodopsin.⁴⁵

In the weakly hydrogen-bonded region of 3750–3500 cm⁻¹ (Figure 4.1B), simulated bands (green curve) at 3642(+), 3587(-), 3500(+), and 3469(-) cm⁻¹ seem to correspond to the experimental bands at 3613(+), 3590(-), ~3517(+), and 3469(-) cm⁻¹, respectively. Most of the modes result from significant couplings with several vibrations, which mainly arise from the OH groups hydrogen-bonded with amino acid residues or Cl⁻.

4.4. Discussion

Assignments of the OH Vibrations of Water Molecules around the Mn Cluster. The hydrogen bond structures (Figure 4.1C and Table 4.1) and the OH vibrations of water molecules (Table 4.2 and Figure 4.1A,B) around the Mn cluster were calculated for the S₁ state and the two forms of the S₂ state [an open cubane form with Mn4(IV) and a closed cubane form with Mn1(IV)] using the QM/MM method based on the X-ray structure by XFEL at 1.95 Å resolution.⁶ The calculated OH vibrations of water were found in a wide frequency range between 3720 and 2600 cm⁻¹ (Table 4.2), reflecting significantly scattered hydrogen bond distances between 3.29 and 2.53 Å in the water network (Table 4.1). Most of the water OH vibrations are coupled among several water molecules in the network (Table 4.2).

Recently, Yang et al.²⁵ also performed normal mode analysis of water molecules in the

S₂ state using QM/MM calculations based on the 1.9 Å structure by synchrotron radiation.³ Although the resultant hydrogen bond pattern of water molecules was similar to ours, the obtained OH frequencies and the vibrational modes were significantly different from those listed in Table 4.2. The calculated frequencies were found between 3752 and 3150 cm⁻¹, and OH modes with frequencies lower than 3000 cm⁻¹ were not obtained. This discrepancy between the results of ref 44 and our study could arise from the following differences in calculations. (1) The difference in the X-ray structure used for calculations. We used a damage-free structure by XFEL⁶ in contrast to a structure partially damaged by a strong dose of X-ray radiation³ used in ref 44. Because the coordinates of heavy atoms other than hydrogen atoms in the MM region were directly adopted from the X-ray structures without optimization, the difference in the X-ray structure could result in slightly different optimized structures of the QM region. (2) The difference in the QM region for geometry optimization. Although the geometry-optimized QM region in ref 44 included more amino acid residues than our study, the main chain amide of D1-F182 that interacts with W6 was not included, whereas all the amino acid residues and main chain amides interacting with W1–W9 were included in our QM region. The difference in the QM region, especially the absence of a residue that directly interacts with a water molecule, could change the hydrogen bond interactions of the water network. (3) The difference in the region used for the normal mode calculation. The authors of ref 44 abstracted a narrower part from the QM region for vibrational analysis by excluding most of the amino acid residues directly interacting water molecules as well as a Cl⁻ ion, whereas we used the whole QM region involving all the amino acid residues around the water molecules and the Cl⁻ ion. Indeed, when we performed normal mode analysis using a narrower part identical to that in ref 44 abstracted from our optimized QM structure, the frequencies were largely shifted from the original ones in Table 4.1; for example, the vibrations at 2618, 2911, and 3177 cm⁻¹ in the lower-frequency region shifted by -18, +139, and +38 cm⁻¹ to 2590, 3050, and 3215 cm⁻¹, respectively. However, the thus calculated frequencies did not reproduce the frequencies reported in ref 44. Thus, although a sufficiently large region for normal mode calculation must be important for obtaining correct vibrational frequencies, the exact reason for the discrepancy between the two studies is unknown at present.

The calculated OH frequencies well overlap the regions of water and hydrogen bond networks in the experimental S₂/S₁ FTIR difference spectrum (Figure 4.1), involving a weakly hydrogen-bonded OH region of water in the range of 3700–3500 cm⁻¹ and a lower-frequency region with a broad positive feature in the range of 3200–2500 cm⁻¹.⁴⁶⁻⁵³ In particular, the latter broad feature, which has been assigned to the vibrations of polarizable protons in hydrogen bond networks,⁴⁷ was sufficiently reproduced in the calculation (Figure 4.1A). The optimized geometry (Table 4.1) showed that this positive feature is caused by the strengthened hydrogen bonds of some water OH groups such as W1a and W2b (Figure 4.1C) upon S₂ formation, shifting their OH

vibrations to lower frequencies. The stronger hydrogen bonds are probably caused by accumulation of an excess positive charge on the Mn cluster in the S_2 state, increasing the polarity of the ligands and the environment. The lowest-frequency mode in the S_2 state arises from the hydrogen bond of W1a with D1-D61 [2618 and 2745 cm^{-1} in the S_2 forms with Mn4(IV) and Mn1(IV), respectively (Table 4.2 and Figure 4.1)]. W2b hydrogen bonded with W8 (2911 and 2778 cm^{-1}) and the in-phase coupled vibration of W5a, W6a, W7a, W2a, and W3b (3177 and 3164 cm^{-1}) also showed relatively low frequencies (Figure 4.1A).

Role of the Water Network in the Water Oxidation Mechanism. In the water oxidation mechanism, proton release takes place in the $S_0 \rightarrow S_1$, $S_2 \rightarrow S_3$, and $S_3 \rightarrow S_0$ transitions.⁷⁻⁹ For efficient proton release, proton transfer pathways by hydrogen bond networks involving water molecules must be formed in proteins. In particular, polarizable protons in water chains play an important role in rapid proton transfer using the Grotthuss mechanism.^{44, 54} Several water channels were found around the Mn cluster, leading to the luminal side.^{3, 16-23} Among them, many authors suggested that the hydrogen bond network starting from D1-D61 through protonatable residues near Cl-1 is effective for proton transfer.^{20, 22, 23, 27, 55-59} In this pathway, the OH stretching vibration of W1a forming a strong hydrogen bond directly with D1-D61 (Figure 4.1C), which was calculated at 2750–2610 cm^{-1} in the S_2 state and probably contributes to the broad positive feature in the S_2/S_1 FTIR spectrum⁶⁰, should work in proton transfer from W1, a ligand to Mn4, to D1-D61. In addition, the vibration of W2b strongly hydrogen bonded with W8 (calculated at 2920–2700 cm^{-1} in the S_2 state), which may also be a constituent of the broad FTIR feature, can be effective for proton transfer from W2 to D1-D61 through W8 and W9 (Figure 4.1C). This proton pathway through D1-D61 may be functional at least in the $S_3 \rightarrow S_0$ transition, because mutations of D1-D61 significantly retarded the $S_3 \rightarrow S_0$ transition and reduced the efficiency of this transition.^{52, 55}

On the other hand, the channel near Y_Z has been proposed as another proton transfer or water access pathway.^{3, 12, 14, 17, 19, 21} We proposed a novel proton transfer mechanism via the Y_Z^\bullet radical in the S_2 and/or S_3 state, which requires proton release before electron transfer because of an excess positive charge on the Mn cluster (Chapter 2).¹⁴ Our QM/MM calculation showed that one water molecule near Y_Z moves closer to D1-H190 upon Y_Z^\bullet formation. It was suggested that hopping of a polarizable proton located between Y_Z^\bullet and D1-H190, which showed a broad feature around 2800 cm^{-1} in a Y_Z^\bullet/Y_Z FTIR spectrum, to this water triggers proton transfer from substrate water on the Mn cluster to the lumen.¹⁴ Alternatively, it might be possible that the first proton transfer takes place from W7 to W4, which is now connected with the hydrogen bond network to the lumen by the moved water molecule. In any case, in the mechanism of proton transfer through Y_Z or a nearby region, the in-phase coupled vibration of a water network involving W5a, W6a, W7a, W3a, and W2a (the directions of proton movements are shown in Figure 4.2), which was

calculated at 3180–3160 cm^{-1} (Table 4.2), may be effective in proton transfer from W2 and W3, candidates of substrate, to Y_Z . Using such a vibrational mode, rapid proton transfer from substrate to the Y_Z site will be possible by the Grotthuss mechanism immediately after or concerted with the trigger reaction of proton hopping from Y_Z -HisH⁺ or W7.

Theoretical studies suggested that in the $S_2 \rightarrow S_3$ transition a water molecule is inserted into Mn1 or Mn4 from bulk or possibly from W3, a water ligand to Ca.^{27, 28, 33, 35, 36, 38, 39, 61} This idea is consistent with the elongation of the Mn–Mn distance in the $S_2 \rightarrow S_3$ transition detected by EXAFS.^{62, 63} Previous FTIR studies also suggested the insertion of water into the WOC in the $S_2 \rightarrow S_3$ transition.^{48, 64, 65} If W3 on Ca moves to Mn1 or Mn4, the inserted water could bind to Ca to compensate for the position of W3. A proton could be released from W3 using the Y_Z pathway before its movement, which can also explain the decrease in activity caused by substitution with Sr²⁺ having a different Lewis acidity.⁶⁶ It is thus possible that the water network near Y_Z and Ca can be used for the concerted process of proton release and water insertion.

References

- [1] Joliot, P., Barbieri, G., and Chabaud, R. (1969) A new model of photochemical centers in system II, *Photochem. Photobiol* 10, 309-329.
- [2] Kok, B., Forbush, B., and McGloin, M. (1970) Cooperation of charges in photosynthetic O₂ evolution-I. A linear four step mechanism, *Photochem. Photobiol.* 11, 457-475.
- [3] Umena, Y., Kawakami, K., Shen, J. R., and Kamiya, N. (2011) Crystal structure of oxygen-evolving photosystem II at a resolution of 1.9 Å, *Nature* 473, 55-60.
- [4] Lubner, S., Rivalta, I., Umena, Y., Kawakami, K., Shen, J. R., Kamiya, N., Brudvig, G. W., and Batista, V. S. (2011) S₁-state model of the O₂-evolving complex of photosystem II, *Biochemistry* 50, 6308-6311.
- [5] Yano, J., Kern, J., Irrgang, K. D., Latimer, M. J., Bergmann, U., Glatzel, P., Pushkar, Y., Biesiadka, J., Loll, B., Sauer, K., Messinger, J., Zouni, A., and Yachandra, V. K. (2005) X-ray damage to the Mn₄Ca complex in single crystals of photosystem II: A case study for metalloprotein crystallography, *Proc. Natl. Acad. Sci. U.S.A.* 102, 12047-12052.
- [6] Suga, M., Akita, F., Hirata, K., Ueno, G., Murakami, H., Nakajima, Y., Shimizu, T., Yamashita, K., Yamamoto, M., Ago, H., and Shen, J. R. (2015) Native structure of photosystem II at 1.95 Å resolution viewed by femtosecond X-ray pulses, *Nature* 517, 99-103.
- [7] Fowler, C. F. (1977) Proton evolution from photosystem II. stoichiometry and mechanistic considerations, *Biochim. Biophys. Acta* 462, 414-421.
- [8] Schlodder, E., and Witt, H. T. (1999) Stoichiometry of proton release from the catalytic center in photosynthetic water oxidation. Reexamination by a glass electrode study at pH 5.5-7.2, *J. Biol. Chem.* 274, 30387-30392.

- [9] Suzuki, H., Sugiura, M., and Noguchi, T. (2009) Monitoring proton release during photosynthetic water oxidation in photosystem II by means of isotope-edited infrared spectroscopy, *J. Am. Chem. Soc.* *131*, 7849-7857.
- [10] Rappaport, F., Blanchard-Desce, M., and Lavergne, J. (1994) Kinetics of electron transfer and electrochromic change during the redox transitions of the photosynthetic oxygen-evolving complex, *Biochim. Biophys. Acta* *1184*, 178-192.
- [11] Haumann, M., Liebisch, P., Muller, C., Barra, M., Grabolle, M., and Dau, H. (2005) Photosynthetic O₂ formation tracked by time-resolved X-ray experiments, *Science* *310*, 1019-1021.
- [12] Klauss, A., Haumann, M., and Dau, H. (2012) Alternating electron and proton transfer steps in photosynthetic water oxidation, *Proc. Natl. Acad. Sci. U.S.A.* *109*, 16035-16040.
- [13] Noguchi, T., Suzuki, H., Tsuno, M., Sugiura, M., and Kato, C. (2012) Time-resolved infrared detection of the proton and protein dynamics during photosynthetic oxygen evolution, *Biochemistry* *51*, 3205-3214.
- [14] Nakamura, S., Nagao, R., Takahashi, R., and Noguchi, T. (2014) Fourier transform infrared detection of a polarizable proton trapped between photooxidized tyrosine Y_Z and a coupled histidine in photosystem II: Relevance to the proton transfer mechanism of water oxidation, *Biochemistry* *53*, 3131-3144.
- [15] Klauss, A., Haumann, M., and Dau, H. (2015) Seven steps of alternating electron and proton transfer in photosystem II water oxidation traced by time-resolved photothermal beam deflection at improved sensitivity, *J. Phys. Chem. B* *119*, 2677-2689.
- [16] Murray, J. W., and Barber, J. (2007) Structural characteristics of channels and pathways in photosystem II including the identification of an oxygen channel, *J. Struct. Biol.* *159*, 228-237.
- [17] Ho, F. M., and Styring, S. (2008) Access channels and methanol binding site to the CaMn₄ cluster in Photosystem II based on solvent accessibility simulations, with implications for substrate water access, *Biochim. Biophys. Acta* *1777*, 140-153.
- [18] Vassiliev, S., Comte, P., Mahboob, A., and Bruce, D. (2010) Tracking the flow of water through photosystem II using molecular dynamics and streamline tracing, *Biochemistry* *49*, 1873-1881.
- [19] Bondar, A. N., and Dau, H. (2012) Extended protein/water H-bond networks in photosynthetic water oxidation, *Biochim. Biophys. Acta* *1817*, 1177-1190.
- [20] Bao, H., Dilbeck, P. L., and Burnap, R. L. (2013) Proton transport facilitating water-oxidation: the role of second sphere ligands surrounding the catalytic metal cluster, *Photosynth. Res.* *116*, 215-229.
- [21] Ogata, K., Yuki, T., Hatakeyama, M., Uchida, W., and Nakamura, S. (2013) All-atom

- molecular dynamics simulation of photosystem II embedded in thylakoid membrane, *J. Am. Chem. Soc.* *135*, 15670-15673.
- [22] Linke, K., and Ho, F. M. (2014) Water in Photosystem II: Structural, functional and mechanistic considerations, *Biochim. Biophys. Acta* *1837*, 14-32.
- [23] Vogt, L., Vinyard, D. J., Khan, S., and Brudvig, G. W. (2015) Oxygen-evolving complex of Photosystem II: an analysis of second-shell residues and hydrogen-bonding networks, *Curr. Opin. Chem. Biol.* *25*, 152-158.
- [24] Saito, K., and Ishikita, H. (2014) Influence of the Ca²⁺ ion on the Mn₄Ca conformation and the H-bond network arrangement in Photosystem II, *Biochim. Biophys. Acta* *1837*, 159-166.
- [25] Yang, J., Hatakeyama, M., Ogata, K., Nakamura, S., and Li, C. (2014) Theoretical study on the role of Ca²⁺ at the S₂ state in photosystem II, *J. Phys. Chem. B* *118*, 14215-14222.
- [26] Siegbahn, P. E. (2014) Water oxidation energy diagrams for photosystem II for different protonation states, and the effect of removing calcium, *Phys. Chem. Chem. Phys.* *16*, 11893-11900.
- [27] Siegbahn, P. E. M. (2012) Mechanisms for proton release during water oxidation in the S₂ to S₃ and S₃ to S₄ transitions in photosystem II, *PCCP* *14*, 4849-4856.
- [28] Siegbahn, P. E. (2013) Water oxidation mechanism in photosystem II, including oxidations, proton release pathways, O-O bond formation and O₂ release, *Biochim. Biophys. Acta* *1827*, 1003-1019.
- [29] Sproviero, E. M., Gascon, J. A., McEvoy, J. P., Brudvig, G. W., and Batista, V. S. (2008) Quantum mechanics/molecular mechanics study of the catalytic cycle of water splitting in photosystem II, *J. Am. Chem. Soc.* *130*, 3428-3442.
- [30] Vogt, L., Ertem, M. Z., Pal, R., Brudvig, G. W., and Batista, V. S. (2015) Computational insights on crystal structures of the oxygen-evolving complex of photosystem II with either Ca²⁺ or Ca²⁺ substituted by Sr²⁺, *Biochemistry* *54*, 820-825.
- [31] Pantazis, D. A., Ames, W., Cox, N., Lubitz, W., and Neese, F. (2012) Two interconvertible structures that explain the spectroscopic properties of the oxygen-evolving complex of photosystem II in the S₂ state, *Angew. Chem. Int. Ed.* *51*, 9935-9940.
- [32] Ames, W., Pantazis, D. A., Krewald, V., Cox, N., Messinger, J., Lubitz, W., and Neese, F. (2011) Theoretical evaluation of structural models of the S₂ state in the oxygen evolving complex of Photosystem II: protonation states and magnetic interactions, *J. Am. Chem. Soc.* *133*, 19743-19757.
- [33] Cox, N., Retegan, M., Neese, F., Pantazis, D. A., Boussac, A., and Lubitz, W. (2014) Electronic structure of the oxygen-evolving complex in photosystem II prior to O-O bond formation, *Science* *345*, 804-808.
- [34] Galstyan, A., Robertazzi, A., and Knapp, E. W. (2012) Oxygen-evolving Mn cluster in

- photosystem II: The protonation pattern and oxidation state in the high-resolution crystal structure, *J. Am. Chem. Soc.* *134*, 7442-7449.
- [35] Isobe, H., Shoji, M., Yamanaka, S., Umena, Y., Kawakami, K., Kamiya, N., Shen, J. R., and Yamaguchi, K. (2012) Theoretical illumination of water-inserted structures of the CaMn_4O_5 cluster in the S_2 and S_3 states of oxygen-evolving complex of photosystem II: Full geometry optimizations by B3LYP hybrid density functional, *Dalton Trans.* *41*, 13727-13740.
- [36] Isobe, H., Shoji, M., Yamanaka, S., Mino, H., Umena, Y., Kawakami, K., Kamiya, N., Shen, J. R., and Yamaguchi, K. (2014) Generalized approximate spin projection calculations of effective exchange integrals of the CaMn_4O_5 cluster in the S_1 and S_3 states of the oxygen evolving complex of photosystem II, *Phys. Chem. Chem. Phys.* *16*, 11911-11923.
- [37] Shoji, M., Isobe, H., Yamanaka, S., Umena, Y., Kawakami, K., Kamiya, N., Shen, J.-R., and Yamaguchi, K. (2013) Theoretical insight in to hydrogen-bonding networks and proton wire for the CaMn_4O_5 cluster of photosystem II. Elongation of Mn–Mn distances with hydrogen bonds, *Catal. Sci. Technol.* *3*, 1831-1848.
- [38] Shoji, M., Isobe, H., and Yamaguchi, K. (2015) QM/MM study of the S_2 to S_3 transition reaction in the oxygen-evolving complex of photosystem II, *Chem. Phys. Lett.* *636*, 172-179.
- [39] Bovi, D., Narzi, D., and Guidoni, L. (2013) The S_2 state of the oxygen-evolving complex of photosystem II explored by QM/MM dynamics: spin surfaces and metastable states suggest a reaction path towards the S_3 state, *Angew. Chem. Int. Ed. Engl.* *52*, 11744-11749.
- [40] Petrie, S., Pace, R. J., and Stranger, R. (2015) Resolving the differences between the 1.9 Å and 1.95 Å crystal structures of photosystem II: A single proton relocation defines two tautomeric forms of the water-oxidizing complex, *Angew. Chem. Int. Ed.* *54*, 7120-7124.
- [41] Frisch, M. J., Trucks, G. W., Schlegel, H. B., Scuseria, G. E., Robb, M. A., Cheeseman, J. R., Scalmani, G., Barone, V., Mennucci, B., Petersson, G. A., Nakatsuji, H., Caricato, M., Li, X., Hratchian, H. P., Izmaylov, A. F., Bloino, J., Zheng, G., Sonnenberg, J. L., Hada, M., Ehara, M., Toyota, K., Fukuda, R., Hasegawa, J., Ishida, M., Nakajima, T., Honda, Y., Kitao, O., Nakai, H., Vreven, T., Montgomery, J. A., Jr., Peralta, J. E., Ogliaro, F., Bearpark, M., Heyd, J. J., Brothers, E., Kudin, K. N., Staroverov, V. N., Kobayashi, R., Normand, J., Raghavachari, K., Rendell, A., Burant, J. C., Iyengar, S. S., Tomasi, J., Cossi, M., Rega, N., Millam, J. M., Klene, M., Knox, J. E., Cross, J. B., Bakken, V., Adamo, C., Jaramillo, J., Gomperts, R., Stratmann, R. E., Yazyev, O., Austin, A. J., Cammi, R., Pomelli, C., Ochterski, J. W., Martin, R. L., Morokuma, K., Zakrzewski, V. G., Voth, G. A., Salvador, P., Dannenberg, J. J., Dapprich, S., Daniels, A. D., Farkas, O., Foresman, J. B., Ortiz, J. V., Cioslowski, J., and Fox, D. J. (2009) *Gaussian 09*, revision C.01, *Gaussian Inc., Wallingford CT*.
- [42] Vreven, T., Byun, K. S., Komaromi, I., Dapprich, S., Montgomery, J. A., Morokuma, K., and Frisch, M. J. (2006) Combining quantum mechanics methods with molecular mechanics

- methods in ONIOM, *J. Chem. Theory Comput.* **2**, 815-826.
- [43] Huggins, C. M., and Pimentel, G. C. (1956) Systematics of the infrared spectral properties of hydrogen bonding systems: Frequency shift, half width and intensity, *J. Phys. Chem.* **60**, 1615-1619.
- [44] Zundel, G. (2000) Hydrogen bonds with large proton polarizability and proton transfer processes in electrochemistry and biology, *Adv. Chem. Phys.* **111**, 1-217.
- [45] Wolf, S., Freier, E., Cui, Q., and Gerwert, K. (2014) Infrared spectral marker bands characterizing a transient water wire inside a hydrophobic membrane protein, *J. Chem. Phys.* **141**, 22D524.
- [46] Noguchi, T., and Sugiura, M. (2000) Structure of an active water molecule in the water-oxidizing complex of photosystem II as studied by FTIR spectroscopy, *Biochemistry* **39**, 10943-10949.
- [47] Noguchi, T., and Sugiura, M. (2002) FTIR detection of water reactions during the flash-induced S-state cycle of the photosynthetic water-oxidizing complex, *Biochemistry* **41**, 15706-15712.
- [48] Suzuki, H., Sugiura, M., and Noguchi, T. (2008) Monitoring water reactions during the S-state cycle of the photosynthetic water-oxidizing center: Detection of the DOD bending vibrations by means of Fourier transform infrared spectroscopy, *Biochemistry* **47**, 11024-11030.
- [49] Shimada, Y., Suzuki, H., Tsuchiya, T., Tomo, T., Noguchi, T., and Mimuro, M. (2009) Effect of a single-amino acid substitution of the 43 kDa chlorophyll protein on the oxygen-evolving reaction of the cyanobacterium *Synechocystis* sp. PCC 6803: Analysis of the Glu354Gln mutation, *Biochemistry* **48**, 6095-6103.
- [50] Hou, L. H., Wu, C. M., Huang, H. H., and Chu, H. A. (2011) Effects of ammonia on the structure of the oxygen-evolving complex in photosystem II as revealed by light-induced FTIR difference spectroscopy, *Biochemistry* **50**, 9248-9254.
- [51] Service, R. J., Yano, J., Dilbeck, P. L., Burnap, R. L., Hillier, W., and Debus, R. J. (2013) Participation of glutamate-333 of the D1 polypeptide in the ligation of the Mn₄CaO₅ cluster in photosystem II, *Biochemistry* **52**, 8452-8464.
- [52] Debus, R. J. (2014) Evidence from FTIR difference spectroscopy that D1-Asp61 influences the water reactions of the oxygen-evolving Mn₄CaO₅ cluster of photosystem II, *Biochemistry* **53**, 2941-2955.
- [53] Pokhrel, R., Debus, R. J., and Brudvig, G. W. (2015) Probing the effect of mutations of asparagine 181 in the D1 subunit of photosystem II, *Biochemistry* **54**, 1663-1672.
- [54] de Grotthuss, C. J. T. (1806) Sur la décomposition de l'eau et des corps qu'elle tient en dissolution à l'aide de l'électricité galvanique, *Ann. Chim.* **58**, 54-74.

- [55] Dilbeck, P. L., Hwang, H. J., Zaharieva, I., Gerencser, L., Dau, H., and Burnap, R. L. (2012) The D1-D61N mutation in *Synechocystis sp.* PCC 6803 allows the observation of pH-sensitive intermediates in the formation and release of O₂ from photosystem II, *Biochemistry* 51, 1079-1091.
- [56] Amin, M., Vogt, L., Szejgis, W., Vassiliev, S., Brudvig, G. W., Bruce, D., and Gunner, M. R. (2015) Proton-coupled electron transfer during the S-state transitions of the oxygen-evolving complex of photosystem II, *J. Phys. Chem. B* 119, 7366-7377.
- [57] Rivalta, I., Amin, M., Lubner, S., Vassiliev, S., Pokhrel, R., Umena, Y., Kawakami, K., Shen, J. R., Kamiya, N., Bruce, D., Brudvig, G. W., Gunner, M. R., and Batista, V. S. (2011) Structural-functional role of chloride in photosystem II, *Biochemistry* 50, 6312-6315.
- [58] Pokhrel, R., Service, R. J., Debus, R. J., and Brudvig, G. W. (2013) Mutation of lysine 317 in the D2 subunit of photosystem II alters chloride binding and proton transport, *Biochemistry* 52, 4758-4773.
- [59] Suzuki, H., Yu, J. F., Kobayashi, T., Nakanishi, H., Nixon, P. J., and Noguchi, T. (2013) Functional roles of D2-Lys317 and the interacting chloride ion in the water oxidation reaction of photosystem II as revealed by Fourier transform infrared analysis, *Biochemistry* 52, 4748-4757.
- [60] Nakamura, S., Ota, K., Shibuya, Y., and Noguchi, T. (2016) Role of a water network around the Mn₄CaO₅ cluster in photosynthetic water oxidation: A Fourier transform infrared spectroscopy and quantum mechanics/molecular mechanics calculation study, *Biochemistry* 55, 597-607.
- [61] Cox, N., and Messinger, J. (2013) Reflections on substrate water and dioxygen formation, *Biochim. Biophys. Acta* 1827, 1020-1030.
- [62] Yano, J., and Yachandra, V. (2014) Mn₄Ca cluster in photosynthesis: Where and how water is oxidized to dioxygen, *Chem. Rev.* 114, 4175-4205.
- [63] Pushkar, Y., Yano, J., Sauer, K., Boussac, A., and Yachandra, V. K. (2008) Structural changes in the Mn₄Ca cluster and the mechanism of photosynthetic water splitting, *Proc. Natl. Acad. Sci. U. S. A.* 105, 1879-1884.
- [64] Noguchi, T. (2008) FTIR detection of water reactions in the oxygen-evolving centre of photosystem II, *Philos. Trans. R. Soc.* 363, 1189-1194.
- [65] Noguchi, T., and Sugiura, M. (2002) Flash-induced FTIR difference spectra of the water oxidizing complex in moderately hydrated photosystem II core films: Effect of hydration extent on Sstate transitions, *Biochemistry* 41, 2322-2330.
- [66] Vrettos, J. S., Stone, D. A., and Brudvig, G. W. (2001) Quantifying the ion selectivity of the Ca²⁺ site in photosystem II: evidence for direct involvement of Ca²⁺ in O₂ formation, *Biochemistry* 40, 7937-7945.

Vibrational analysis of carboxylate ligands in the water oxidizing center

5.1. Introduction

The catalytic site of water oxidation is a water-oxidizing center (WOC) located in the electron-donor side of PSII.¹⁻³ Recent high-resolution (1.9–1.95 Å) X-ray crystallographic structures of PSII^{4, 5} revealed that the WOC core is an Mn cluster fixed to the protein by six carboxylate [D1-D170, D1-E189, D1-E333, D1-D342, D1-A344 (C terminus), and CP43-E354] ligands and one imidazole (D1-H332) ligand. Four water ligands are also bound to Mn4 (W1 and W2) and Ca (W3 and W4) (Figure 5.1 shows numbering of the Mn ions and water ligands). Because of the absence of the information of hydrogen atoms in the X-ray structures, the protonation states of the water and oxo ligands in Mn as well as the structure of the hydrogen bond network remain to be clarified.

The water-oxidizing reaction proceeds through a cycle of five intermediates designated as S_n states ($n = 0-4$),^{6, 7} where S_1 is the most stable in the dark. Oxidation of the Mn cluster by a

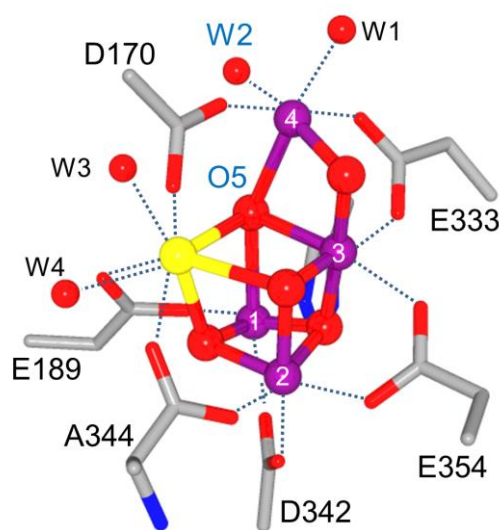


Figure 5.1 Carboxylate groups and water ligands around the Mn cluster with numbering of Mn and oxygen atoms.

Y_Z^\bullet radical, produced by light-induced charge separation, advances the S_n state ($n = 0-3$) to the S_{n+1} state. The S_4 state immediately relaxes to the S_0 state on release of O_2 . The oxidation states of the Mn atoms within the cluster have long been a source of debate, especially around whether the cluster exists in a high-oxidation $[Mn(III)_2Mn(IV)_2]$ or low-oxidation $[Mn(III)_4$ or $Mn(II)Mn(III)_2Mn(IV)]$ state in S_1 .⁸⁻¹²

With the information of atomic coordinates from high-resolution X-ray structures of the WOC, quantum chemical calculation is now a very powerful method in investigation of the water oxidation mechanism^{10, 12-24}. Calculations using the density functional theory (DFT) and quantum mechanics/molecular mechanics (QM/MM) methods can be used to predict individual S-state structures and hence, the reaction scheme. Experimental data, such as EPR and extended X-ray absorption fine structure (EXAFS), as well as X-ray structural information were simulated using these methods to identify the protonation structure and the oxidation states,^{10, 13, 15, 20, 21} although a definite conclusion has not yet been reached.

In contrast to EPR and EXAFS, which provide information mainly about the core of the Mn cluster, FTIR spectroscopy provides structural information about the protein moiety and water molecules coupled to the Mn cluster.²⁵⁻²⁷ FTIR spectroscopy, which detects molecular vibrations, is highly sensitive to the structures and interactions of functional groups, and hence, the FTIR difference technique can detect subtle structural changes at a much finer structural resolution than X-ray crystallography. Flash-induced FTIR difference spectra taken during the S-state cycle exhibit many prominent signals in the protein region. In particular, characteristic features were observed around 1400 cm^{-1} in the region of the symmetric stretching vibrations of carboxylate groups.²⁸⁻³⁵ Such signals reflect significant changes in the interactions of carboxylate groups around the Mn cluster, implying that these carboxylate groups are deeply involved in the water oxidation mechanism. The observation that Ca^{2+} depletion drastically changed the spectral feature around 1400 cm^{-1} ^{28, 36} also supports this idea. Thus, analyzing the structural changes of carboxylate groups during the S-state cycle provides crucial information regarding the mechanism of this reaction. However, clear assignment of the FTIR bands to individual carboxylate groups has not been achieved, except for the C-terminal carboxylate of D1-Ala344, which has bands that

Table 5.1 Mn cluster models used for QM/MM calculations

Model	Oxidation state in S_1^a	W2	O5	Oxidized Mn in S_2
1	High (III, IV, IV, III)	H_2O	O^{2-}	Mn1 or Mn4
2	High (III, IV, IV, III)	OH^-	O^{2-}	Mn1 or Mn4
3	Low (III, III, III, III)	OH^-	H_2O	Mn2
4	Low (III, IV, III, II)	H_2O	OH^-	Mn4
5 (Ca depleted)	High (III, IV, IV, III)	H_2O	O^{2-}	Mn4

^aOxidation states of (Mn1, Mn2, Mn3, Mn4).

were assigned successfully by its selective labeling with [1-¹³C]Ala.^{31, 32}

In this study, the carboxylate stretching region of the FTIR difference spectra of the WOC was simulated using QM/MM calculations, which were based on a damage-free X-ray structure obtained using an X-ray free electron laser (XFEL).⁵ Several WOC models with different oxidation and protonation states (Table 5.1) were assumed to reproduce the experimental S₂/S₁ difference³⁰ and ¹²C/¹³C-Ala S₂/S₁ double-difference³¹ spectra. The S₂/S₁ difference spectrum of a Ca-depleted WOC²⁸ was also simulated. These FTIR spectra show subtle changes in bond lengths and interactions of carboxylate groups, thus providing a different way of evaluating the most accurate WOC model from previous simulations using EXAFS and EPR data.^{10, 13, 15, 20, 21} This QM/MM simulation provides sufficient reproduction of the FTIR spectra, showing the significance of carboxylate ligands in the water oxidation mechanism.

5.2. Materials and Methods

The initial coordinates of PSII models were obtained from the XFEL X-ray structure at a resolution of 1.95 Å⁵ (Protein Data Bank ID code 4UB6). In addition to the Mn cluster, amino acid residues, water molecules, and two Cl⁻ ions located within 20 Å from the Mn cluster were extracted from the X-ray structure. Hydrogen atoms were generated and optimized using the AMBER force field.³⁷ During this procedure, the positions of all heavy atoms were fixed. QM/MM calculations were performed using the two-layer ONIOM method³⁸ with the electronic embedding scheme within the Gaussian 09 program package.³⁹ The QM region consists of the Mn cluster, amino acid ligands (D1-D170, D1-E189, D1-E333, D1-D342, D1-A344, CP43-E354, and D1-H332), water ligands (W1, W2, W3, and W4), 11 other water molecules that surround the Mn cluster, Y_Z, D1-H190, D1-D61, D1-H337, and CP43- R357. Other atoms in the selected region were assigned to the molecular mechanics (MM) region. Geometry optimization and normal mode analysis of the QM region were performed using an unrestricted DFT method with the B3LYP functional using LANL2DZ and 6-31G(d) as basis sets for metal atoms and other atoms, respectively.²⁴ In QM/MM geometry optimization, the coordinates of the QM region were fully relaxed, whereas those of the MM region were fixed. Table 5.1 shows the oxidation and protonation states of calculated models. The oxidation states of (Mn1, Mn2, Mn3, Mn4) in the S₁ state are (III, IV, IV, III) in high-oxidation models and (III, III, III, III) or (III, IV, III, II) in lowoxidation models. Mn1 or Mn4 and Mn2 or Mn4 were oxidized on S₂ formation in the high- and low-oxidation models, respectively. High-spin states were assumed in the calculations. The protonation states of W2 and O5 were assumed to be H₂O, OH⁻, or O²⁻ following previous studies.^{10, 12-24}

To obtain IR spectra in the COO⁻ stretching region, normal modes involving carboxylate

vibrations were added by assuming a Gaussian band with a 16-cm^{-1} width (FWHM) for each mode. A scaling factor was determined for each simulated difference spectrum (for models 1 and 2, an average spectrum of Mn1- and Mn4-oxidized S_2) to adjust the frequency of the simulated major peak to that of the experimental one; this major peak includes the negative peak at 1401 cm^{-1} in the S_2/S_1 difference spectrum, the positive peak at 1320 cm^{-1} in the $^{12}\text{C}/^{13}\text{C}$ -Ala S_2/S_1 double-difference spectrum, and the positive peak at 1431 cm^{-1} in the S_2/S_1 difference spectrum of Ca-depleted PSII. Adopted scaling factors ranged from 0.955 to 0.966. When the corresponding peak was not found in a calculated spectrum, a scaling factor of 0.960 was adopted.

5.3. Results

The quantum mechanics (QM) region of the WOC (Figure 5.1) used in QM/MM calculations included six carboxylate ligands (D170, E189, E333, D342, E354, and A344; subunit names are omitted hereafter) and one nearby carboxylate group (D61) hydrogen bonded with W1. All of the amino acid groups and water molecules interacting with these carboxylate groups were included in the QM region to accurately reproduce carboxylate vibrations. Different protonation states at W2 and O5 as well as high- and low-oxidation states of the Mn ions were assumed in the constructed models (Table 5.1). Model 1 ($\text{W2/O5} = \text{H}_2\text{O/O}^{2-}$) and model 2 ($\text{W2/O5} = \text{OH}^-/\text{O}^{2-}$), both of which have high-oxidation states, have been used in many previous DFT and QM/MM studies,^{10, 14, 16, 18-20, 22} whereas model 3 ($\text{W2/O5} = \text{OH}^-/\text{H}_2\text{O}$) and model 4 ($\text{W2/O5} = \text{H}_2\text{O}/\text{OH}^-$) have low-oxidation states that previous DFT calculations suggested could fit to the 1.9- and 1.95-Å structures, respectively, revealed by X-ray crystallography.¹² A model of a Ca-depleted WOC with the same protonation and oxidation states as model 1 was also calculated (model 5). In the S_2 state, Mn1 or Mn4 was oxidized in the high-oxidation models, whereas Mn2 or Mn4 was oxidized in the low-oxidation models. The Mn1- and Mn4-oxidized S_2 states of the high-oxidation models have been proposed to reflect two conformations showing $g = 4.1$ and $g = 2$ multiline EPR signals, respectively, where the latter conformation has a slightly lower energy.^{10, 14, 17}

Models 1 and 2 showed relatively small deviations ($\text{rmsd} = 0.12\text{--}0.13\text{ \AA}$), whereas models 3 and 4 showed larger deviations ($\text{rmsd} = 0.25$ and 0.15 \AA , respectively). In particular, model 3 has very large deviations in Mn3-O5 and Mn4-O5 (0.93 and 0.86 \AA , respectively). The calculated distances of model 1 are very similar to those in previous QM/MM calculations.^{18, 19} A relatively large deviation of Mn3-O5 (-0.44 \AA) from the XFEL structure could be attributed to a minor contribution of the S_0 state as previously suggested.²⁰ IR spectra of the WOC were simulated within the symmetric COO^- stretching region at around 1400 cm^{-1} . This region does not overlap with other vibrational modes in contrast to a severe overlap of the strong amide II bands in the asymmetric COO^- region around 1550 cm^{-1} .²⁹ Simulated S_2/S_1 IR difference spectra of model 1 agreed well with the experimental spectrum³⁰ for both of the S_2 states oxidized at Mn1

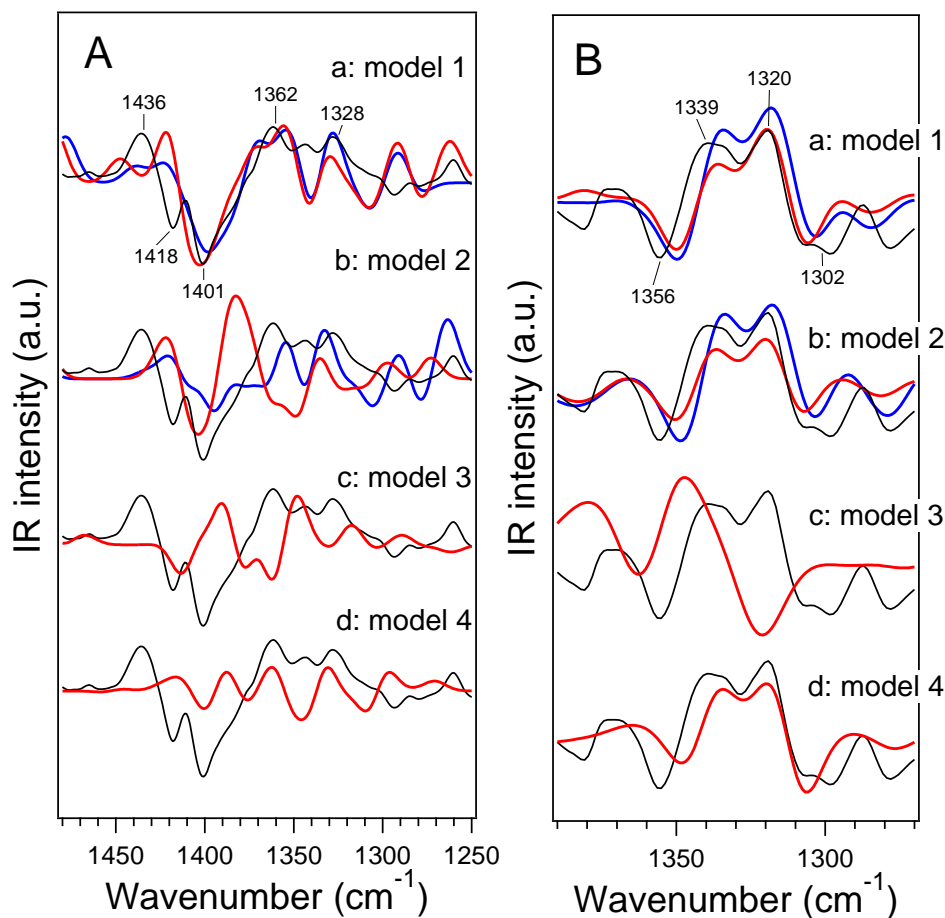


Figure 5.2 Calculated IR spectra in the symmetric COO^- stretching vibrations of carboxylate groups (red or blue lines) compared with experimental FTIR difference spectra (black lines). (A) S_2/S_1 difference spectra. (B) $^{12}\text{C}/^{13}\text{C}$ -A344 S_2/S_1 double-difference spectra. (a) Model 1 (blue line, Mn1-oxidized S_2 ; red line, Mn4-oxidized S_2), (b) model 2 (blue line, Mn1-oxidized S_2 ; red line, Mn4-oxidized S_2), (c) model 3, and (d) model 4. Experimental spectra in A and B were taken from refs. 30 and 31, respectively.

and Mn4 (Figure 5.2 A, a). In particular, the prominent negative band present at 1401 cm^{-1} with positive bands on both the higher- and lower-frequency sides of this peak was well-reproduced. The $^{12}\text{C}/^{13}\text{C}$ -Ala S_2/S_1 double-difference spectra calculated using model 1, with both the Mn1- and Mn4-oxidized S_2 sites, also well-reproduced the experimental spectrum obtained in the work by Chu et al.³¹, which showed major bands at $1356(-)/1339(+)/1320(+)/1302(-)$ representing the vibrations of the C-terminal carboxylate of D1-A344 (Figure 5.2 B, a). The calculated spectra of model 2, with the S_2 states oxidized at Mn1 and Mn4, also showed features similar to those of the experimental S_2/S_1 difference spectrum (Figure 5.2 A, b) and are in good agreement with the

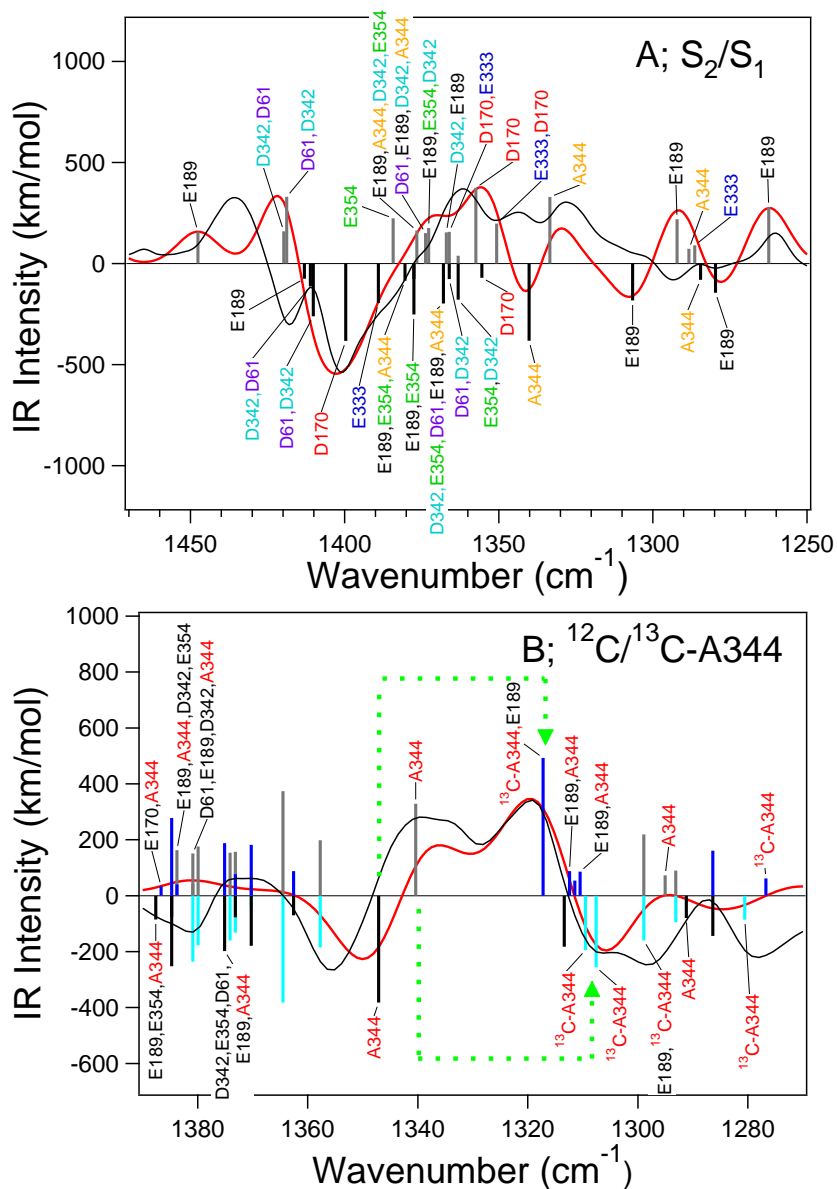


Figure 5.3 Assignments of the symmetric COO^- stretching vibrations of model 1 in the S and Mn4-oxidized S_2 states. (A) S_2/S_1 difference spectrum. (B) $^{12}\text{C}/^{13}\text{C}$ -A344 S_2/S_1 double-difference spectrum. Calculated normal modes of unlabeled WOC are expressed as black (S_1) and gray (S_2) bars, whereas those of $[1-^{13}\text{C}]$ Ala-WOC are expressed as blue (S_1) and cyan (S_2) bars. Calculated and experimental (30, 31) spectra are shown as red and black lines, respectively. In B, $[1-^{13}\text{C}]$ Ala-induced shifts of calculated major A344 modes are indicated by green dotted arrows.

$^{12}\text{C}/^{13}\text{C}$ -Ala S_2/S_1 double-difference spectrum (Figure 5.2 B, b). In contrast to high-oxidation models, the low-oxidation models 3 and 4, poorly reproduced the S_2/S_1 difference spectrum (Figure 5.2 A, c and d). The $^{12}\text{C}/^{13}\text{C}$ -Ala S_2/S_1 difference spectrum was also not reproduced by

Table 5.2 CO bond lengths (Å) of carboxylate groups calculated for high-oxidation models

Carboxylate ^a	Model 1			Model 2			Model 5 (Ca depleted)	
	Length (Å)	ΔS_2 (Mn1) ^b	ΔS_2 (Mn4) ^b	Length (Å)	ΔS_2 (Mn1) ^b	ΔS_2 (Mn4) ^b	Length (Å)	ΔS_2 (Mn4) ^b
E189 (Mn1)	1.295	0.009	0.006	1.297	0.006	0.005	1.295	0.008
E189 (Ca)	1.248	-0.003	-0.001	1.244	0.000	0.000	1.236	-0.003
D342 (Mn1)	1.261	0.014	0.007	1.260	0.012	0.004	1.259	0.002
D342 (Mn2)	1.272	-0.004	-0.002	1.271	-0.004	-0.002	1.269	-0.001
A344 (Ca)	1.236	-0.003	-0.001	1.235	-0.004	-0.001	1.225	-0.001
A344 (Mn2)	1.294	0.009	0.005	1.292	0.009	0.005	1.305	0.003
E354 (Mn2)	1.287	0.001	-0.010	1.289	0.001	-0.008	1.279	-0.008
E354 (Mn3)	1.263	0.006	0.013	1.258	0.005	0.010	1.264	0.011
E333 (Mn3)	1.266	-0.003	-0.008	1.272	0.000	-0.012	1.262	-0.007
E333 (Mn4)	1.277	0.012	0.014	1.266	0.008	0.017	1.275	0.014
D170 (Mn4)	1.271	0.012	0.015	1.257	0.009	0.019	1.294	0.025
D170 (Ca)	1.265	-0.005	-0.008	1.280	-0.004	-0.013	1.235	-0.009
D61 (W1)	1.268	0.011	0.007	1.263	0.009	0.009	1.260	0.008
D61 (W9)	1.262	-0.005	0.002	1.264	-0.004	-0.006	1.266	-0.005

^aInteracting metal or water is in parentheses. ^bChange in length by formation of the S₂ state. Oxidized Mn is indicated in parentheses.

model 3 (Figure 5.2 B, c), although model 4 reproduced major features of the ¹²C/¹³C-A344 difference spectrum (Figure 5.2 B, d).

The calculated normal modes of symmetric COO⁻ vibrations of model 1 in the S₁ and Mn4-oxidized S₂ states are depicted under the simulated S₂/S₁ spectrum in Figure 5.3A. Most of the COO⁻ vibrations show significant couplings among carboxylate groups, although lower-frequency bands at 1350–1250 cm⁻¹ arise from isolated vibrations of A344 and E189, which bridge Mn and Ca ions. It is notable that the prominent negative band at 1401 cm⁻¹ arises mainly from the isolated vibration of D170 in model 1 (Figure 5.3A). The vibration of E333 also contributes to the lower-frequency side of the band. In the S₂ state, these vibrations are downshifted to ~1360 cm⁻¹. The bands at 1436/1418 cm⁻¹ may be assigned to the vibrations of D61, D342, and E189 calculated at 1450–1420/~1410 cm⁻¹ (Figure 5.3A); the deviations from the experimental frequencies may be because of slightly different scaling factors depending on the vibrational modes. The same tendency was also found in model 2. In this case, however, E333 is the main vibration for the 1401-cm⁻¹ band, whereas D170 contributes to the higher-frequency

band together with D61 and D342. Thus, deprotonation of W2 induces a slight rearrangement of COO⁻ vibrations without drastic changes in their frequencies.

Downshifts in frequencies associated with D170 and E333 are consistent with changes in CO lengths within COO⁻ (Table 5.2); the CO bond interacting with Mn4 has a longer length than the other CO bond interacting with Ca (D170) or Mn3 (E333) in the S₁ state, and the former CO further lengthens on S₂ formation, whereas the latter CO is shortened. This asymmetric structure weakens the coupling of two CO vibrations within the COO⁻ group. This change in the coupling increases the contribution of the longer CO bond in the “symmetric” COO⁻ stretching vibration, resulting in observed frequency downshifts. The CO length changes in D170 and E333 are induced by stronger interactions with Mn4 as shown in the tendency toward shortened distances of D170-Mn4 and E333-Mn4 on S₂ formation.

Normal modes in the simulated ¹²C/¹³C-Ala S₂/S₁ double difference spectrum are shown in Figure 5.3B for model 1 with a Mn4-oxidized S₂ state. It is clear that the major experimental bands at 1356/1339/1320/1302 cm⁻¹ arise from ¹³C-induced shifts of isolated A344 vibrations at 1356(S₁)/1339(S₂) cm⁻¹ to 1320(S₁)/1302(S₂) cm⁻¹ by 36–37 cm⁻¹. The relatively low frequency of the A344 vibration and the 17 cm⁻¹ downshift on S₂ formation are consistent with its asymmetric structure and an increased asymmetry on S₂ formation; it has longer (1.294 Å) and

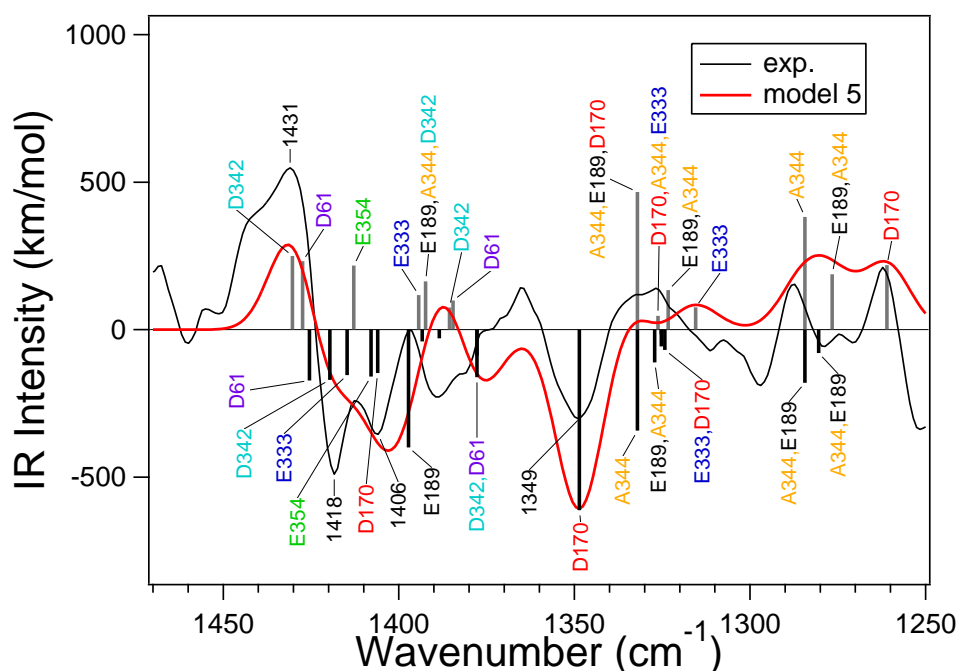


Figure 5.4 A calculated S₂/S₁ IR difference spectrum in the symmetric COO⁻ stretching region of the Ca-depleted WOC model (model 5; red line) compared with the experimental FTIR difference spectrum of Ca-depleted PSII (black line). Calculated normal modes are expressed as black (S₁) and gray (S₂) bars. The experimental spectrum was taken from ref. 28.

shorter (1.236 Å) CO bonds on the Mn2 and Ca sides, respectively, which change by +0.0005 and -0.0001 Å, respectively. Weak coordination to Ca is reflected in the distance of A344-Ca (2.54 Å), which is long relative to A344-Mn2 (1.91 Å), in good agreement with experimental values (2.43 and 1.90 Å, respectively). This weak coordination to Ca is also consistent with experimental observations that the A344 bands are insensitive to the replacement of Ca²⁺ with Sr²⁺.³² Similar trends in vibrational frequencies and bond lengths within A344 are also found in other high-oxidation models.

A simulated S₂/S₁ difference spectrum of the Ca-depleted WOC (model 5), which is shown in Figure 5.4 with band assignments, is in good agreement with the experimental spectrum.²⁸ In particular, the isolated D170 vibration at ~1400 cm⁻¹ in the intact WOC (Figure 5.3A) is downshifted to ~1350 cm⁻¹, and a positive feature around 1360 cm⁻¹ arising from the coupled D170 vibrations is lost. These alterations are consistent with a change from bidentate to unidentate coordination on Ca²⁺ removal, which is reflected in variations in CO lengths (specifically, +0.024 and -0.030 Å on the Mn4 and free sides, respectively) (Table 5.2). Vibrations of other carboxylate groups are also rearranged significantly on Ca²⁺ depletion (Figure 5.4).

5.4. Discussion

A number of theoretical simulations of the Mn cluster have been attempted to clarify details regarding its structure and physical properties. Most of these simulations focused on the geometry and the spin properties of the Mn cluster to reproduce the X-ray structure as well as EXAFS and EPR data.^{10, 13, 15, 20, 21} In a recent study, Chuah et al.²³ performed DFT calculations on the Mn cluster with its first-shell ligands to outline how carboxylate stretching frequencies behave on Mn oxidation and deprotonation. In this study, we present a successful simulation of the FTIR difference spectra of the WOC in the carboxylate stretching region; to do this simulation, we performed QM/MM calculations with a large QM region including nearby amino acids and water molecules in addition to first-shell ligands (Figure 5.1).

Our calculations satisfactorily reproduced the symmetric COO⁻ stretching region of the experimental S₂/S₁ difference spectrum³⁰ by using high-oxidation models (models 1 and 2), which have an oxidation state of (III, IV, IV, III) in the S₁ state (Figure 5.2 A, a and b). Model 1 showed a slightly better reproduction compared with model 2. Both of the high-oxidation models also showed a good reproduction of the ¹²C/¹³C-A344 S₂/S₁ double-difference spectrum³¹ (Figure 5.2 B, a and b), which specifically represents the A344 (C-terminal carboxylate) bands. This result indicates that the A344 vibrations in the S₁ and S₂ states are estimated correctly by the calculations. In addition, the Ca-depleted model (model 5) showed a good agreement with the experimental S₂/S₁ difference spectrum of Ca-depleted PSII²⁸ (Figure 5.4). These successful reproductions of

experimental spectra lend credibility to the QM/MM calculations and proposed assignments of prominent spectral features (Figures 5.3 and 5.4).

In contrast to the high-oxidation models, both of the low-oxidation models (models 3 and 4) (Table 5.1) did not reproduce the S_2/S_1 difference spectrum (Figure 5.2 A, c and d). In addition, the $^{12}\text{C}/^{13}\text{C}$ -Ala difference spectrum was not reproduced by model 3, although the major spectral feature was reproduced by model 4 (Figure 5.2 B, c and d). Thus, low-oxidation models previously used to reproduce X-ray structures¹² are unlikely according to carboxylate vibrations. Previous DFT simulations of EXAFS and EPR data also support this conclusion.¹⁰

The QM region used in vibrational analysis includes six carboxylate ligands surrounding the Mn cluster and the D61 hydrogen bonded to W1. The result that simulations with this QM region reproduced the experimental FTIR difference spectra in the COO^- stretching region indicates that the COO^- bands in the spectra originate mostly from these seven carboxylate groups closely interacting with the Mn cluster. The vibrations of these carboxylate groups are coupled significantly with each other in most normal modes (Figure 5.3A). On formation of S_2 , carboxylate groups are rearranged without drastic changes in coordination, resulting in frequency shifts and alteration in couplings shown in the simulated S_2/S_1 difference spectrum (Figure 5.3A). Because strong couplings exist among carboxylate groups alongside charge delocalization, we concluded that virtually all of the carboxylate groups contribute to the experimental spectrum (Figure 5.3A). Among the normal modes, D170 and E333, ligands bound to Mn4, have rather isolated vibrations at $\sim 1400\text{ cm}^{-1}$ in S_1 , which change to coupled vibrations at $\sim 1360\text{ cm}^{-1}$ on S_2 formation, providing prominent bands at these positions in the difference spectrum (Figure 5.3A). In addition, the calculated Mulliken charges show that an additional charge is distributed largely to Mn4 when not only Mn4 is oxidized but also, Mn1 is formally oxidized on S_2 formation. This increased charge at Mn4 induces frequency downshifts of carboxylate ligands. Thus, this charge distribution to Mn4 explains the major contribution of the Mn4 ligands (D170 and E333) to the spectral feature and further explains the unexpected similarity between the calculated spectra with Mn1- and Mn4-oxidized S_2 states (Figure 5.2 A, a). Large changes in Mn4 ligands are consistent with a recent QM/MM analysis of the $S_2 - S_1$ difference Fourier map from XFEL X-ray diffraction data,⁴⁰ which suggests that the main structural change during the $S_1 \rightarrow S_2$ transition is in the position of Mn4 and its coordination environment.⁴¹ Krewald et al.¹⁰ also suggested that the $S_1 \rightarrow S_2$ transition should mostly affect the D170 and E333 vibrations because of Mn4(III)'s loss of Jahn–Teller axis on oxidation. The experimental observation that the prominent negative band at $\sim 1400\text{ cm}^{-1}$ is lost on Ca^{2+} depletion^{28, 36} is also consistent with the assignment of this band to D170 bridging Mn4 and Ca; the spectral change is well-explained in calculation of the Ca-depleted WOC (model 5), in which the D170 vibration downshifts to $\sim 1350\text{ cm}^{-1}$ because of a change from bidentate to unidentate coordination (Figure 5.4). Assigning the $\sim 1400\text{-cm}^{-1}$ band

to a carboxylate bridge between Mn and Ca was previously proposed from this FTIR observation.²⁸

Site-directed mutagenesis of cyanobacteria has been used to investigate how carboxylate amino acid residues are involved in COO⁻ vibrations of FTIR difference spectra of S-state transitions.^{33-35, 42-49} In contrast to selective isotope labeling using [1-¹³C]A344,^{31, 32} the effects of mutation on FTIR spectra are not straightforward because of the full or partial inactivation of the WOC on mutation of critical residues, secondary effects on WOC structure, and rearrangement of vibrational couplings of carboxylate groups. On E354Q mutation, the S₂/S₁ FTIR difference spectrum showed intensity changes in the 1440- to 1300-cm⁻¹ region, which spans virtually the entire symmetric COO⁻ region.^{33, 34} Because the E354 vibration contributes to coupled modes over the 1390- to 1360-cm⁻¹ range in calculated spectra (Figure 5.3A), experimental alterations may be explained by rearrangements in the ligand structure and changes in vibrational couplings that occur in addition to the loss of E354 vibrations. In addition, D61A mutation induced changes in the 1440- to 1410-cm⁻¹ and 1370- to 1320-cm⁻¹ regions of the S₂/S₁ spectrum,³⁵ which are consistent with major contributions of D61 to coupled modes present at 1420–1410 and 1370–1360 cm⁻¹ (Figure 5.3A). We note several puzzling observations; specifically, mutations of D170, E189, E333, and D342 induced no or minor changes in the COO⁻ region in the FTIR difference spectra during the S-state cycle, which is concomitant with little change in oscillation patterns.^{42-44, 49} These carboxylate ligands are thought to be crucial in supporting the structure of the Mn cluster, where their negative charges should be important in determining the redox potential of S-state intermediates. Thus, it is expected that mutations within these carboxylate groups would significantly affect the WOC structure as well as its reactions. In addition, vibrations of these carboxylate groups are heavily coupled with those of other carboxylate groups (Figure 5.3A). Thus, mutation of one of the carboxylate groups (even if it is not coordinated to the formally oxidized Mn) should alter vibrational features, resulting in perturbation in the FTIR difference spectra. Indeed, mutations in amino acid residues that are located far from the Mn cluster but interact with it through a hydrogen bond network, such as D2-K317,^{45, 46} D1-N181,⁵⁰ D1-E65, D2-E312, D1-R334, and D1-Q165,^{47, 48} showed clear changes in the COO⁻ region of the FTIR spectra during the S-state cycle. In most cases, the mutations also lowered the efficiency of the S₃→S₀ transition. Although recent DFT studies suggested that deprotonation of water/hydroxide ligands coordinating an oxidized Mn suppresses frequency shifts of carboxylate ligands,^{23, 51} the S₁→S₂ transition is not accompanied by release of protons⁵²; additionally, it is not possible that several carboxylate ligands are all silent in any Mn models. Rather, the data in these DFT studies, which showed frequency shifts, to a more or less extent, in virtually all of the carboxylate ligands,^{28, 51} are consistent with our results. Additional studies on carboxylate ligands mutants are necessary to resolve discrepancies between the mutational effects

on FTIR data and QM/MM calculation results.

We also note a clear trend where D170, A344, and E189, which bridge Mn and Ca, show asymmetric structural changes; this trend includes lengthened CO bonds on the Mn side and shortened CO bonds on the Ca side on S₂ formation (Table 5.2), which result in relatively large frequency downshifts (Figure 5.3A). This change is caused by an increase in positive charge on Mn ions on S₂ formation, which attracts a negative charge on the COO⁻ group and induces single- and double-bond characters in the CO bonds on Mn and Ca sides, respectively (Mn...O⁻-C = O...Ca). This shift of negative charge through the conjugated COO⁻ group from the Ca side to the Mn side eventually increases the positive charge on Ca²⁺, which then increases the acidity of water molecules on Ca (W3 and W4). This alteration in charge on Ca is also reflected in a decrease in Ca-W3 and Ca-W4 distances and an increase in OH lengths in W3 and W4 on S₂ formation. It is known that replacing Ca²⁺ with Sr²⁺ decreases the water oxidation rate,⁵³ which can be caused by the difference in Lewis acidity between Ca²⁺ and Sr²⁺.^{54, 55} It is, thus, possible that the W3 and W4 attached to Ca²⁺ are involved in proton release in water oxidation, especially during the S₂→S₃ transition, which is inhibited by Ca²⁺ depletion.⁵⁶ It has also been proposed that W3 approaches to Mn4 during the S₂→S₃ transition in the so-called oxo-oxyl mechanism.^{13, 17, 22} Thus, the carboxylate ligands bridging Mn and Ca ions may play an important role in water oxidation by tuning the reactivity of water ligands on Ca by charge shifts via their π conjugation.

References

- [1] McEvoy, J. P., and Brudvig, G. W. (2006) Water-splitting chemistry of photosystem II, *Chem. Rev.* 106, 4455-4483.
- [2] Cox, N., and Messinger, J. (2013) Reflections on substrate water and dioxygen formation, *Biochim. Biophys. Acta* 1827, 1020-1030.
- [3] Yano, J., and Yachandra, V. (2014) Mn₄Ca cluster in photosynthesis: Where and how water is oxidized to dioxygen, *Chem. Rev.* 114, 4175-4205.
- [4] Umena, Y., Kawakami, K., Shen, J. R., and Kamiya, N. (2011) Crystal structure of oxygen-evolving photosystem II at a resolution of 1.9 Å, *Nature* 473, 55-60.
- [5] Suga, M., Akita, F., Hirata, K., Ueno, G., Murakami, H., Nakajima, Y., Shimizu, T., Yamashita, K., Yamamoto, M., Ago, H., and Shen, J. R. (2015) Native structure of photosystem II at 1.95 Å resolution viewed by femtosecond X-ray pulses, *Nature* 517, 99-103.
- [6] Joliot, P., Barbieri, G., and Chabaud, R. (1969) A new model of photochemical centers in system II, *Photochem. Photobiol* 10, 309-329.
- [7] Kok, B., Forbush, B., and McGloin, M. (1970) Cooperation of charges in photosynthetic O₂ evolution-I. A linear four step mechanism, *Photochem. Photobiol.* 11, 457-475.
- [8] Roelofs, T. A., Liang, W., Latimer, M. J., Cinco, R. M., Rompel, A., Andrews, J. C., Sauer, K.,

- Yachandra, V. K., and Klein, M. P. (1996) Oxidation states of the manganese cluster during the flash-induced S-state cycle of the photosynthetic oxygen-evolving complex, *Proc. Natl. Acad. Sci. U. S. A.* *93*, 3335-3340.
- [9] Kulik, L. V., Epel, B., Lubitz, W., and Messinger, J. (2007) Electronic structure of the $\text{Mn}_4\text{O}_x\text{Ca}$ cluster in the S_0 and S_2 states of the oxygen-evolving complex of photosystem II based on pulse ^{55}Mn -ENDOR and EPR spectroscopy., *J. Am. Chem. Soc.* *129*, 13421-13435.
- [10] Krewald, V., Retegan, M., Cox, N., Messinger, J., Lubitz, W., DeBeer, S., Neese, F., and Pantazis, D. A. (2015) Metal oxidation states in biological water splitting, *Chem. Sci.* *6*, 1676-1695.
- [11] Zheng, M., and Dismukes, G. C. (1996) Orbital configuration of the valence electrons, ligand field symmetry, and manganese oxidation states of the photosynthetic water oxidizing complex: Analysis of the S_2 state multiline EPR signals, *Inorg. Chem.* *35*, 3307-3319.
- [12] Petrie, S., Pace, R. J., and Stranger, R. (2015) Resolving the differences between the 1.9 Å and 1.95 Å crystal structures of photosystem II: A single proton relocation defines two tautomeric forms of the water-oxidizing complex, *Angew. Chem. Int. Ed.* *54*, 7120-7124.
- [13] Ames, W., Pantazis, D. A., Krewald, V., Cox, N., Messinger, J., Lubitz, W., and Neese, F. (2011) Theoretical evaluation of structural models of the S_2 state in the oxygen evolving complex of Photosystem II: protonation states and magnetic interactions, *J. Am. Chem. Soc.* *133*, 19743-19757.
- [14] Pantazis, D. A., Ames, W., Cox, N., Lubitz, W., and Neese, F. (2012) Two interconvertible structures that explain the spectroscopic properties of the oxygen-evolving complex of photosystem II in the S_2 state, *Angew. Chem. Int. Ed.* *51*, 9935-9940.
- [15] Galstyan, A., Robertazzi, A., and Knapp, E. W. (2012) Oxygen-evolving Mn cluster in photosystem II: The protonation pattern and oxidation state in the high-resolution crystal structure, *J. Am. Chem. Soc.* *134*, 7442-7449.
- [16] Siegbahn, P. E. (2013) Water oxidation mechanism in photosystem II, including oxidations, proton release pathways, O-O bond formation and O_2 release, *Biochim. Biophys. Acta* *1827*, 1003-1019.
- [17] Bovi, D., Narzi, D., and Guidoni, L. (2013) The S_2 state of the oxygen-evolving complex of photosystem II explored by QM/MM dynamics: spin surfaces and metastable states suggest a reaction path towards the S_3 state, *Angew. Chem. Int. Ed. Engl.* *52*, 11744-11749.
- [18] Pal, R., Negre, C. F., Vogt, L., Pokhrel, R., Ertem, M. Z., Brudvig, G. W., and Batista, V. S. (2013) S_0 -State model of the oxygen-evolving complex of photosystem II, *Biochemistry* *52*, 7703-7706.
- [19] Saito, K., and Ishikita, H. (2014) Influence of the Ca^{2+} ion on the Mn_4Ca conformation and the H-bond network arrangement in Photosystem II, *Biochim. Biophys. Acta* *1837*, 159-166.

- [20] Askerka, M., Vinyard, D. J., Wang, J., Brudvig, G. W., and Batista, V. S. (2015) Analysis of the radiation-damage-free X-ray structure of photosystem II in light of EXAFS and QM/MM data, *Biochemistry* 54, 1713-1716.
- [21] Li, X., Siegbahn, P. E., and Ryde, U. (2015) Simulation of the isotropic EXAFS spectra for the S₂ and S₃ structures of the oxygen evolving complex in photosystem II, *Proc. Natl. Acad. Sci. U. S. A.* 112, 3979-3984.
- [22] Shoji, M., Isobe, H., and Yamaguchi, K. (2015) QM/MM study of the S₂ to S₃ transition reaction in the oxygen-evolving complex of photosystem II, *Chem. Phys. Lett.* 636, 172-179.
- [23] Chuah, W. Y., Stranger, R., Pace, R. J., Krausz, E., and Frankcombe, T. J. (2016) Deprotonation of water/hydroxo ligands in clusters mimicking the water oxidizing complex of PSII and its effect on the vibrational frequencies of ligated carboxylate groups., *J. Phys. Chem. B* 120, 377-385.
- [24] Nakamura, S., Ota, K., Shibuya, Y., and Noguchi, T. (2016) Role of a water network around the Mn₄CaO₅ cluster in photosynthetic water oxidation: A Fourier transform infrared spectroscopy and quantum mechanics/molecular mechanics calculation study, *Biochemistry* 55, 597-607.
- [25] Chu, H. A. (2013) Fourier transform infrared difference spectroscopy for studying the molecular mechanism of photosynthetic water oxidation, *Front. Plant Sci.* 4, 146.
- [26] Debus, R. J. (2015) FTIR studies of metal ligands, networks of hydrogen bonds, and water molecules near the active site Mn₄CaO₅ cluster in Photosystem II, *Biochim. Biophys. Acta* 1847, 19-34.
- [27] Noguchi, T. (2015) Fourier transform infrared difference and time-resolved infrared detection of the electron and proton transfer dynamics in photosynthetic water oxidation, *Biochim. Biophys. Acta* 1847, 35-45.
- [28] Noguchi, T., Ono, T., and Inoue, Y. (1995) Direct detection of a carboxylate bridge between Mn and Ca²⁺ in the photosynthetic oxygen-evolving center by means of Fourier transform infrared spectroscopy, *Biochim. Biophys. Acta* 1228, 189-200.
- [29] Noguchi, T., and Sugiura, M. (2003) Analysis of flash-induced FTIR difference spectra of the S-state cycle in the photosynthetic water-oxidizing complex by uniform ¹⁵N and ¹³C isotope labeling, *Biochemistry* 42, 6035-6042.
- [30] Noguchi, T., and Sugiura, M. (2002) Flash-induced FTIR difference spectra of the water oxidizing complex in moderately hydrated photosystem II core films: Effect of hydration extent on Sstate transitions, *Biochemistry* 41, 2322-2330.
- [31] Chu, H.-A., Hillier, W., and Debus, R. J. (2004) Evidence that the C-terminus of the D1 polypeptide of photosystem II is ligated to the manganese ion that undergoes oxidation during the S₁ to S₂ transition: An isotope-edited FTIR study, *Biochemistry* 43, 3152-3166.

- [32] Strickler, M. A., Walker, L. M., Hillier, W., and Debus, R. J. (2005) Evidence from biosynthetically incorporated strontium and FTIR difference spectroscopy that the C-terminus of the D1 polypeptide of photosystem II does not ligate calcium, *Biochemistry* 44, 8571-8577.
- [33] Shimada, Y., Suzuki, H., Tsuchiya, T., Tomo, T., Noguchi, T., and Mimuro, M. (2009) Effect of a single-amino acid substitution of the 43 kDa chlorophyll protein on the oxygen-evolving reaction of the cyanobacterium *Synechocystis* sp. PCC 6803: Analysis of the Glu354Gln mutation, *Biochemistry* 48, 6095-6103.
- [34] Service, R. J., Yano, J., McConnell, I., Hwang, H. J., Nicks, D., Hille, R., Wydrzynski, T., Burnap, R. L., Hillier, W., and Debus, R. J. (2011) Participation of glutamate-354 of the CP43 polypeptide in the ligation of manganese and the binding of substrate water in photosystem II, *Biochemistry* 50, 63-81.
- [35] Debus, R. J. (2014) Evidence from FTIR difference spectroscopy that D1-Asp61 influences the water reactions of the oxygen-evolving Mn₄CaO₅ cluster of photosystem II, *Biochemistry* 53, 2941-2955.
- [36] Taguchi, Y., and Noguchi, T. (2007) Drastic changes in the ligand structure of the oxygen-evolving Mn cluster upon Ca²⁺ depletion as revealed by FTIR difference spectroscopy, *Biochim. Biophys. Acta* 1767, 535-540.
- [37] Case, D., Darden, T., Cheatham III, T., Simmerling, C., Wang, J., Duke, R., Luo, R., Walker, R., Zhang, W., and Merz, K. AMBER 12; University of California: San Francisco, 2012, *University of California, San Francisco*.
- [38] Vreven, T., Byun, K. S., Komaromi, I., Dapprich, S., Montgomery, J. A., Morokuma, K., and Frisch, M. J. (2006) Combining quantum mechanics methods with molecular mechanics methods in ONIOM, *J. Chem. Theory Comput.* 2, 815-826.
- [39] Frisch, M. J., Trucks, G. W., Schlegel, H. B., Scuseria, G. E., Robb, M. A., Cheeseman, J. R., Scalmani, G., Barone, V., Mennucci, B., Petersson, G. A., Nakatsuji, H., Caricato, M., Li, X., Hratchian, H. P., Izmaylov, A. F., Bloino, J., Zheng, G., Sonnenberg, J. L., Hada, M., Ehara, M., Toyota, K., Fukuda, R., Hasegawa, J., Ishida, M., Nakajima, T., Honda, Y., Kitao, O., Nakai, H., Vreven, T., Montgomery, J. A., Jr., Peralta, J. E., Ogliaro, F., Bearpark, M., Heyd, J. J., Brothers, E., Kudin, K. N., Staroverov, V. N., Kobayashi, R., Normand, J., Raghavachari, K., Rendell, A., Burant, J. C., Iyengar, S. S., Tomasi, J., Cossi, M., Rega, N., Millam, J. M., Klene, M., Knox, J. E., Cross, J. B., Bakken, V., Adamo, C., Jaramillo, J., Gomperts, R., Stratmann, R. E., Yazyev, O., Austin, A. J., Cammi, R., Pomelli, C., Ochterski, J. W., Martin, R. L., Morokuma, K., Zakrzewski, V. G., Voth, G. A., Salvador, P., Dannenberg, J. J., Dapprich, S., Daniels, A. D., Farkas, O., Foresman, J. B., Ortiz, J. V., Cioslowski, J., and Fox, D. J. (2009) *Gaussian 09*, revision C.01, *Gaussian Inc., Wallingford CT*.

- [40] Kern, J., Alonso-Mori, R., Tran, R., Hattne, J., Gildea, R. J., Echols, N., Glockner, C., Hellmich, J., Laksmono, H., Sierra, R. G., Lassalle-Kaiser, B., Koroidov, S., Lampe, A., Han, G., Gul, S., Difiore, D., Milathianaki, D., Fry, A. R., Miahnahri, A., Schafer, D. W., Messerschmidt, M., Seibert, M. M., Koglin, J. E., Sokaras, D., Weng, T. C., Sellberg, J., Latimer, M. J., Grosse-Kunstleve, R. W., Zwart, P. H., White, W. E., Glatzel, P., Adams, P. D., Bogan, M. J., Williams, G. J., Boutet, S., Messinger, J., Zouni, A., Sauter, N. K., Yachandra, V. K., Bergmann, U., and Yano, J. (2013) Simultaneous femtosecond X-ray spectroscopy and diffraction of photosystem II at room temperature, *Science* 340, 491-495.
- [41] Askerka, M., Wang, J., Brudvig, G. W., and Batista, V. S. (2014) Structural changes in the oxygen-evolving complex of photosystem II induced by the S₁ to S₂ transition: A combined XRD and QM/MM study, *Biochemistry* 53, 6860-6862.
- [42] Debus, R. J., Strickler, M. A., Walker, L. M., and Hillier, W. (2005) No evidence from FTIR difference spectroscopy that aspartate-170 of the D1 polypeptide ligates a manganese ion that undergoes oxidation during the S₀ to S₁, S₁ to S₂, or S₂ to S₃ transitions in photosystem II, *Biochemistry* 44, 1367-1374.
- [43] Strickler, M. A., Hillier, W., and Debus, R. J. (2006) No evidence from FTIR difference spectroscopy that glutamate-189 of the D1 polypeptide ligates a Mn ion that undergoes oxidation during the S₀ to S₁, S₁ to S₂, or S₂ to S₃ transitions in photosystem II, *Biochemistry* 45, 8801-8811.
- [44] Service, R. J., Yano, J., Dilbeck, P. L., Burnap, R. L., Hillier, W., and Debus, R. J. (2013) Participation of glutamate-333 of the D1 polypeptide in the ligation of the Mn₄CaO₅ cluster in photosystem II, *Biochemistry* 52, 8452-8464.
- [45] Pokhrel, R., Service, R. J., Debus, R. J., and Brudvig, G. W. (2013) Mutation of lysine 317 in the D2 subunit of photosystem II alters chloride binding and proton transport, *Biochemistry* 52, 4758-4773.
- [46] Suzuki, H., Yu, J. F., Kobayashi, T., Nakanishi, H., Nixon, P. J., and Noguchi, T. (2013) Functional roles of D2-Lys317 and the interacting chloride ion in the water oxidation reaction of photosystem II as revealed by Fourier transform infrared analysis, *Biochemistry* 52, 4748-4757.
- [47] Service, R. J., Hillier, W., and Debus, R. J. (2010) Evidence from FTIR difference spectroscopy of an extensive network of hydrogen bonds near the oxygen-evolving Mn₄Ca cluster of photosystem II involving D1-Glu65, D2-Glu312, and D1-Glu329, *Biochemistry* 49, 6655-6669.
- [48] Service, R. J., Hillier, W., and Debus, R. J. (2014) Network of hydrogen bonds near the oxygen-evolving Mn₄CaO₅ cluster of photosystem II probed with FTIR difference spectroscopy, *Biochemistry* 53, 1001-1017.

- [49] Strickler, M. A., Walker, L. M., Hillier, W., Britt, R. D., and Debus, R. J. (2007) No evidence from FTIR difference spectroscopy that aspartate-342 of the D1 polypeptide ligates a Mn ion that undergoes oxidation during the S₀ to S₁, S₁ to S₂, or S₂ to S₃ transitions in photosystem II, *Biochemistry* 46, 3151-3160.
- [50] Pokhrel, R., Debus, R. J., and Brudvig, G. W. (2015) Probing the effect of mutations of asparagine 181 in the D1 subunit of photosystem II, *Biochemistry* 54, 1663-1672.
- [51] Terrett, R., Frankcombe, T., Pace, R., and Stranger, R. (2016) Effect of concomitant oxidation and deprotonation of hydrated Mn centres in rationalising the FTIR difference silence of D1-Asp170 in Photosystem II, *J. Inorg. Biochem.* 155, 101-104.
- [52] Suzuki, H., Sugiura, M., and Noguchi, T. (2009) Monitoring proton release during photosynthetic water oxidation in photosystem II by means of isotope-edited infrared spectroscopy, *J. Am. Chem. Soc.* 131, 7849-7857.
- [53] Boussac, A., and Rutherford, A. (1988) Nature of the inhibition of the oxygen-evolving enzyme of photosystem II induced by NaCl washing and reversed by the addition of Ca²⁺ or Sr²⁺, *Biochemistry* 27, 3476-3483.
- [54] Vrettos, J. S., Stone, D. A., and Brudvig, G. W. (2001) Quantifying the ion selectivity of the Ca²⁺ site in photosystem II: evidence for direct involvement of Ca²⁺ in O₂ formation, *Biochemistry* 40, 7937-7945.
- [55] Pitari, F., Bovi, D., Narzi, D., and Guidoni, L. (2015) Characterization of the Sr²⁺- and Cd²⁺-substituted oxygen-evolving complex of photosystem II by quantum mechanics/molecular mechanics calculations, *Biochemistry* 54, 5959-5968.
- [56] Yocum, C. F. (1991) Calcium activation of photosynthetic water oxidation, *Biochim. Biophys. Acta* 1059, 1-15.

Protonation structure of a key histidine in the water oxidizing center

6.1. Introduction

It is well established that the water oxidation reaction proceeds through a cycle of five intermediates called S_n states ($n = 0-4$).^{1, 2} For $n = 0-3$, the S_n states advance to the S_{n+1} states by removal of an electron by a Y_Z radical (Y_Z^\bullet). The S_1 state is the most stable in the dark, even though the S_0 state is the most reduced intermediate. The S_4 state has the highest oxidation state but is a transient intermediate that immediately relaxes to the S_0 state, releasing an oxygen molecule.

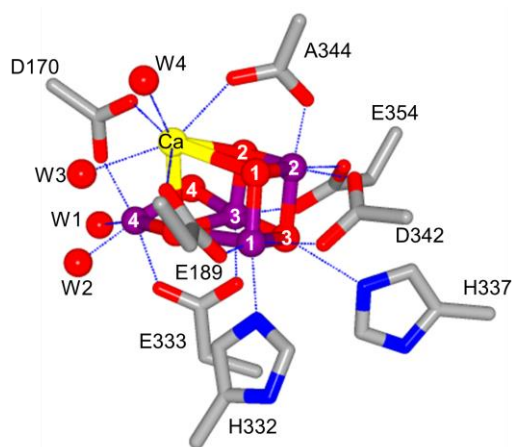


Figure 6.1 an expanded view of the Mn cluster with directly interacting amino acid residues and water molecules deduced from the XFEL structure of PSII (PDB ID 4UB6). Mn, purple; Ca, orange; O, red. Amino acid residues are on the D1 subunit, except for R357 and E354 on the CP43 subunit and K317 on the D2 subunit.

The structure of the WOC has been determined by high-resolution X-ray crystallography using synchrotron radiation^{3, 4} and an X-ray free-electron laser (XFEL).⁵⁻⁷ The Mn cluster in the S_1 state has a structure of a Mn_3Ca cubane (Mn1–Mn3 and Ca) combined with an additional Mn (Mn4), in which the metal ions are bridged by five oxygen atoms (O1–O5). The

Mn and Ca ions are coordinated by six carboxylate groups [D1-D170, D1-E189, D1-E333, D1-D342, D1-A344 (C-terminus), and CP43-E354], one imidazole group (D1-H332), and four water ligands (W1 and W2 on Mn4 and W3 and W4 on Ca). In addition, D1-H337 and CP43-R357 directly interact with the Mn cluster through hydrogen bonds with the bridging oxygen atoms. (Figure 6.1) This core part of the WOC is further surrounded by two Cl⁻ ions (Cl-1 and Cl-2), several water molecules, and amino acid residues (Y_Z, D1-H190, D1-D61, etc.) that might be involved in the water oxidation reaction.

Although the basic structure of the WOC is now known, the protonation structures of amino acid residues and water molecules, and hence the exact structures of the hydrogen-bond networks in the WOC, are still unknown, because the X-ray structures have not resolved hydrogen atoms.³⁻⁷ However, such information on protonation structures and hydrogen-bond networks is crucial for understanding the molecular mechanism of water oxidation, which involves the release of protons and the movement of water molecules. In addition, the protonation and deprotonation of amino acid residues and water molecules change the charge distribution around the Mn cluster, which is a major factor determining its redox potential (E_m). The E_m value of water oxidation is +0.88 V at pH 6.0, whereas that of Y_Z, an immediate electron acceptor of the Mn cluster, has been estimated to be between +0.9 and +1.0 V.^{8, 9} Thus, the E_m value of the Mn cluster must be controlled to be about +0.9 V on average during the S-state cycle to enable water oxidation.

The protonation structure in the WOC has been studied mainly by theoretical calculations based on high-resolution X-ray structures.¹⁰⁻²¹ In particular, as an amino acid residue near the Mn cluster, the protonation state of D1-H337 interacting with O₃ has been extensively disputed.¹⁶⁻²¹ The protonation/deprotonation of this His directly interacting with the Mn cluster should have a significant impact on the E_m value of the Mn cluster and should thus play a crucial role in the water oxidation mechanism. Also, the involvement of D1-H337 in proton-transfer reactions has been suggested.¹⁹ However, little experimental information, except for the hydrogen-bond distance determined by X-ray crystallography,³⁻⁵ has been obtained so far about the protonation state of D1-H337. In this study, we determined the protonation state of D1-H337 using polarized attenuated total reflectance Fourier transform infrared (ATR-FTIR) spectroscopy in combination with a light-induced difference technique. Here, we detected the NH stretching vibration of a His side chain coupled with the S-state transitions and examined the orientation of its transition dipole moment. The assignment of the vibration of D1-H337 and the determination of its protonation state were assisted by vibrational analysis using quantum mechanics/molecular mechanics (QM/MM) calculations. The QM/MM calculations further showed the significant role of D1-H337 in the control of E_m during the reaction cycle of water oxidation.

6.2. Materials and Methods

Sample Preparation. PSII membranes²² were prepared from spinach as reported previously²³ and suspended in a Mes buffer [buffer A: 200 mM Mes (pH 6.0), 5 mM NaCl, and 5 mM CaCl₂]. Samples for ATR-FTIR measurements were prepared by the method described previously^{24, 25} with slight modifications. For ATR-FTIR measurements of the WOC, 1 mL of the PSII suspension (0.5 mg of Chl/mL) in buffer A was centrifuged at 170000g for 5 min. The pellet was resuspended in 100 μ L of the same buffer, diluted with 880 μ L of Milli-Q water, and then mixed with 20 μ L of 100 mM sodium ferricyanide. The sample was centrifuged at 4000g for 5 min, and 900 μ L of the supernatant was removed. The precipitate was suspended in the remaining solution, and 10 μ L of the suspension was loaded on the surface of a three-reflection silicon prism (3 mm in diameter) of the ATR accessory (DuraSamplIR II, Smiths Detection) and then dried under nitrogen gas flow. To form a moderately hydrated film,²⁶ 2 μ L of a 20% (v/v) glycerol/water solution was placed near the sample but without touching it, and then the sample was covered with an acrylic plate together with a silicone sheet spacer (0.5 mm in thickness). The temperature of the sample was maintained at 283 K by circulating cooled water through a copper plate attached to the sample stage. In the case of Q_A^-/Q_A measurements, a PSII sample that was depleted of the Mn cluster by NH₂OH (10 mM) treatment for 30 min was used. The pellet obtained after centrifugation (170000g for 5 min) was resuspended in 100 μ L of buffer A, which was diluted with 870 μ L of Milli-Q water and mixed with 10 μ L of 100 mM NH₂OH, 10 μ L of 1 mM 3-(3,4-dichlorophenyl)-1,1-dimethylurea (DCMU)/ethanol, and 10 μ L of 5 mM phenazine methosulfate (PMS). Other procedures were the same as those for the measurements of the WOC.

Polarized ATR-FTIR Measurements. FTIR spectra were recorded on a Bruker IFS-66/S spectrophotometer equipped with a mercury cadmium telluride (MCT) detector (InfraRed D313-L) at 4 cm⁻¹ resolution. Illumination was performed with a flash from a Qswitched Nd:YAG laser (Quanta-Ray Indi; 532 nm, \sim 7 ns fwhm, \sim 20 mJ cm⁻² pulse⁻¹ at the sample). In the WOC measurements, after the sample had been set on the ATR crystal, the transition efficiency of the S-state cycle was first estimated; the sample was illuminated by two preflashes and then subjected to 1 h of dark adaptation to synchronize the WOC to the S₁ state, after which 12 successive flashes were applied. Single-beam spectra with 20 scans (10-s accumulation) were recorded twice before the illumination and once after each flash, to calculate difference spectra upon individual flashes together with a difference spectrum between the first two dark spectra representing the noise level. Subsequently, polarized ATR-FTIR difference spectra were recorded with perpendicular and parallel polarizations of the incident IR beam, which were produced using a wire grid polarizer (ST-Japan, STJ-1001).²⁴ After two preflashes (1-s interval) and subsequent 1-h dark relaxation, four flashes were applied, and single-beam spectra with 20 scans (10-s accumulation) were

recorded twice before the illumination and once after each flash. This procedure (including preflashes) was repeated at an interval of 1 h. The signals of the nonheme iron ($\text{Fe}^{2+}/\text{Fe}^{3+}$)^{27, 28} that contaminate the first-flash spectra as a result of the preoxidation of the nonheme iron by ferricyanide and subsequent photoreduction can be significantly diminished by repetitive measurements because of the slow reoxidation of Fe^{2+} . The polarization of the incident IR beam was changed every two to four measurements. Twelve samples were used, and spectra of 44 and 48 measurements in total for perpendicular and parallel polarizations, respectively, were averaged to calculate difference spectra for the first through fourth flashes, together with a dark-minus-dark spectrum representing the noise level.

To examine the extent of membrane orientation on the ATR crystal surface, polarized ATR-FTIR difference spectra of Q_A upon its photoreduction were measured with a sample containing DCMU (see above).²⁴ Single-beam spectra with 80 scans (40-s accumulation) were recorded twice before and once after a single flash, and this measurement was repeated with a 1-h interval for dark relaxation. The polarization of the incident IR beam was changed every four to eight measurements, and spectra of 16 and 36 measurements in total for perpendicular and parallel polarizations, respectively, were averaged using one sample. These spectra were used to calculate light-minus-dark (Q_A^-/Q_A) difference spectra, together with a dark-minus-dark (noise level) difference spectrum.

Analysis of the polarized ATR-FTIR spectra was performed as described previously.²⁴ The dichroic ratio R , which is defined as $\Delta A_{//}/\Delta A_{\perp}$ (where ΔA_{\perp} and $\Delta A_{//}$ are the absorbance changes for perpendicular and parallel polarizations, respectively), was correlated with an orientational order parameter S ²⁹

$$R = \frac{A_{//}}{A_{\perp}} = \frac{E_x^2}{E_y^2} + \frac{E_z^2}{E_y^2} \left(1 + \frac{3S}{1-S} \right) \quad (1)$$

where E_x^2 , E_y^2 , and E_z^2 are the time-average squared electric field amplitudes of the evanescent wave. Specifically, E_x^2 , E_y^2 , and E_z^2 are expressed as

$$E_x^2 = \frac{4 \cos^2 \theta (\sin^2 \theta - n_{21}^2)}{(1 - n_{21}^2)[(1 + n_{21}^2) \sin^2 \theta - n_{21}^2]} \quad (2)$$

$$E_y^2 = \frac{4 \cos^2 \theta}{1 - n_{21}^2} \quad (3)$$

$$E_z^2 = \frac{4 \cos^2 \theta \sin^2 \theta}{(1 - n_{21}^2)[(1 + n_{21}^2) \sin^2 \theta - n_{21}^2]} \quad (4)$$

In eqs 2–4, $n_{21} = n_2/n_1$, where n_1 and n_2 are the refractive indices of an internal reflection element (IRE) and the external medium, respectively, and θ represents the angle of the incident IR beam with respect to the normal of the IRE surface. An n_1 value of 1.5 has been used for PSII membranes^{24, 30, 31} with $n_2 = 3.42$ for a Si crystal of an IRE and θ equal to 45° , E_x^2 , E_y^2 , and E_z^2

are 1.887, 2.476, and 3.066, respectively. The experimental order parameter S in eq. 1 is defined as

$$S = S_{\text{ms}}S_{\text{dp}} \quad (5)$$

where S_{ms} represents the dispersion of the membrane normal with respect to the normal of the IRE surface by mosaic spread^{24, 30, 31} and S_{dp} represents an order parameter, which means the orientation of the transition dipole moment of a normal-mode vibration. When the membranes are perfectly oriented, $S_{\text{ms}} = 1$, whereas a totally random orientation provides $S_{\text{ms}} = 0$. In the latter case, R is equal to 2 by ATR-FTIR spectroscopy since the penetration depth for parallel polarization is 2 times greater than that of perpendicular polarization. S_{dp} is related to the angle φ of the transition dipole with respect to the membrane normal through the equation

$$S_{\text{dp}} = \frac{3 \cos^2 \varphi - 1}{2} \quad (6)$$

Thus, once S_{ms} has been determined, the φ value of a vibration of interest can be estimated from the R value in eqs 1, 5, and 6.

Quantum Chemical Calculations. Quantum chemical calculations were performed using the Gaussian 09 program package.³² The atomic coordinates of the Mn cluster and of amino acid residues, water molecules, and Cl^- ions located within 20 Å of the Mn cluster were taken from the X-ray free-electron laser (XFEL) structure of the PSII complex at 1.95 Å resolution (PDB ID 4UB6).⁵ The hydrogen atoms were generated and optimized using Amber. QM/MM calculations were performed using the ONIOM (our own n-layered integrated molecular orbital and molecular mechanics) method³³ as described previously³⁴⁻³⁶ with a minor modification. The QM region consisted of the Mn cluster, its amino acid ligands (D1-D170, D1-E189, D1-H332, D1-E333, D1-D342, D1-A344, and CP43-E354), nearby amino acid side residues (side chains of Y_Z, D1-H190, D1-N298, D1-D61, CP43-R357, and D1-H337 and the backbone between D1-E329 and D1-V330), and 15 nearby water molecules involving water ligands (W1–W4), whereas other atoms in the selected region of PSII were assigned to the MM region. The titratable groups of the amino acid residues in the QM and MM regions except for D1-H337 were assumed to be in standard protonation states at neutral pH. For the estimation of the E_{m} value of the Mn cluster in the $S_1 \rightarrow S_2$ transition, the QM region was slightly modified to include more charged residues and ions without changing the overall QM/MM region; D2-K317, two Cl^- ions (Cl-1 and Cl-2), and one water molecule (ligand to Cl-2) were added, and D1-N298 and the backbone between D1-E329 and D1-V330 were removed to maintain a similar size of the QM region. The oxidation states of the Mn ions in the S_1 state were (Mn1, Mn2, Mn3, Mn4) = (III, IV, IV, III), and Mn1 or Mn4 was oxidized upon S_2 formation.^{10-19, 37, 38} High spin states were assumed in calculations. It is noted that the spin configuration minimally affects the geometry of the Mn cluster^{10, 12, 15} and, hence, the vibrations of the surroundings. The geometry of the QM region was optimized by fixing

other atoms in the MM region using ONIOM (B3LYP:Amber). Normal-mode calculations were performed for the optimized geometries of the QM region. As basis sets in the QM calculations, LANL2DZ was used for Ca and Mn, and 6-31G(d) was used for the other atoms. No scaling was employed for the calculated vibrational frequencies.

E_m versus the standard hydrogen electrode (SHE) of the $S_1 \rightarrow S_2$ transition was calculated from the energies of the S_1 and S_2 states (E_{S1} and E_{S2} , respectively), which were corrected with zero-point energies, using the equation

$$E_m = \frac{(E_{S2} - E_{S1})}{F} - E_H \quad (7)$$

where F is the Faraday constant and E_H is the absolute potential of the SHE, which has been estimated to be 4.43 V.^{39, 40}

6.3. Results

In the present study, we utilized polarized ATR-FTIR spectroscopy to identify the NH vibration and its orientation for a His residue coupled with the S-state cycle of the WOC. The spectra were analyzed using QM/MM calculations. The outline of the experiments and analyses is as follows. (1) The extent of orientation of the PSII membranes on the Si surface, which is expressed as S_{ms} , was estimated by detecting the dichroic ratio of the strong CO stretching band of Q_A^- . (2) The miss probability of the S-state cycle was estimated by measuring nonpolarized ATR-FTIR spectra upon successive 12 flashes and subsequent simulation of the oscillation pattern. (3) Polarized ATR-FTIR spectra of the S-state cycle were measured with four flashes. The obtained spectra in the 1800–1000 cm^{-1} region, where characteristic peaks of the S-state transitions appear, were examined to confirm that the spectra of individual S-state transitions were properly obtained and the previous polarized FTIR spectra were well reproduced. (4) The spectral features in the 3000–2200 cm^{-1} region, which involves the NH vibrations of His, were examined. Spectra of pure contributions of the individual S-state transitions were calculated using the miss probability, and the orientations of the transition dipole moments of the NH vibrations were estimated using the dichroic ratios of prominent bands and the S_{ms} value. (5) QM/MM calculations were performed to assign the observed signals to the specific His residue from the frequencies and the orientations of the NH vibrations. The protonation state of this His residue was also determined. (6) The impact of the protonation states of this His and W2 on the redox potential of the Mn cluster was examined by further QM/MM calculations.

Estimation of the Orientation of the PSII Membranes on the IRE Surface. We first estimated the extent of orientation of the PSII membranes on the IRE surface by obtaining S_{ms} utilizing the R value of the CO stretching vibration of Q_A^- .²⁴ We used this vibration for the

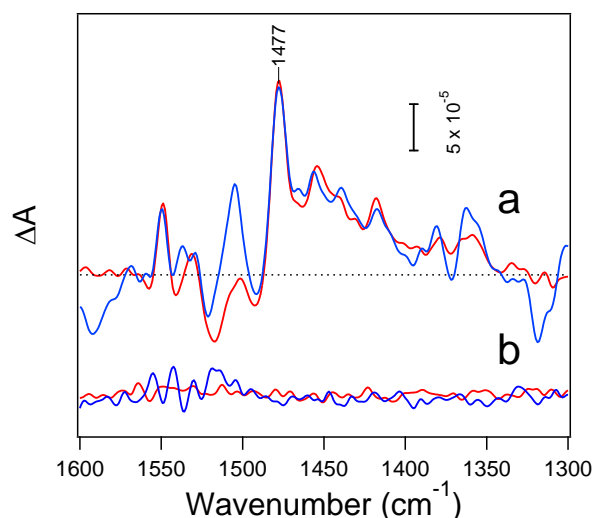


Figure 6.2 Polarized ATR-FTIR difference spectra upon light-induced (a) Q_A^- formation and (d) dark-minus-dark spectra of oriented PSII membranes. Spectra were recorded with parallel (blue lines) and perpendicular (red lines) polarizations of the incident IR light. The zero line is shown in black.

estimation of S_{ms} because it provides a strong band at $\sim 1477\text{ cm}^{-1}$, where no other prominent bands overlap, and the direction of its transition dipole moment is readily determined in the crystal structure. Figure 6.2 shows the polarized Q_A^-/Q_A ATR-FTIR difference spectra of the oriented PSII membranes. The dichroic ratio R of the positive band at 1477 cm^{-1} originating from the asymmetric CO stretching vibration of Q_A^- , which is coupled with the CC stretches and the methyl deformations,⁴¹⁻⁴³ was estimated to be 0.97 ± 0.03 , which is similar to the result obtained in our previous study (0.99 ± 0.01).²⁴ The orientation of this CO vibration of Q_A^- (φ) with respect to the membrane normal (the vector between the nonheme iron and the midpoint of two Mg atoms of P680) was estimated to be 81.9° from the high-resolution (1.95 \AA) XFEL structure (PDB ID 4UB6)⁵ and the deviation of the transition dipole moment of this vibration from the C1–O1 bond by 7.1° , which was obtained in a previous study.²⁴ Note that this value of 81.9° is slightly different from the previous estimation of 77° , which was obtained using a lower-resolution (2.9 \AA) X-ray structure of PSII.⁴⁴ From eqs 1, 5, and 6, S_{ms} was estimated to be 0.81 ± 0.03 using $R = 0.97 \pm 0.03$ and $\varphi = 81.9^\circ$, indicating that moderately hydrated PSII membranes are highly oriented on the IRE surface.

Estimation of the Miss Probability of the S-State Cycle. Before the measurement of polarized ATR-FTIR difference spectra of the WOC in oriented PSII membranes, we estimated the miss probability of the S-state cycle for the same sample, but using a nonpolarized IR beam,

by applying 12 flashes. In this system, we used ferricyanide as an exogenous electron acceptor. The obtained spectra (1500–1300 cm^{-1}) are presented in Figure 6.3A, showing the spectral features of the S-state cycle very similar to those previously obtained using spinach and cyanobacterial PSII samples.⁴⁵⁻⁴⁸ Prominent bands in the 1450–1300 cm^{-1} region have been assigned to the symmetric COO^- stretching vibrations of carboxylate groups around the Mn

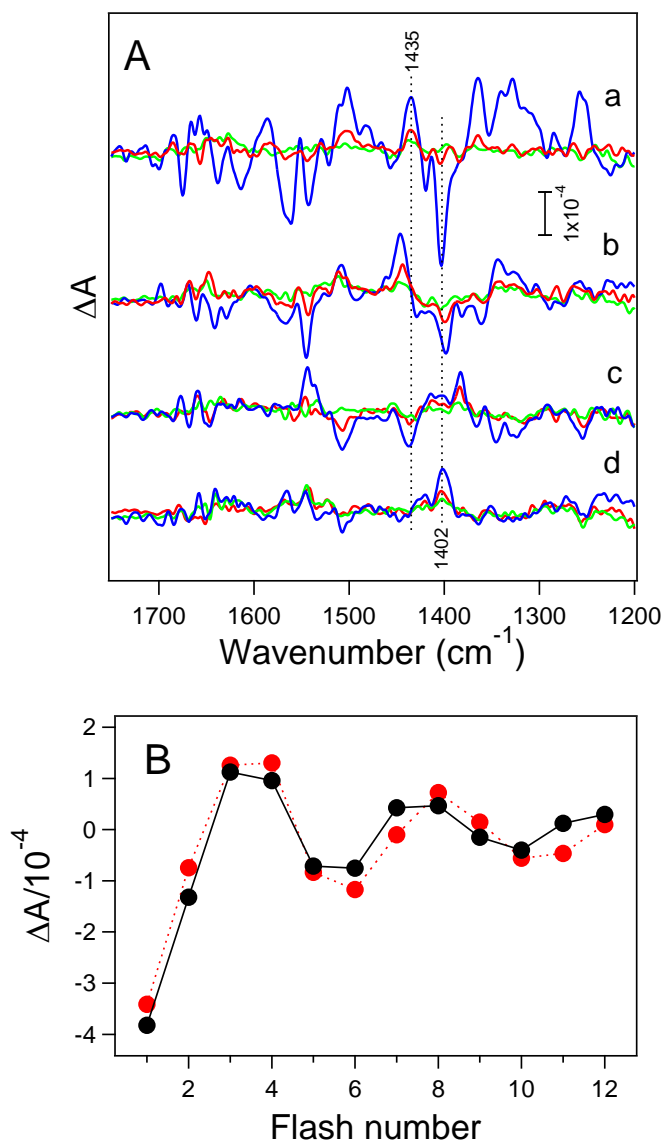


Figure 6.3 (A) ATR-FTIR difference spectra of the WOC in oriented PSII membranes upon 12 successive flashes (1750–1300 cm^{-1}). (a–d) Difference spectra upon the (a) $(4i + 1)$ th, (b) $(4i + 2)$ th, (c) $(4i + 3)$ th, and (d) $(4i + 4)$ th flashes ($i = 0, 1, 2$) are presented in blue ($i = 0$), red ($i = 1$), and green ($i = 2$). (B) Flash-number dependence of the intensity difference at 1402 and 1435 cm^{-1} (solid circles), together with a simulated oscillation pattern (open circles) providing an average miss probability of 0.18. Errors were estimated from the noise level of the dark-minus-dark spectrum (panel A, trace e).

cluster.^{35, 49} The plot of the intensity difference between 1402 and 1435 cm^{-1} , where prominent negative and positive bands are located in the first-flash spectrum, against the flash number (Figure 6.3B, solid circles) showed a clear period-four oscillation pattern. This pattern was simulated assuming a single miss factor and no double hits (open circles),⁵⁰ providing a miss probability of 0.18 ± 0.04 . Note that this value is relatively high compared with the miss values (~ 0.1) previously obtained by using phenyl-pbenzoquinone (PpBQ) as the electron acceptor for similar PSII membranes or by the combination of PSII core complexes and ferricyanide.^{51, 52} This relatively high miss value, however, is not due to the sample form of a moderately hydrated film, because our previous study using a pellet sample of spinach PSII membranes also showed a similar miss value of 0.17–0.18 with ferricyanide as the electron acceptor.⁵² Thus, the high miss

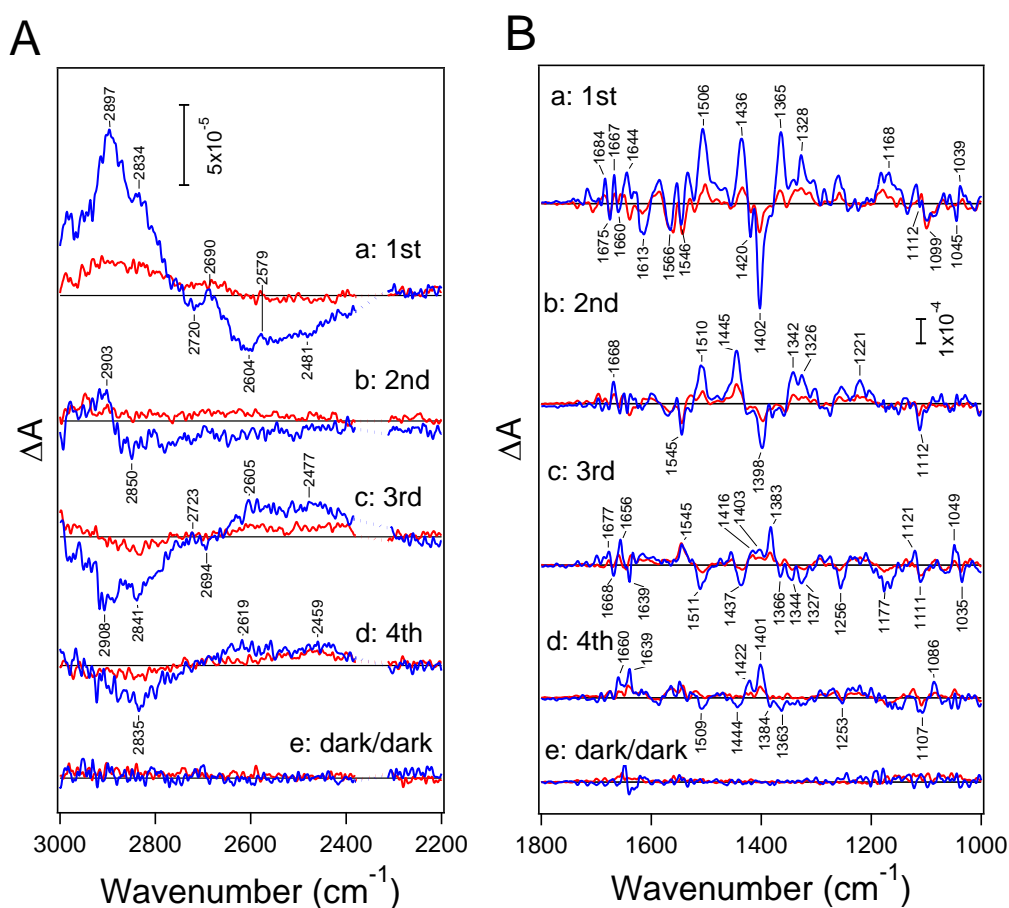


Figure 6.4 Polarized ATR-FTIR difference spectra (A: 3000–2200 cm^{-1} region and B: 1800–1000 cm^{-1} region) of the WOC in oriented PSII membranes upon the (a) first, (b) second, (c) third, and (d) fourth flashes and (e) corresponding dark-minus-dark difference spectra measured with parallel (blue lines) and perpendicular (red lines) polarizations of the incident IR light. Zero lines are shown in black. The frequency range of the spectra surrounding 2340 cm^{-1} , shown as dotted lines, is overlapped by the signal of CO_2 in the atmosphere.

value can be ascribed to ferricyanide, which is less accessible to the acceptor side of PSII in the membrane sample.⁵² However, we avoided using PpBQ as the electron acceptor because of the involvement of nonheme iron signals ($\text{Fe}^{3+}/\text{Fe}^{2+}$) in difference spectra with a period-two oscillation due to oxidation of Fe^{2+} by PpBQ^- to produce Fe^{3+} at odd-numbered flashes and its photoreduction at even-numbered flashes.⁵³

Polarized ATR-FTIR Spectra of the S-State Cycle. Figure 6.4A shows polarized ATR-FTIR difference spectra (red, perpendicular; blue, parallel) of the S-state transitions upon the first through fourth flashes in the 1800–1000 cm^{-1} region. Bands in the first-flash spectra due to the $\text{S}_1 \rightarrow \text{S}_2$ transition (Figure 6.4Aa) showed dichroic ratios very similar to those found in our previous study;²⁴ most of the bands in the symmetric COO^- region (1450–1300 cm^{-1}) showed large R values, whereas the bands in the region of asymmetric COO^- and amide II bands (1600–1500 cm^{-1}) showed relatively small R values, except for the band at 1506 cm^{-1} , which has a high R value. The same tendency was observed in other spectra at the second (Figure 6.4Ab), third (Figure 6.4Ac), and fourth (Figure 6.4Ad) flashes, mainly representing the $\text{S}_2 \rightarrow \text{S}_3$, $\text{S}_3 \rightarrow \text{S}_0$, and $\text{S}_0 \rightarrow \text{S}_1$ transitions, respectively. The observed R values (2.0–5.0) for the symmetric COO^- bands indicate that the angles of the transition moments of these vibrations with respect to the membrane normal are in the range between 30° and 60°.²⁴ It is noted here that our recent QM/MM calculations showed that most of the symmetric COO^- vibrations of the carboxylate groups around the Mn cluster are significantly coupled with each other³⁵ and, hence, the angles of the transition dipole moments do not simply represent the orientations of individual carboxylate groups.

The polarized ATR-FTIR difference spectra of the S-state cycle in the high-frequency region of 3000–2200 cm^{-1} are shown in Figure 6.4B (red, perpendicular; blue, parallel). This frequency region includes the vibrations of polarizable protons in OH or NH groups with strong hydrogen bonds in water molecules and proteins.^{36, 54-56} The first-flash spectrum with parallel polarization shows broad positive and negative features at about 2900 and 2600 cm^{-1} , respectively, superimposed by several minor peaks (Figure 6.4Ba). Similar features but of opposite sign were observed in the third-flash spectrum with parallel polarization (Figure 6.4B c). In contrast, corresponding spectra with perpendicular polarization show only weak intensities in these regions (Figure 6.4B a,c). At the second flash, the band feature was not clear except for a positive band at about 2900 cm^{-1} in parallel polarization (Figure 6.4B b). The spectral feature at the fourth flash with parallel polarization (Figure 6.4B d) was similar to that of the third-flash spectrum, but with a weaker intensity and slightly different positions of the minor peaks. Note that the dark-minus-dark difference spectra (Figure 6.4B e) show virtually straight lines without any specific structures, indicating that the spectral features of the flash-induced spectra (Figure 6.4B a–d) did not involve baseline changes except for only slight shifts.

In Figure 6.5, polarized ATR-FTIR difference spectra of pure contributions of the $S_1 \rightarrow S_2$ and $S_3 \rightarrow S_0$ transitions (blue lines, parallel; red lines, perpendicular) are presented in the 3000–2400 cm^{-1} region. The spectra of the $S_3 \rightarrow S_0$ transition were calculated from the third-flash spectra that were corrected with first- and second-flash spectra using the miss factor of 0.18 (see above), whereas the $S_1 \rightarrow S_2$ spectra were identical to the first-flash spectra. Spectra were also corrected with slight baseline shifts by subtracting dark-minus-dark spectra (Figure 6.4Be) after appropriate smoothing to accurately estimate R values. It can be clearly seen that the pure

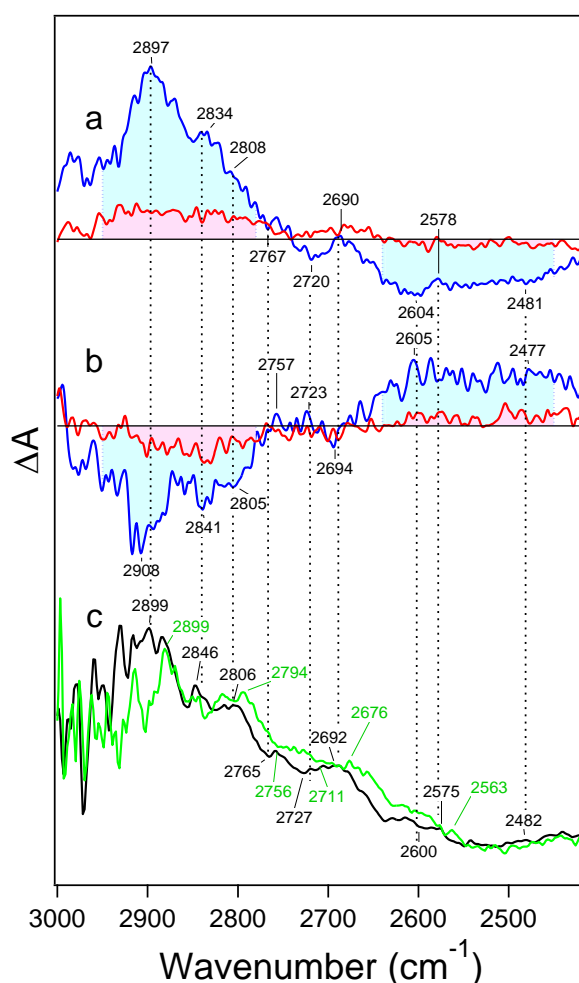


Figure 6.5 (a,b) Corrected polarized FTIR difference spectra (3000–2400 region) representing the pure contributions of the (a) $S_1 \rightarrow S_2$ and (b) $S_3 \rightarrow S_0$ transitions. Blue and red lines indicate parallel and perpendicular polarizations, respectively. Zero lines are shown in black. The areas colored in cyan and magenta at 2950–2780 and 2640–2450 cm^{-1} were used for calculations of the dichroic ratios of the broad bands. (c) FTIR difference spectra of the $S_1 \rightarrow S_2$ transition (c) in the unlabeled (black line) and globally ^{15}N -labeled (green line) PSII membranes of spinach. The spectra in panel c were reproduced from the data of Noguchi et al.⁵⁴

Table 6.1 Dichroic ratios of broad bands in the strongly hydrogen-bonded region of the FTIR difference spectra upon the $S_1 \rightarrow S_2$ and $S_3 \rightarrow S_0$ Transitions

FTIR spectrum	S state	frequency (cm ⁻¹)	dichroic ratio R^a	angle (deg) ^b
S_2/S_1^c	S_1	2640–2450	10.0	19
	S_2	2950–2780	4.3	37
S_0/S_3^d	S_3	2950–2780	6.4	28
	S_0	2640–2450	3.9	39

^aDichroic ratios were calculated from the areas of the parallel and perpendicular polarization spectra from the zero line in the frequency region. ^bAngles of the transition dipole moments with respect to the membrane normal were estimated from R using $S_{ms} = 0.81$. ^c S_2/S_1 spectra (parallel and perpendicular polarizations) are the first-flash spectra corrected with baselines (dark-minus-dark spectra). ^dPure S_0/S_3 spectra (parallel and perpendicular polarizations) were calculated from the first-, second-, and third-flash spectra using a miss factor of 0.18, followed by baseline correction.

S_2/S_1 and S_0/S_3 spectra are virtually mirror images and that not only the broad features but also the minor peaks correspond to each other. These minor peaks on the broad features are in good agreement with those in the previously obtained S_2/S_1 difference spectrum of spinach PSII membranes (Figure 6.5c, black line), which shows downshifts by several wavenumbers upon global ¹⁵N labeling (Figure 6.5c, green line).⁵⁴ The presence of the Fermi resonance peaks of His in the 3000–2400 cm⁻¹ region of the S_2/S_1 and S_0/S_3 spectra (Figure 6.5) indicates that the NH stretching vibrations of the His residue that is perturbed in the $S_1 \rightarrow S_2$ and $S_3 \rightarrow S_0$ transitions are located in this region.

The dichroic ratios (R) of the broad features in the S_2/S_1 and S_0/S_3 spectra at about 2600 and 2900 cm⁻¹ (Table 6.1) were estimated from the areas in the ranges 2640–2450 and 2950–2780 cm⁻¹ (colored magenta and cyan for perpendicular and parallel polarizations, respectively, in Figure 6.5a,b). They were all relatively large (3.9–10.0), indicating small angles of the transition dipole moments with respect to the membrane normal. Indeed, the angles calculated using $S_{ms} = 0.81$ range between 19° and 39° (Table 6.1). The negative feature in the S_1 state at about 2600 cm⁻¹ (Figure 6.5a) resulted in a particularly large R value of 10.0 and a small angle of 19°, whereas the corresponding positive feature at the same frequency in the S_0 state (Figure 6.5b) resulted in a slightly larger angle of 39° ($R = 3.9$). The feature at about 2900 cm⁻¹ in the S_2 and S_3 states resulted in angles of 37° ($R = 4.3$) and 28° ($R = 6.4$), respectively.

His NH Vibrations Estimated by QM/MM Calculations. To assign the bands with large dichroic ratios in the strongly hydrogen-bonded region (Figure 6.5), we performed normal mode analysis of amino acid residues and water molecules around the Mn cluster in the S_1 and S_2 states using QM/MM calculations. The QM region includes all of the amino acid residues and

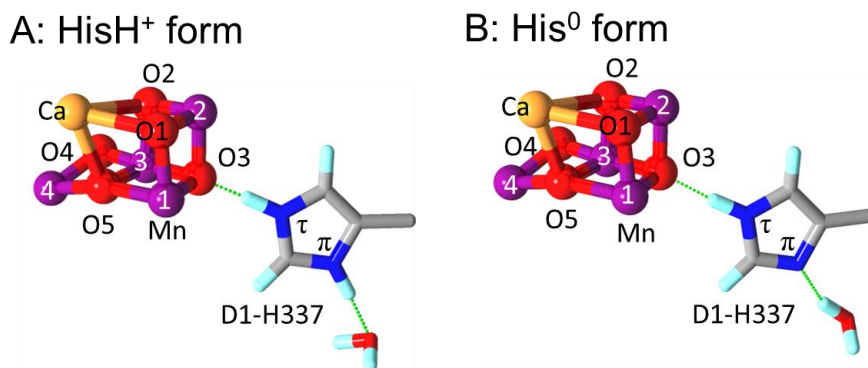


Figure 6.6 Protonation states of D1-H337 in its (A) protonated cation form (HisH⁺) and (B) neutral NτH form (His⁰) in alculated models. Note that a water molecule interacting at the Nπ site of D1-H337 functions as a hydrogen-bond acceptor in panel A and a hydrogen-bond donor in panel B.

water molecules directly interacting with the Mn cluster, together with Y_Z, some nearby residues, and water molecules. Three His residues, D1-H337, D1-H332, and D1-H190 are included in this region; D1-H337 is hydrogen-bonded with O3 of the Mn cluster, whereas D1-H332 is a ligand to Mn1. D1-H190 is hydrogen-bonded with Y_Z and indirectly interacts with the Mn cluster through a hydrogen-bond network. The hydrogen-bond partners of these His side chains, namely, a water molecule for the D1-H337 Nπ, an amide group between D1-D329 and D1-V330 for the D1-H332 Nπ, and a side chain of D1-N298 for the D1-H190 Nπ, were also included in the QM region to correctly estimate the NH vibrations of the His side chains. We calculated four models with different protonation structures regarding W2 and D1-H337, whose protonation states have been extensively investigated in previous theoretical calculations¹⁶⁻²¹ namely, W2 = H₂O or OH⁻ and H337 = HisH⁺ (protonated cation form) or His⁰ (neutral NτH form). In the case of the protonated HisH⁺ form, a water molecule interacting with the NπH functions as the proton acceptor, whereas in the neutral NτH form, the water molecule is a hydrogen-bond donor to the Nπ (Figure 6.6). In contrast, H332 and H190 are forced to have the neutral NπH form, because their Nτ sites function as a ligand to Mn and a hydrogen-bond acceptor of the Y_Z OH, respectively. In calculations, a high oxidation state of the Mn cluster, namely, (Mn1, Mn2, Mn3, Mn4) = (III, IV, IV, III) in the S₁ state, was assumed, and either Mn4 or Mn1 was oxidized in the S₂ state, providing the so-called “open cubane” or “closed cubane” structure, respectively.^{12, 37, 38} The protonation states of the amino acid residues and water molecules in the QM region were unchanged during geometry optimization in both the S₁ and S₂ states, indicating that proton transfer such as from W1/W2 to D61 did not take place upon S₂ formation. It is also noted that the structure with O3–H hydrogen-bonded with neutral H337 (W2 = H₂O) was unstable and converged to the structure with protonated H337.

Table 6.2 Calculated frequencies and orientations of the NH stretching vibrations of his residues around the Mn cluster

model	S ₁				S ₂ (Mn4 oxidation)				S ₂ (Mn1 oxidation)							
	mode	frequency (cm ⁻¹)	IR intensity (km/mol)	angle (deg) ^b	mode	frequency (cm ⁻¹)	IR intensity (km/mol)	angle (deg) ^b	mode	frequency (cm ⁻¹)	IR intensity (km/mol)	angle (deg) ^b	mode	frequency (cm ⁻¹)	IR intensity (km/mol)	angle (deg) ^b
W2 His337 ^a	H337 N π H	2513	3609	13.5	H337 N π H	2922	408	12.9	H337 N π H	2840	3182	13.9	H337 N π H	3255	1191	48.9
	H337 N π H	3343	461	53.1	H337 N π H	3283	-60	49.5	H337 N π H	3110	3207	53.5	H332 N π H	3199	1329	82.4
	H332 N π H	3227	2450	57.2	H332 N π H	3080	-147	56.0	H190 N π H	3453	978	11.8	H332 N π H	3190	2589	55.9
	H190 N π H	3271	1633	89.6	H190 N π H	3199	-72	83.9	H190 N π H	3239	1574	76.7	H190 N π H	3352	1199	89.3
	H337 N π H	3304	2298	25.6	H337 N π H	3447 ^c	143	36.6	H337 N π H	2623	3654	13.5	H337 N π H	3373	169	39.2
	H332 N π H	3287	1879	64.9	H332 N π H	3168	-119	56.3	H332 N π H	3214	2588	59.2	H332 N π H	3383	935	13.1
	H190 N π H	3368	1183	87.1	H190 N π H	3240	-128	76.9	H190 N π H	3381	1268	80.7	H332 N π H	3284	2135	63.3
OH ⁻ HisH ⁺	H337 N π H	2028	4219	14.6	H337 N π H	2668	640	12.7	H337 N π H	3352	1199	89.3	H337 N π H	3383	935	13.1
	H337 N π H	3427	957	45.4	H337 N π H	3371	-56	41.2	H337 N π H	3373	169	39.2	H337 N π H	3383	935	13.1
	H332 N π H	3316	2005	56.5	H332 N π H	3186	-130	57.4	H332 N π H	3214	2588	59.2	H332 N π H	3284	2135	63.3
	H190 N π H	3400	1554	86.6	H190 N π H	3348	-52	89.4	H190 N π H	3352	1199	89.3	H190 N π H	3381	1268	80.7
	H337 N π H	3225	2851	21.1	H337 N π H	3361 ^c	136	78.0	H337 N π H	3383	935	13.1	H337 N π H	3383	935	13.1
	H332 N π H	3382	1791	55.8	H332 N π H	3257	-126	58.8	H332 N π H	3284	2135	63.3	H332 N π H	3284	2135	63.3
	H190 N π H	3423	1034	86.2	H190 N π H	3378	-45	85.3	H190 N π H	3381	1268	80.7	H190 N π H	3381	1268	80.7

^aD1-H337 is in its protonated cation form (HisH⁺) or neutral N π H form (His⁰). ^bAngle of the transition moment of the normal mode with respect to the membrane normal determined in the X-ray structure of PSII (PDB ID 4UB6). ^cVibration strongly coupled with water OH vibrations.

Table 6.2 shows the calculated NH stretching modes of three His side chains (D1-H337, D1-H332, and D1-H190) near the Mn cluster. The calculated NH frequencies and the intensities in the S_1 and S_2 states are also presented in Figure 6.7A, together with the experimental ATR-FTIR spectrum with parallel polarization in panel a. It can be clearly seen that only the $N\tau H$ stretching mode of H337 in the protonated HisH^+ form provided vibrational frequencies in the $3000\text{--}2000\text{ cm}^{-1}$ region (Figure 6.7a), whereas all other NH vibrations of H337, H332, and H190 were calculated to be higher than 3000 cm^{-1} in both the S_1 and S_2 states (Figure 6.7b–d). It should

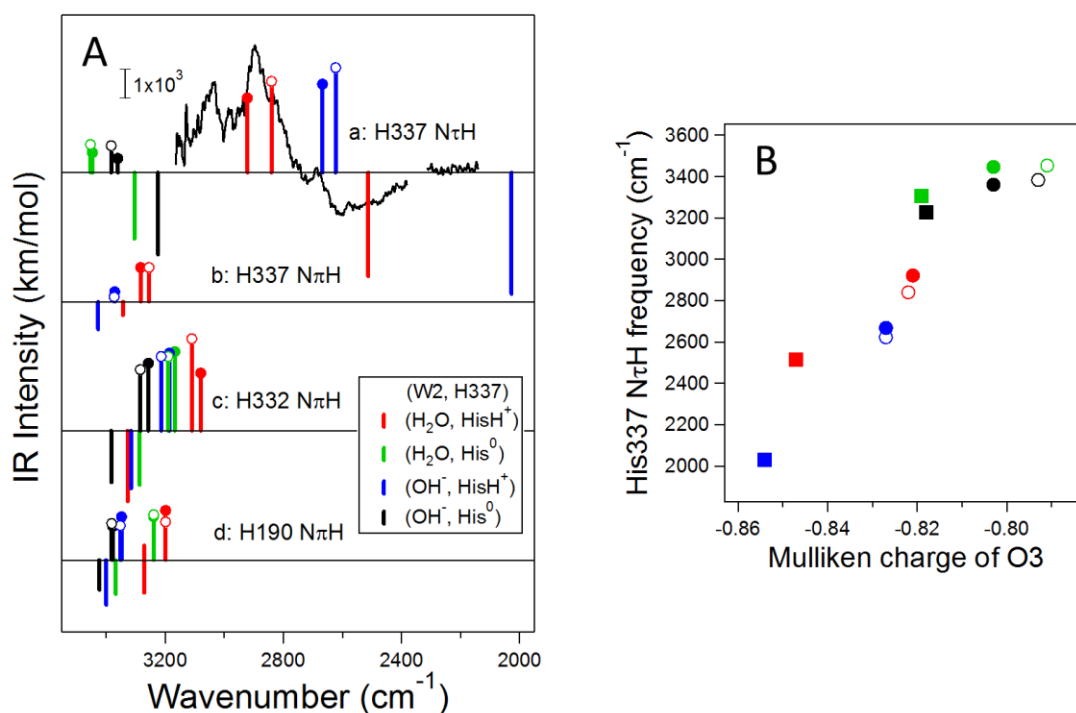


Figure 6.7 (A) Calculated NH stretching vibrations of His residues (D1-H337, D1-H332, and D1-H190) around the Mn cluster: (a) $N\tau H$ of D1-H337, (b) $N\pi H$ of D1-H337, (c) $N\pi H$ of D1-H332, and (d) $N\pi H$ of D1-H190. Calculations were performed for models with $W2/H337 = \text{H}_2\text{O}/\text{HisH}^+$ (red bars), $\text{H}_2\text{O}/\text{His}^0$ (green bars), $\text{OH}^-/\text{HisH}^+$ (blue bars), and OH^-/His^0 (black bars). Negative and positive bars are the vibrations in the S_1 and S_2 states, respectively, and bars with solid and open circles indicate Mn4- and Mn1-oxidized S_2 , respectively. The experimental FTIR spectrum with parallel polarization (black line) is superimposed on the calculated $N\tau H$ vibrations of D1-H337 in panel a. (B) Relationship between the Mulliken charge of O3 and the $N\tau H$ stretching frequency of D1-H337 obtained by QM/MM calculations for models of $W2/H337 = \text{H}_2\text{O}/\text{HisH}^+$ (red), $\text{H}_2\text{O}/\text{His}^0$ (green), $\text{OH}^-/\text{HisH}^+$ (blue), and OH^-/His^0 (black). S_1 state, solid squares; Mn4-oxidized S_2 state, solid circles; Mn1-oxidized S_2 state, open circles

Table 6.3 Calculated distances between O3 and N τ of D1-H337 in comparison with the experimental distance

	model	O3-N τ distance (Å)		
	W2/H337 ^a	S ₁	S ₂ (Mn4-oxidized)	S ₂ (Mn1-oxidized)
QM/MM	H ₂ O/HisH ⁺	2.60	2.70	2.59
	H ₂ O/His ⁰	2.78	2.85	2.74
	OH ⁻ /HisH ⁺	2.54	2.65	2.57
	OH ⁻ /His ⁰	2.75	2.82	2.73
experiment ^b		2.63		

^aD1-H337 is in its protonated cation form (HisH⁺) or neutral N τ H form (His⁰). ^bAverage of monomer A and B (2.60 and 2.65 Å, respectively) in the XFEL structure

be noted that no other NH and OH vibrations of amino acid residues in the QM regions showed frequencies in the 3000–2000 cm⁻¹ region, whereas some of the OH stretching vibrations of water molecules with strong hydrogen bonds showed bands at 3000–2600 cm⁻¹ in the S₂ state, as reported previously.³⁶

The relatively low N τ H frequencies of H337 in the HisH⁺ form are correlated with short hydrogen-bond distances between the O3 of the Mn cluster and the N τ of H337 (Table 6.3). They were calculated to be 2.60 and 2.54 Å in the S₁ state of the W2/H337 = H₂O/HisH⁺ and OH⁻/HisH⁺ structures, respectively, whereas other models with neutral H337 (W2/H337 = H₂O/His⁰ and OH⁻/His⁰) showed longer distances of 2.75–2.78 Å. A similar correlation was also found in the S₂ state: In the Mn4- (Mn1-) oxidized S₂ state, distances of 2.70 (2.59) and 2.65 (2.57) Å were found for protonated H337 with W2 = H₂O and OH⁻, respectively, in comparison with 2.82–2.85 (2.73–2.74) Å for neutral H337.

The N τ H frequencies of H337 are also correlated with the Mulliken charge of O3 (Figure 6.7B): A more negative charge on O3 provides a lower N τ H frequency. When H337 is protonated, O3 has a more negative charge in the model with W2 = OH⁻ (blue marks) than with W2 = H₂O

Table 6.4 Calculated redox potentials (E_m) of the S₁ → S₂ transition^a

W2/H337 ^a	total charge of S ₁ ^c	E_m (V)
H ₂ O/HisH ⁺	0	0.87
H ₂ O/His ⁰	-1	-0.92
OH ⁻ /HisH ⁺	-1	-1.49
OH ⁻ /His ⁰	-2	-3.28

^aMn4-oxidized S₂ state was assumed for estimation of E_m . ^bD1-H337 is in its protonated cation form (HisH⁺) or neutral N τ H form (His⁰). ^cQM region used for the E_m calculation includes all charged species within 8 Å from the Mn cluster.

(red marks) in each S state, providing a lower N τ H frequency. In contrast, the models with neutral H337 (green and black marks) showed less negative O3 charges than the models with protonated H337, providing higher N τ H frequencies. The relationship between the O3 charge and the N τ H frequency holds between the S₁ and S₂ states. In all of the protonation structures, the O3 charge becomes less negative upon S₂ formation, which induces the upshift of the N τ H frequency.

Table 6.2 also includes the calculated angles of the transition dipole moments of His NH vibrations with respect to the membrane normal. The N τ H vibration of H337 showed a small angle of 13–26° in most of the models in both the S₁ and S₂ states, although the vibrations of the models with W2/H337 = H₂O/His⁰ and OH⁻/His⁰ in the Mn4-oxidized S₂ state showed larger angles because of strong couplings with water OH vibrations. In contrast, other NH vibrations of His showed relatively large angles: >39°, >53°, and >76° for H337 N π , H332 N τ , and H190 N τ , respectively.

Estimation of the Redox Potentials of the S₁ → S₂ Transition in Different Protonation Structures. Using the four protonation structures, we calculated the redox potential (E_m) of the S₁ → S₂ transition upon Mn4 oxidation (Table 6.4). In this E_m calculation, we added two Cl⁻ ions and a positively charged D2-K317 residue to the QM region so that all of the charged amino acid side chains and ions within 8 Å from the Mn cluster were included in the QM region. For the structure of W2/H337 = H₂O/HisH⁺, in which the total charge of the QM region is 0, the E_m value was estimated to be +0.87 V, which is close to the E_m value of the water oxidation reaction (+0.88 V at pH 6.0). In contrast, in other protonation structures, namely, W2/H337 = H₂O/His⁰, OH⁻/HisH⁺, and OH⁻/His⁰, the E_m values were all estimated to be negative: -0.92, -1.49, and -3.28 V, respectively. These values indicate that, when W2 is turned into OH⁻ from H₂O, E_m decreases by 2.16 V irrespective of the protonation state of H337, whereas when H337 takes its neutral form instead of its protonated cation form, E_m decreases by 1.79 V irrespective of the protonation state of W2.

6.4. Discussion

In the present study, we measured polarized ATR-FTIR difference spectra of the S-state cycle using the oriented PSII membranes of spinach. With parallel polarization, relatively large features with positive and negative intensities were observed at about 2900 and 2600 cm⁻¹, respectively, in the S₁ → S₂ transition (Figure 6.5a), and opposite-sign signals at the same frequencies were observed in the S₃ → S₀ transition (Figure 6.5b). Only weak intensities were detected with a perpendicular polarization, providing relatively large dichroic ratios (R = 3.9–10.0; Table 6.1). In addition, the broad features at 3000–2400 cm⁻¹ exhibited several minor peaks that also showed mirror images between the S₁ → S₂ and S₃ → S₀ transitions (Figure 6.5a,b).

These minor peaks in the S_2/S_1 difference spectrum have been attributed to the Fermi resonance of the His NH vibration coupled with overtones and combinations of other imidazole vibrations from global ^{15}N -labeling of spinach PSII membranes (Figure 6.5c). Thus, the observation of the Fermi resonance peaks is strong support for the presence of the NH stretching vibrations of a His side chain in the 3000–2400 cm^{-1} region of the S_2/S_1 and S_0/S_3 difference spectra. In addition, the previous observation of significant decreases in the Fermi resonance peaks and broad features in the 3000–2400 cm^{-1} region in D_2O ^{55, 56} are also consistent with the presence of a NH vibration.

Our QM/MM calculations of the WOC, which includes three His residues near the Mn cluster (D1-H337, D1-H332, and D1-H190) in the QM region, indeed showed that D1-H337, which is hydrogen-bonded with O3 of the Mn cluster at the $\text{N}\tau\text{H}$, has a $\text{N}\tau\text{H}$ stretching vibration in the 3000–2000 cm^{-1} region when it is in its protonated cation form (Figure 6.7a; Table 6.2). In particular, the $\text{N}\tau\text{H}$ frequencies of protonated H337 in the $\text{W2} = \text{H}_2\text{O}$ model (2513 cm^{-1} in S_1 and 2922 and 2840 cm^{-1} in Mn4- and Mn1- oxidized S_2 , respectively; Figure 8a, red bars) agree well with the band positions in the experimental S_2/S_1 spectrum with parallel polarization (~ 2600 cm^{-1} in S_1 and ~ 2900 cm^{-1} in S_2 ; Figure 8a, spectrum in black), whereas the frequencies are too low in the $\text{W2} = \text{OH}^-$ model (2028 cm^{-1} in S_1 and 2668 and 2623 cm^{-1} in Mn4- and Mn1-oxidized S_2 , respectively; Figure 8a, blue bars). In contrast, the $\text{N}\pi\text{H}$ vibration of the same cation form of H337 (Figure 6.6B) and the $\text{N}\tau\text{H}$ vibration of neutral H337 (Figure 6.6C) showed much higher frequencies of 3500–3200 cm^{-1} in both the S_1 and S_2 states (Figure 6.7a,b; Table 6.2). The NH vibrations of other nearby His residues, D1-H332 and D1-H190, also showed frequencies higher than 3000 cm^{-1} (Figure 6.7c,d; Table 6.2).

These relatively low $\text{N}\tau\text{H}$ frequencies of protonated H337 reflect a strong hydrogen bond between O3 and $\text{N}\tau\text{H}$. Indeed, the calculated $\text{O3}\cdots\text{N}\tau$ distances of protonated His337 in the S_1 state (2.60 and 2.54 Å for $\text{W2} = \text{H}_2\text{O}$ and OH^- , respectively; Table 6.3) are shorter than the $\text{O}\cdots\text{N}$ distances at the $\text{N}\pi$ of H337 and other His residues. The calculated $\text{O3}\cdots\text{N}\tau$ distance of 2.60 Å in the $\text{W2}/\text{H337} = \text{H}_2\text{O}/\text{HisH}^+$ model is in good agreement with that in the high-resolution XFEL structure,⁵ which is 2.63 Å for this distance (Table 6.3). Longer hydrogen-bond distances at other NH groups of H337, H332, and H190 in the XFEL structure (2.69–2.78 Å) are also consistent with the calculations.

The calculations also indicated a tendency that a lower $\text{N}\tau\text{H}$ frequency of the protonated H337 is correlated with a more negative charge of O3 in the Mn cluster (Figure 6.7B). Thus, the lower $\text{N}\tau\text{H}$ frequency in the $\text{W2}/\text{H337} = \text{OH}^-/\text{HisH}^+$ model than in the $\text{W2}/\text{H337} = \text{H}_2\text{O}/\text{HisH}^+$ model (Figure 6.7Aa) can be explained by the presence of a more negative charge on O3 in the former model (Figure 6.7B). In addition, by electron extraction from the Mn cluster upon S_2 formation, the negative charge of O3 decreases, and the $\text{N}\tau\text{H}$ frequency of H337 upshifts (Figure 6.7B). Thus, the mirror images of the features in the 3000–2200 cm^{-1} region between the $S_1 \rightarrow$

S_2 and $S_3 \rightarrow S_0$ transitions (Figure 6.5) suggests that the change in the O3 charge upon the $S_1 \rightarrow S_2$ transition is reversed in the $S_3 \rightarrow S_0$ transition, whereas no large change in the O3 charge is induced by the $S_2 \rightarrow S_3$ and $S_0 \rightarrow S_1$ transitions, being consistent with minor intensities in this region in the S_3/S_2 and S_1/S_0 difference spectra.

The observed large dichroic ratio ($R = 10.0$) of the $\sim 2600\text{ cm}^{-1}$ band in the polarized S_2/S_1 spectra (Figure 6.5a, Table 6.1) provided a relatively small angle of 19° of the transition dipole moment of this vibration with respect to the membrane normal. The calculated R values for the N τ H vibration of H337 ($13\text{--}26^\circ$; Table 6.2) are in good agreement with this experimental value, whereas other NH vibrations of His residues (N π of H337, H332, and H190) showed much larger calculated angles of $39\text{--}90^\circ$ (Table 6.2). This agreement of the angle of the transition dipole moment is additional strong evidence for the assignment of this feature to the N τ H vibration of H337. Slightly lower R values ($3.9\text{--}6.4$) and hence larger angles ($28\text{--}39^\circ$) in the band at about 2900 cm^{-1} in the S_2 state in the S_2/S_1 spectra (Figure 6.5a) and the bands at about 2600 and 2900 cm^{-1} in the S_0/S_3 spectra (Figure 6.5b) might be due to the overlaps of other vibrations, probably the OH stretching vibrations of strongly hydrogen-bonded water molecules.^{55,56}

From the above observations of the polarized ATR-FTIR spectra and the analysis using QM/MM calculations, it is definitely concluded that the observed FTIR features at about 2600 and 2900 cm^{-1} in the S_2/S_1 and S_0/S_3 difference spectra arise from or involve significant contributions from the N τ H vibration of D1-H337 in its protonated cation form. This also indicates that this His residue remains protonated in all of the metastable S states ($S_0\text{--}S_3$). D1-H337 stays protonated even at high pH values: The S_2/S_1 spectra in the $3000\text{--}2200\text{ cm}^{-1}$ region measured at pH $4\text{--}9$ ⁵⁷ were virtually identical, indicating that the protonation state of H337 does not change in the physiological pH range. It is noted that the proton of H337 is exchangeable, as shown by the D₂O effect (see above), and hence, the reason for staying in its protonated form is not isolation of H337 from the water-accessible region. The protonated cation of H337 is probably energetically stabilized by a strong charge-assisted hydrogen bond with the negatively charged O3.

The above conclusion that D1-H337 has its protonated cation form throughout the S-state cycle indicates that this His residue might not contribute to proton transfer during water oxidation. This is at odds with the previous theoretical prediction that H337 is deprotonated during the $S_2 \rightarrow S_3$ transition.¹⁹ However, our result is consistent with the high-resolution XFEL structure of PSII,⁵ in which the hydrogen bond network from the D1-His337 N π is not directly connected to the bulk and, hence, proton release through this site should require a high energy barrier. It is noted that the recent report of the X-ray structure of PSII showed significantly different O3 \cdots N τ (H337) distances (2.46 and 2.75 \AA) between two monomers (monomer A and B) in the PSII crystal, and the difference was suggested to arise from the deprotonated and protonated forms

of H337.⁴ However, the presence of two different protonation forms in the S_1 state should induce a heterogeneity in the electron-transfer rate in the $S_1 \rightarrow S_2$ transition, which has not been observed in time-resolved spectroscopic studies.⁵⁸⁻⁶¹ It is thus possible that the variation in the $O3 \cdots N\tau(H337)$ distance could be an observation specific to the PSII crystal. Further careful X-ray crystallographic studies in combination with FTIR measurements of PSII crystals⁷ would be necessary to address the origin of the structural difference between the two monomers.

Although D1-H337 probably does not play a role in proton transfer, the positive charge on its cationic form should have a dramatic impact on the E_m value of the Mn cluster, which is a major factor driving electron transfer to Y_Z^\bullet . Our E_m estimation using QM/MM calculations (Table 6.4), in which all of the charged species within 8 Å from the Mn cluster were included in the QM region, showed that only the model with $W2/H337 = H_2O/HisH^+$ provided a positive E_m value of +0.87 V, whereas all other protonation models provided negative E_m values (between -0.92 and -3.28 V) that are not appropriate for water oxidation. The E_m value of +0.87 V is comparable to the E_m value of water oxidation (+0.88 V at pH 6.0) and properly lower than the E_m values of Y_Z (0.9–1.0 V)^{8, 9} and P680 (~1.2 V),^{62, 63} and hence, it is a good estimation for the E_m value of the $S_1 \rightarrow S_2$ transition, in which simple electron transfer takes place from the Mn cluster to Y_Z^\bullet . This E_m value estimated by the present QM/MM calculations is also in good agreement with the previous estimation (between +0.70 and +0.93 V) for the $S_1 \rightarrow S_2$ transition by Amin et al.¹⁹ using multiconformation continuum electrostatic (MCCE) calculations. The good agreement of the calculated E_m value for the $W2/H337 = H_2O/HisH^+$ model with the predicted level is additional evidence that D1-H337 is in its protonated cation form. The E_m calculation also suggested that the protonation structure of W2 is most likely H_2O rather than OH^- in the S_1 and S_2 states. This is supported by the better agreement of the $N\tau H$ frequency and the $O3 \cdots N\tau$ distance with the experimental polarized ATR-FTIR spectra (Figure 6.5) and the XFEL structure,⁵ respectively, in the model with $W2/H337 = H_2O/HisH^+$ than in that with $W2/H337 = OH^-/HisH^+$ (Figure 6.7A, Table 6.3). In addition, our recent QM/MM simulation of the symmetric COO^- stretching vibrations showed that the model with $W2 = H_2O$ provided a slightly better agreement with the experimental S_2/S_1 FTIR difference spectrum.³⁵ [Note that, although our previous simulation of the COO^- vibrations assumed neutral D1-H337, a similar spectrum was obtained for the model with protonated H337]. The protonation structure of $W2/H337 = H_2O/HisH^+$ (thus, all of the water ligands are protonated) in the S_1 state is in agreement with the previously proposed structures based on MCCE¹⁹ and QM/MM¹¹ calculations.

The distribution of charged species around the Mn cluster is crucial for the E_m value. The total charge of the QM region in the S_1 state is 0 in the $W2/H337 = H_2O/HisH^+$ model, whereas other models give total charges of -1 ($W2/H337 = H_2O/His^0$ and $OH^-/HisH^+$) and -2 ($W2/H337 = OH^-/His^0$). In the first model ($H_2O/HisH^+$), the charge of the Mn cluster [(Mn1,

Mn₂, Mn₃, Mn₄) = (III, IV, IV, III)] with the first shell ligands (six COO⁻ groups, one neutral imidazole group, and four neutral water molecules) is 0, and the nearby charged residues (D1-H337 + CP43-R357 + D1-D61 + D2-K317 = +2) and two Cl⁻ ions (-2) cancel the charges. The impact of the protonation of H337 on the E_m value is +1.79 V, whereas that of W2 (OH⁻ to H₂O) is +2.16 V (Table 6.4). The large impact of the protonation of D1-H337 on the E_m value (+1.79 V), which is natural considering the direct hydrogen bonding to the Mn cluster, implies that this His residue plays a crucial role in maintaining the high E_m values of the Mn cluster necessary for water oxidation throughout the S-state cycle.

References

- [1] Joliot, P., Barbieri, G., and Chabaud, R. (1969) A new model of photochemical centers in system II, *Photochem. Photobiol* 10, 309-329.
- [2] Kok, B., Forbush, B., and McGloin, M. (1970) Cooperation of charges in photosynthetic O₂ evolution-I. A linear four step mechanism, *Photochem. Photobiol.* 11, 457-475.
- [3] Umena, Y., Kawakami, K., Shen, J. R., and Kamiya, N. (2011) Crystal structure of oxygen-evolving photosystem II at a resolution of 1.9 Å, *Nature* 473, 55-60.
- [4] Tanaka, A., Fukushima, Y., and Kamiya, N. (2017) Two different structures of the oxygen-evolving complex in the same polypeptide frameworks of photosystem II, *J. Am. Chem. Soc.* 139, 1718-1721.
- [5] Suga, M., Akita, F., Hirata, K., Ueno, G., Murakami, H., Nakajima, Y., Shimizu, T., Yamashita, K., Yamamoto, M., Ago, H., and Shen, J. R. (2015) Native structure of photosystem II at 1.95 Å resolution viewed by femtosecond X-ray pulses, *Nature* 517, 99-103.
- [6] Young, I. D., Ibrahim, M., Chatterjee, R., Gul, S., Fuller, F., Koroidov, S., Brewster, A. S., Tran, R., Alonso-Mori, R., Kroll, T., Michels-Clark, T., Laksmono, H., Sierra, R. G., Stan, C. A., Hussein, R., Zhang, M., Douthit, L., Kubin, M., de Lichtenberg, C., Long Vo, P., Nilsson, H., Cheah, M. H., Shevela, D., Saracini, C., Bean, M. A., Seuffert, I., Sokaras, D., Weng, T. C., Pastor, E., Weninger, C., Fransson, T., Lassalle, L., Brauer, P., Aller, P., Docker, P. T., Andi, B., Orville, A. M., Glowacka, J. M., Nelson, S., Sikorski, M., Zhu, D., Hunter, M. S., Lane, T. J., Aquila, A., Koglin, J. E., Robinson, J., Liang, M., Boutet, S., Lyubimov, A. Y., Uervirojnangkoorn, M., Moriarty, N. W., Liebschner, D., Afonine, P. V., Waterman, D. G., Evans, G., Wernet, P., Dobbek, H., Weis, W. I., Brunger, A. T., Zwart, P. H., Adams, P. D., Zouni, A., Messinger, J., Bergmann, U., Sauter, N. K., Kern, J., Yachandra, V. K., and Yano, J. (2016) Structure of photosystem II and substrate binding at room temperature, *Nature* 540, 453-457.
- [7] Suga, M., Akita, F., Sugahara, M., Kubo, M., Nakajima, Y., Nakane, T., Yamashita, K., Umena,

- Y., Nakabayashi, M., Yamane, T., Nakano, T., Suzuki, M., Masuda, T., Inoue, S., Kimura, T., Nomura, T., Yonekura, S., Yu, L. J., Sakamoto, T., Motomura, T., Chen, J. H., Kato, Y., Noguchi, T., Tono, K., Joti, Y., Kameshima, T., Hatsui, T., Nango, E., Tanaka, R., Naitow, H., Matsuura, Y., Yamashita, A., Yamamoto, M., Nureki, O., Yabashi, M., Ishikawa, T., Iwata, S., and Shen, J. R. (2017) Light-induced structural changes and the site of O=O bond formation in PSII caught by XFEL, *Nature* 543, 131-135.
- [8] Metz, J. G., Nixon, P. J., Rogner, M., Brudvig, G. W., and Diner, B. A. (1989) Directed alteration of the D1 polypeptide of photosystem II: Evidence that tyrosine-161 is the redox component, Z, connecting the oxygen-evolving complex to the primary electron-donor, P680, *Biochemistry* 28, 6960-6969.
- [9] Vass, I., and Styring, S. (1991) pH-Dependent charge equilibria between tyrosine-D and the S states in photosystem II. Estimation of relative midpoint redox potentials, *Biochemistry* 30, 830-839.
- [10] Ames, W., Pantazis, D. A., Krewald, V., Cox, N., Messinger, J., Lubitz, W., and Neese, F. (2011) Theoretical evaluation of structural models of the S₂ state in the oxygen evolving complex of Photosystem II: protonation states and magnetic interactions, *J. Am. Chem. Soc.* 133, 19743-19757.
- [11] Luber, S., Rivalta, I., Umena, Y., Kawakami, K., Shen, J. R., Kamiya, N., Brudvig, G. W., and Batista, V. S. (2011) S₁-state model of the O₂-evolving complex of photosystem II, *Biochemistry* 50, 6308-6311.
- [12] Isobe, H., Shoji, M., Yamanaka, S., Umena, Y., Kawakami, K., Kamiya, N., Shen, J. R., and Yamaguchi, K. (2012) Theoretical illumination of water-inserted structures of the CaMn₄O₅ cluster in the S₂ and S₃ states of oxygen-evolving complex of photosystem II: Full geometry optimizations by B3LYP hybrid density functional, *Dalton Trans.* 41, 13727-13740.
- [13] Krewald, V., Retegan, M., Cox, N., Messinger, J., Lubitz, W., DeBeer, S., Neese, F., and Pantazis, D. A. (2015) Metal oxidation states in biological water splitting, *Chem. Sci.* 6, 1676-1695.
- [14] Saito, K., Rutherford, A. W., and Ishikita, H. (2015) Energetics of proton release on the first oxidation step in the water-oxidizing enzyme, *Nat. Commun.* 6, 8488.
- [15] Shoji, M., Isobe, H., Nakajima, T., and Yamaguchi, K. (2016) Large-scale QM/MM calculations of the CaMn₄O₅ cluster in the oxygen-evolving complex of photosystem II: Comparisons with EXAFS structures, *Chem. Phys. Lett.* 658, 354-363.
- [16] Siegbahn, P. E. (2014) Water oxidation energy diagrams for photosystem II for different protonation states, and the effect of removing calcium, *Phys. Chem. Chem. Phys.* 16, 11893-11900.
- [17] Galstyan, A., Robertazzi, A., and Knapp, E. W. (2012) Oxygen-evolving Mn cluster in

- photosystem II: The protonation pattern and oxidation state in the high-resolution crystal structure, *J. Am. Chem. Soc.* *134*, 7442-7449.
- [18] Robertazzi, A., Galstyan, A., and Knapp, E. W. (2014) PSII manganese cluster: protonation of W2, O5, O4 and His337 in the S₁ state explored by combined quantum chemical and electrostatic energy computations, *Biochim. Biophys. Acta* *1837*, 1316-1321.
- [19] Amin, M., Vogt, L., Szejgis, W., Vassiliev, S., Brudvig, G. W., Bruce, D., and Gunner, M. R. (2015) Proton-coupled electron transfer during the S-state transitions of the oxygen-evolving complex of photosystem II, *J. Phys. Chem. B* *119*, 7366-7377.
- [20] Petrie, S., Gatt, P., Stranger, R., and Pace, R. J. (2012) The interaction of His337 with the Mn₄Ca cluster of photosystem II, *Phys. Chem. Chem. Phys.* *14*, 4651-4657.
- [21] Petrie, S., Stranger, R., and Pace, R. J. (2015) Rationalising the geometric variation between the A and B monomers in the 1.9 Å crystal structure of photosystem II, *J. Chem. - Eur. J.* *21*, 6780-6792.
- [22] Berthold, D. A., Babcock, G. T., and Yocum, C. F. (1981) A highly resolved, oxygen-evolving photosystem II preparation from spinach thylakoid membranes: EPR and electron-transport properties, *FEBS Lett.* *134*, 231-234.
- [23] Ono, T., and Inoue, Y. (1986) Effects of removal and reconstitution of the extrinsic 33, 24 and 16 kDa proteins on flash oxygen yield in photosystem II particles, *Biochim. Biophys. Acta* *850*, 380-389.
- [24] Iizasa, M., Suzuki, H., and Noguchi, T. (2010) Orientations of carboxylate groups coupled to the Mn cluster in the photosynthetic oxygen-evolving center as studied by polarized ATR-FTIR spectroscopy, *Biochemistry* *49*, 3074-3082.
- [25] Okubo, T., and Noguchi, T. (2007) Selective detection of the structural changes upon photoreactions of several redox cofactors in photosystem II by means of light-induced ATR-FTIR difference spectroscopy, *Spectrochim. Acta, Part A* *66*, 863-868.
- [26] Noguchi, T., and Sugiura, M. (2002) Flash-induced FTIR difference spectra of the water oxidizing complex in moderately hydrated photosystem II core films: Effect of hydration extent on Sstate transitions, *Biochemistry* *41*, 2322-2330.
- [27] Hienerwadel, R., and Berthomieu, C. (1995) Bicarbonate binding to the non-heme iron of photosystem II investigated by Fourier transform infrared difference spectroscopy and ¹³C-labeled bicarbonate, *Biochemistry* *34*, 16288-16297.
- [28] Noguchi, T., and Inoue, Y. (1995) Identification of Fourier transform infrared signals from the non-heme iron in photosystem II, *J. Biochem.* *118*, 9-12.
- [29] Goormaghtigh, E., Raussens, V., and Ruyschaert, J. M. (1999) Attenuated total reflection infrared spectroscopy of proteins and lipids in biological membranes, *Biochim. Biophys. Acta* *1422*, 105-185.

- [30] Rothschild, K. J., and Clark, N. A. (1979) Polarized infrared spectroscopy of oriented purple membrane, *Biophys. J.* 25, 473-487.
- [31] Nabedryk, E., and Breton, J. (1981) Orientation of intrinsic proteins in photosynthetic membranes. Polarized infrared spectroscopy of chloroplasts and chromatophores, *Biochim. Biophys. Acta* 635, 515-524.
- [32] Frisch, M. J., Trucks, G. W., Schlegel, H. B., Scuseria, G. E., Robb, M. A., Cheeseman, J. R., Scalmani, G., Barone, V., Mennucci, B., Petersson, G. A., Nakatsuji, H., Caricato, M., Li, X., Hratchian, H. P., Izmaylov, A. F., Bloino, J., Zheng, G., Sonnenberg, J. L., Hada, M., Ehara, M., Toyota, K., Fukuda, R., Hasegawa, J., Ishida, M., Nakajima, T., Honda, Y., Kitao, O., Nakai, H., Vreven, T., Montgomery, J. A., Jr., Peralta, J. E., Ogliaro, F., Bearpark, M., Heyd, J. J., Brothers, E., Kudin, K. N., Staroverov, V. N., Kobayashi, R., Normand, J., Raghavachari, K., Rendell, A., Burant, J. C., Iyengar, S. S., Tomasi, J., Cossi, M., Rega, N., Millam, J. M., Klene, M., Knox, J. E., Cross, J. B., Bakken, V., Adamo, C., Jaramillo, J., Gomperts, R., Stratmann, R. E., Yazyev, O., Austin, A. J., Cammi, R., Pomelli, C., Ochterski, J. W., Martin, R. L., Morokuma, K., Zakrzewski, V. G., Voth, G. A., Salvador, P., Dannenberg, J. J., Dapprich, S., Daniels, A. D., Farkas, O., Foresman, J. B., Ortiz, J. V., Cioslowski, J., and Fox, D. J. (2009) *Gaussian 09*, revision C.01, *Gaussian Inc., Wallingford CT*.
- [33] Vreven, T., Byun, K. S., Komaromi, I., Dapprich, S., Montgomery, J. A., Morokuma, K., and Frisch, M. J. (2006) Combining quantum mechanics methods with molecular mechanics methods in ONIOM, *J. Chem. Theory Comput.* 2, 815-826.
- [34] Nakamura, S., Nagao, R., Takahashi, R., and Noguchi, T. (2014) Fourier transform infrared detection of a polarizable proton trapped between photooxidized tyrosine Y_Z and a coupled histidine in photosystem II: Relevance to the proton transfer mechanism of water oxidation, *Biochemistry* 53, 3131-3144.
- [35] Nakamura, S., and Noguchi, T. (2016) Quantum mechanics/molecular mechanics simulation of the ligand vibrations of the water-oxidizing Mn₄CaO₅ cluster in photosystem II, *Proc. Natl. Acad. Sci. U. S. A.*
- [36] Nakamura, S., Ota, K., Shibuya, Y., and Noguchi, T. (2016) Role of a water network around the Mn₄CaO₅ cluster in photosynthetic water oxidation: A Fourier transform infrared spectroscopy and quantum mechanics/molecular mechanics calculation study, *Biochemistry* 55, 597-607.
- [37] Pantazis, D. A., Ames, W., Cox, N., Lubitz, W., and Neese, F. (2012) Two interconvertible structures that explain the spectroscopic properties of the oxygen-evolving complex of photosystem II in the S₂ state, *Angew. Chem. Int. Ed.* 51, 9935-9940.
- [38] Bovi, D., Narzi, D., and Guidoni, L. (2013) The S₂ state of the oxygen-evolving complex of photosystem II explored by QM/MM dynamics: spin surfaces and metastable states suggest

- a reaction path towards the S₃ state, *Angew. Chem. Int. Ed. Engl.* *52*, 11744-11749.
- [39] Trasatti, S. (1986) The absolute electrode potential: an explanatory note (Recommendations 1986), *Pure Appl. Chem.* *58*, 955-966.
- [40] Reiss, H., and Heller, A. (1985) The absolute potential of the standard hydrogen electrode: a new estimate, *J. Phys. Chem.* *89*, 4207-4213.
- [41] Berthomieu, C., Navedryk, E., Mantele, W., and Breton, J. (1990) Characterization by FTIR spectroscopy of the photoreduction of the primary quinone acceptor Q_A in photosystem II, *FEBS Lett.* *269*, 363-367.
- [42] Takano, A., Takahashi, R., Suzuki, H., and Noguchi, T. (2008) Herbicide effect on the hydrogen-bonding interaction of the primary quinone electron acceptor Q_A in photosystem II as studied by Fourier transform infrared spectroscopy, *Photosynth. Res.* *98*, 159-167.
- [43] Ashizawa, R., and Noguchi, T. (2014) Effects of hydrogen bonding interactions on the redox potential and molecular vibrations of plastoquinone as studied using density functional theory calculations, *Phys. Chem. Chem. Phys.* *16*, 11864-11876.
- [44] Guskov, A., Kern, J., Gabdulkhakov, A., Broser, M., Zouni, A., and Saenger, W. (2009) Cyanobacterial photosystem II at 2.9 Å resolution and the role of quinones, lipids, channels and chloride, *Nat. Struct. Mol. Biol.* *16*, 334-342.
- [45] Noguchi, T., and Sugiura, M. (2001) Flash-induced Fourier transform infrared detection of the structural changes during the S-state cycle of the oxygen-evolving complex in photosystem II, *Biochemistry* *40*, 1497-1502.
- [46] Hillier, W., and Babcock, G. T. (2001) S-state dependent Fourier transform infrared difference spectra for the photosystem II oxygen evolving complex, *Biochemistry* *40*, 1503-1509.
- [47] Debus, R. J., Strickler, M. A., Walker, L. M., and Hillier, W. (2005) No evidence from FTIR difference spectroscopy that aspartate-170 of the D1 polypeptide ligates a manganese ion that undergoes oxidation during the S₀ to S₁, S₁ to S₂, or S₂ to S₃ transitions in photosystem II, *Biochemistry* *44*, 1367-1374.
- [48] Kimura, Y., Mizusawa, N., Ishii, A., and Ono, T. (2005) FTIR detection of structural changes in a histidine ligand during S-state cycling of photosynthetic oxygen-evolving complex, *Biochemistry* *44*, 16072-16078.
- [49] Noguchi, T., and Sugiura, M. (2003) Analysis of flash-induced FTIR difference spectra of the S-state cycle in the photosynthetic water-oxidizing complex by uniform ¹⁵N and ¹³C isotope labeling, *Biochemistry* *42*, 6035-6042.
- [50] Suzuki, H., Sugiura, M., and Noguchi, T. (2009) Monitoring proton release during photosynthetic water oxidation in photosystem II by means of isotope-edited infrared spectroscopy, *J. Am. Chem. Soc.* *131*, 7849-7857.

- [51] Suzuki, H., Taguchi, Y., Sugiura, M., Boussac, A., and Noguchi, T. (2006) Structural perturbation of the carboxylate ligands to the manganese cluster upon $\text{Ca}^{2+}/\text{Sr}^{2+}$ exchange in the S-state cycle of photosynthetic oxygen evolution as studied by flash-induced FTIR difference spectroscopy, *Biochemistry* 45, 13454-13464.
- [52] Suzuki, H., Sugiura, M., and Noguchi, T. (2012) Determination of the miss probabilities of individual S-state transitions during photosynthetic water oxidation by monitoring electron flow in photosystem II using FTIR spectroscopy, *Biochemistry* 51, 6776-6785.
- [53] Zimmermann, J.-L., and Rutherford, A. (1986) Photoreductant-induced oxidation of Fe^{2+} in the electron-acceptor complex of photosystem II, *Biochim. Biophys. Acta* 851, 416-423.
- [54] Noguchi, T., Inoue, Y., and Tang, X. S. (1999) Structure of a histidine ligand in the photosynthetic oxygen-evolving complex as studied by light-induced Fourier transform infrared difference spectroscopy, *Biochemistry* 38, 10187-10195.
- [55] Noguchi, T., and Sugiura, M. (2002) FTIR detection of water reactions during the flash-induced S-state cycle of the photosynthetic water-oxidizing complex, *Biochemistry* 41, 15706-15712.
- [56] Debus, R. J. (2014) Evidence from FTIR difference spectroscopy that D1-Asp61 influences the water reactions of the oxygen-evolving Mn_4CaO_5 cluster of photosystem II, *Biochemistry* 53, 2941-2955.
- [57] Suzuki, H., Sugiura, M., and Noguchi, T. (2005) pH dependence of the flash-induced S-state transitions in the oxygen-evolving center of photosystem II from *Thermosynechococcus elongatus* as revealed by Fourier transform infrared spectroscopy, *Biochemistry* 44, 1708-1718.
- [58] Rappaport, F., Blanchard-Desce, M., and Lavergne, J. (1994) Kinetics of electron transfer and electrochromic change during the redox transitions of the photosynthetic oxygen-evolving complex, *Biochim. Biophys. Acta* 1184, 178-192.
- [59] Haumann, M., Liebisch, P., Muller, C., Barra, M., Grabolle, M., and Dau, H. (2005) Photosynthetic O_2 formation tracked by time-resolved X-ray experiments, *Science* 310, 1019-1021.
- [60] Noguchi, T., Suzuki, H., Tsuno, M., Sugiura, M., and Kato, C. (2012) Time-resolved infrared detection of the proton and protein dynamics during photosynthetic oxygen evolution, *Biochemistry* 51, 3205-3214.
- [61] Sakamoto, H., Shimizu, T., Nagao, R., and Noguchi, T. (2017) Monitoring the reaction process during the $\text{S}_2 \rightarrow \text{S}_3$ transition in photosynthetic water oxidation using time-resolved infrared spectroscopy, *J. Am. Chem. Soc.* 139, 2022-2029.
- [62] Kato, Y., Sugiura, M., Oda, A., and Watanabe, T. (2009) Spectroelectrochemical determination of the redox potential of pheophytin a, the primary electron acceptor in

photosystem II, *Proc. Natl. Acad. Sci. U. S. A.* *106*, 17365-17370.

- [63] Rappaport, F., Guergova-Kuras, M., Nixon, P. J., Diner, B. A., and Lavergne, J. (2002) Kinetics and pathways of charge recombination in photosystem II, *Biochemistry* *41*, 8518-8527.

General conclusion

Regarding the electron transfer and water oxidation mechanisms of PSII, many problems had been unresolved such as (1) the origin of the asymmetric electron transfer of two redox-active tyrosines, Y_Z and Y_D, which is crucial for the high quantum efficiency of water oxidation, (2) hydrogen bond networks used in proton release during water oxidation, (3) the roles of key amino acid residues around the Mn cluster in the water oxidation mechanism. To address the issues, in this study, we investigated the structures and reactions of these tyrosines and the WOC, especially focusing on their hydrogen-bond interactions and protonation structures, using the combinatorial approach of infrared spectroscopy and quantum chemical calculations.

To clarify the molecular mechanism of the proton-coupled electron transfer reaction of Y_Z and Y_D, we first analyzed their hydrogen-bonded structures (Chapter 2). It was shown from FTIR analysis that a proton of Y_Z was transferred to the neighboring D1-His190 upon photooxidation, forming a strong hydrogen bond with a high proton polarizability, whereas such a strong hydrogen bond was absent in oxidized Y_D. The QM/MM calculations revealed the rearrangement of the hydrogen bond network of water molecules around Y_Z upon oxidation. These results suggested that Y_Z has a key role in proton release during water oxidation, and a novel proton release mechanism through Y_Z' was proposed. Furthermore, we detected protons released to the bulk upon Y_Z and Y_D oxidation using the isotope-edited FTIR technique (Chapter 3). It was shown that a proton is released into the bulk upon Y_D oxidation, whereas no proton release was observed upon Y_Z oxidation. This indicated that long-distance proton transfer takes place upon Y_D oxidation in contrast to the Y_Z case, in which a proton was only shifted to the His through a hydrogen bond. A high activation energy originating from this long-distance proton transfer was concluded to be the reason for the redox reaction of Y_D much slower than that of Y_Z, causing the asymmetric electron transfer between Y_Z and Y_D. This difference was proposed to arise from amino acid residues, D1-N298 and D2-R294, hydrogen-bonded to the N π sites of the His residues coupled to Y_Z and Y_D, respectively.

In Chapter 4, to investigate the role of the hydrogen-bond network around the Mn cluster, we performed normal mode analysis of the OH stretching vibrations of water molecules by QM/MM calculations. The calculated OH stretching vibrations well reproduced the experimental FTIR spectrum, and among them, a vibrational mode delocalized over several water molecules

located between Y_Z and the Mn cluster was found. It was suggested that this vibrational mode contributes to a rapid proton transfer from the Mn cluster to Y_Z according to the Grotthuss mechanism. This result supported the proton transfer via Y_Z during water oxidation proposed in Chapter 2. Because this mechanism needs an excess positive charge on the Mn cluster as a driving force, this proton transfer was suggested to occur in the $S_2 \rightarrow S_3$ or $S_3 \rightarrow S_0$ transition.

Furthermore, we investigated the roles of amino acid residues interacting with the Mn cluster in water oxidation (Chapters 5 and 6). First, to clarify the role of the carboxylate ligands to the Mn cluster, we performed normal mode analysis of the COO^- vibrations of these carboxylate groups by QM/MM calculations (Chapter 5). The COO^- vibrations reproduced the experimental FTIR spectrum. The large downshift of the vibrational frequency and the changes in the CO lengths of D1-D170 in the $S_1 \rightarrow S_2$ transition indicated the shift of a positive charge from Mn4 to Ca via the π conjugation of this carboxylate group. Together with the concomitant changes in the OH lengths of the water ligands to Ca, we concluded that D1-D170 bridging Ca and Mn has a crucial role in controlling the reactivity of the water ligands to Ca. Next, to clarify the role of histidine residues in WOC, we performed polarized ATR-FTIR measurements and QM/MM calculations (Chapter 6). In the polarized FTIR difference spectra upon the S-state transitions, bands with large dichroic ratios were observed in the high-frequency region in the $S_1 \rightarrow S_2$ and $S_3 \rightarrow S_0$ transitions. The QM/MM analysis showed that these bands arise from the $\text{N}\tau\text{H}$ stretching vibration of the protonated cation form of D1-H337, which is hydrogen-bonded with the Mn cluster. From these results together with energy calculations, we concluded that D1-H337 stays in a protonated cation throughout the S-state cycle and this histidine regulates the redox potential of the Mn cluster to oxidize water molecules.

All of these results in the present study showed that the hydrogen-bonded structure is important to characterize the proton transfer reactions and the protonation structures of water molecules and amino acid residues. Moreover, it was shown that molecular vibrations are suitable for monitoring slight structural changes in PSII proteins, which cannot be detected by other spectroscopic methods. Such information of hydrogen bond interactions and structural changes in the catalytic site is crucial to clarify the molecular mechanism of water oxidation. Therefore, the methodology and results in the present study will make a significant contribution to the future researches for full understanding of the mechanism of photosynthetic water oxidation.

Acknowledgments

I would like to express my gratitude to all those who gave me the opportunity to complete this thesis. I am greatly indebted to my supervisor, Prof. Takumi Noguchi, for providing his knowledge, guidance, and technical supports. I could have learned the importance of objectivity and perseverance for science through research activities with him.

I deeply appreciate Dr. Ryo Nagao for sample preparations, significant advices and technical supports. I could have learned the biochemical techniques in this thesis. I also appreciate Dr. Ryouta Takahashi and Mr. Kai Ota for technical supports. They were the collaborators in my research activities and their supports were necessary to complete this study.

I greatly thank Prof. Hiroyuki Mino for helpful advices and discussions. I also thank Dr. Yuki Kato and all members in photo-bioenergetics laboratory for helpful discussion and kind supports. In particular, advices from Mr. Ryota Ashizawa and discussion with him have been meaningful to advance my researches about the computational techniques.

This research was supported by Japan Society for the Promotion of Science (JSPS) Fellows Grant-in-Aid 15J10320. QM/MM calculations were performed at the Research Center for Computational Science, Okazaki, Japan, and Information Technology Center, Nagoya University.